On the Simulation of Turbulent Fluid-Structure Interaction

Vom Fachbereich Maschinenbau
der Technischen Universität Darmstadt
zur Erlangung des Grades eines
Doktors der Ingenieurwissenschaften
(Dr.-Ing.)
genehmigte

Dissertation

von
M. Sc. Awais Ali
aus Multan, Pakistan

Referent:	Prof. Dr. rer. nat. Michael Schäfer
Korreferent:	Prof. Dr.-Ing. Johannes Janicka
Tag der Einreichung:	25. Oct 2016
Tag der mündlichen Prüfung:	08. Feb 2017

Darmstadt 2017
D 17

To my family

Acknowledgements

The research in this thesis is conducted at Institute of Numerical Methods in Mechanical Engineering at TU Darmstadt, under a doctoral fellowship from DFG Graduiertenkolleg "Instationäre Systemmodellierung von Flugtriebwerken". I am thankful to Prof. Michael Schäfer and Prof. Johannes Janicka for providing me this opportunity as a doctoral candidate.

I owe my deepest gratitude to Prof. Michael Schäfer for the constant support, discussion and ideas during this research. His support and encouragement has been vital for the completion of this thesis. I would also like to thank my co-supervisor Prof. Johannes Janicka for his help and support during this work.

I would like to thank Monika Müller for help with many administrative issues. I am also grateful to FNB system administrator Michael Fladerer, not only for keeping my computer running, but also for being a good friend with whom I shared many coffee brakes.

This acknowledgment can not be completed without saying thanks to my colleagues. I benefited a lot from many discussions at FNB. For this, I would like to express my sincere gratitude to Tilo Winter, Andreas Schmitt, Jakob Munz, Xin Huang, Hariyo Pratomo, Dominik Staab and Stefan Kneißl. I would specially like to thank Anastasia Kondratyuk for very helpful discussions with her. I also owe a special thanks to Jonas Friedrich, with whom I shared our office during the writing of this thesis, his proofreading of this manuscript has been of tremendous help.

I am sincerely thankful to Dörte Sternel for incredible support and suggestions during this work, specially for translating the summary of this thesis to German language. I am also grateful to Thorsten Reimann for many nice discussions and sharing ideas, and also for proofreading my thesis.

I would also like to thank my family for supporting me in every possible way, specially my mother and father for their constant support and prayers. A special thanks to my wife Ayesha and sweet son Adan for their understanding and support during the course of this work.

Contents

Chapter 1
Introduction

1.1 Motivation

Fluid-structure interaction (FSI) problems involve one or more flexible structures interacting with a fluid flow either internal or by surrounding the structure. The structure exposed to the fluid flow is deformed and deflected under the influence of fluid forces acting on it. The deformation of the structure further influences the flow, resulting in a complex coupling process. These phenomena are relevant in numerous scientific and engineering disciplines. The analytical solution of model equations for most of the FSI problems are impossible, while experimentation has its limitations associated with measuring techniques, cost and design of experiments for real world applications.

Numerical techniques have gained significant popularity for the simulation of coupled problems in recent years. This popularity is fueled by recent developments in computational technology that have made it possible to study complex and sophisticated models to simulate coupled problems. The use of numerical simulations is becoming important in understanding various physical effects occurring in a coupled problem. For this purpose, different commercial and in-house software packages are used in academia and industry. The major concern with these simulations is the efficiency, stability and accuracy of predictions for the coupled phenomena.

The use of FSI simulations is spreading across various disciplines of science and engineering, ranging from bio-medicine to aerospace. In bio-medicine, patient specific blood flow simulation through arteries has a growing interest, where the data from simulations can help in diagnosis and treatment. The flutter analysis of an aircraft or a turbine blade is an important application from aerospace industry. The FSI analysis can be critical for long lasting and efficient design of aircraft wings and turbine blades. Similarly, FSI simulations can also be employed in civil engineering to study the dynamic response of buildings and bridges under wind loading.

The simulation of individual problems from fluid or structural dynamics could be a computationally intensive task, depending upon the problem size and numerical models. When the solution for a coupled FSI problem is sought, the most obvious distinction is made between monolithic and partitioned coupling strategies. In monolithic approaches, the individual fluid and structure subproblem are stated as one problem discretized on one single grid covering both physical fields, while in a partitioned approach the fluid and structure are treated as individual problems with coupling through boundary conditions and data exchange at the fluid-structure interface. Partitioned approaches are preferred on the basis of software modularity and re-useability. But these coupling algorithms often need multiple coupling iterations in a time step to achieve stability and convergence, which adds to the computational cost. Also, the task to develop a coupling environment between two solvers is not usually straightforward and requires a considerable amount of research effort for testing and validation. On the other hand, dealing with flow simulations, turbulence poses a major challenge in achieving accurate flow predictions with economical computational cost. Significant research has been done in the field of turbulence modeling, with an aim of developing highly accurate and computationally economical turbulence models. The application of these methods needs to be verified in the FSI context. Another important aspect is the computational time required for these simulations, which in turbulent FSI analysis depends a great deal on the turbulence modeling approach and the coupling strategy. The ultimate goal is to employ validated coupling environments to replace or minimize the expensive experimentation for the analysis of FSI applications.

1.2 State of the Art

This section gives a literature review related to the current work. The focus is on studies in the area of FSI, while a short discussion on turbulence modeling relative to this study is also provided.

Fluid-Structure Interaction

Fluid-structure interaction studies and algorithms can be broadly classified into categories based on the coupling strategy as described in the previous section and based on the treatment of meshes. The classification based on the treatment of meshes is distinguished by whether the fluid mesh is adapted/moved to conform to the structure or the mesh remains unchanged i.e. non-conforming.

Based on the coupling strategy, the numerical procedures to solve FSI problems are mainly classified into monolithic and partitioned coupling approaches. The monolithic approaches treat the fluid and structural subproblem in the same mathematical framework on a single grid to form a single system of equations for the entire problem. The monolithic approach to FSI simulation has been demonstrated in works of Heil [34], Walhorn et al. [119] and Hron and Turek [38], a review of other studies has been provided in [40]. On the other hand, the partitioned approaches deal with the coupling explicitly by data exchange at the interface between two subproblems that are solved in different computational frameworks on their respective meshes. Two further classifications between partitioned coupling approaches are termed as explicit (also known as loose or weak coupling) and implicit coupling (also known as strong coupling) strategies. In explicit partitioned coupling strategies [61, 22, 58] the data exchange and coupling between two solvers for fluid and structural subproblems is performed only once per time step. This kind of strategy is only suitable for weak fluid structure interaction and puts a strict limitation on the time step size. The implicit partitioned coupling technique enforces the equilibrium of traction and velocity/displacement at the fluid structure interface by successive iterations of the coupling procedure between two solvers, for each time step. The solvers can calculate the individual subproblems either in a Jacobi iteration scheme (parallel execution of the fluid and the structural solver) or a Gauss-Seidel iteration scheme (sequential execution of the fluid and the structural solver). The implicit coupling partitioned scheme has been employed in the works of Sternel et al. [102], Schäfer et al. [91] and Vierendeels et al. [118]. However, the slow convergence of these algorithms is a well known issue and significant research is being done for the development of acceleration techniques, where Aitken [42] and IQN-ILS [15] are frequently used. This work employs an implicit partitioned coupling strategy to solve FSI problems, a detailed review of partitioned coupling techniques and acceleration of these techniques has been provided by Degroote in [14].

The next classification in FSI methods is based on the movement of the fluid grid. The fluid subproblem is generally solved in Eulerian formulation, i.e. on a fixed-grid. The Arbitrary Lagrangian Eulerian (ALE) formulation of Navier-Stokes equations for moving grids was proposed by Hirt et al. [36], where the grid can deform at an arbitrary velocity, independent of fluid motion. Donea et al. [17] adopted the ALE formulation to propose Finite Element models for FSI analysis. In contrast to the ALE formulation, there has been a number of fixed grid approaches that has been used for FSI studies. In this regard, the Immersed Boundary (IB) method [67] was developed by Peskin [76] to study the flow patterns around heart valves. In IB methods the structure is represented by so called fibers, which consist of a chain of solid nodes. A three-dimensional structure could be represented by weaving a net of these fibers. Another fixed grid technique for fluid simulation with immersed bodies is called distributed Lagrange multiplier fictitious domain

(DLM/FD) method, proposed by Glowinski et al. [28, 27]. The method has been used for the simulation of interaction between fluid and flexible structures in [3, 126]. In DLM/FD method, the fluid grid region occupied by the structure is filled with the same fluid as the remainder of the fluid domain. This fictitious fluid is constrained with Lagrange multipliers to move with the same velocity as the structural domain. Wall et al. [120] proposed a combination of extended finite element method (XFEM) and the DLM/FD method. The XFEM method originated for the simulation of cracks in finite element analysis of structures. The advantage of such a method is the decoupling of the fictitious fluid overlapped by the structure and the fluid around by the use of the XFEM method. Wall et al. [120] also proposed a moving and fixed fluid grid approach, where a local body-fitted grid around the structure is employed to take advantage of the ALE formulation. Both the moving fluid grid and the structure move on a fixed fluid grid, where the fixed fluid grid overlapped by the structure is disabled. The fluid flow on the fixed grid and moving grid are calculated with a Chimera technique [100]. The main advantage of IB and FD methods is that the fixed fluid grid does not change, which enables the use of simple and fast solvers. A main disadvantage is the loss of accuracy near the fluid-structure interface, due to inaccurate representation of the interface. Also, at high Reynolds numbers where a very fine grid is required in the vicinity of solid boundaries, these methods might suffer from unacceptable grid design.

Turbulence Modeling

Even though the advent of high performance computing technology has made studies of many computationally intensive problems possible, turbulence still posses a challenge owing to the multi-scale nature of the problem. The exact simulation of turbulence for flows with practical relevance, where all scales are resolved, might not be possible in a foreseeable future. This makes turbulence modeling a key area of research with effort towards developing models to accurately represent effects of turbulence in fluid motion, while keeping the computational cost manageable. In this context, the statistical approach to model turbulence, also known as the Reynolds Averaged Navier-Stokes (RANS) modeling technique is favored in industry owing to lower computational cost than scale resolving simulation techniques. In RANS concepts, the turbulent quantities are decomposed into mean flow and turbulent fluctuations as introduced by Reynolds [85]. The decomposition when applied to Navier-Stokes equations, results in RANS equations and the closure problem with the emergence of Reynolds stress terms in RANS equations. The closure problem necessarily means more unknowns than number of equations available for a determinate solution. Based on the mechanism to handle the closure problem, the RANS modeling techniques are categorized in two broad groups;

the Reynolds stress models (RSM) and eddy viscosity models (EVM). In the RSM technique, a transport equation for each component of the Reynolds stress tensor is sought, however some empiricism is involved to obtain solutions for these equations, more details about RSM techniques can be found in [53]. In contrast the EVM approach is based on the Boussinesq hypothesis [4], where the Reynolds stresses are modeled with an eddy viscosity. The eddy viscosity in RANS turbulence models is calculated based on the solution of some transported turbulent quantity. The two equation $k-\epsilon$ model proposed by Launder and Sharma [55], models the eddy viscosity by means of k and ϵ, which represent the turbulent kinetic energy and the dissipation rate of turbulent kinetic energy, respectively. The model became a standard tool for computing turbulent flows, despite some issues for predictions of wall bounded flows. Chien [11] and Launder and Sharma [54], presented improvements to the initial proposal of the $k-\epsilon$ model, which addressed some of the issues. Spalart and Allmars [97] proposed a one equation model based on a transport equation for the eddy viscosity, which is commonly known as the S-A model. The S-A model has gained significant popularity specially for applications in the field of external aerodynamics. Another two equation model, the $k-\omega$ model with ω being the specific dissipation rate of turbulence, was presented by Wilcox [122]. The $k-\omega$ model was shown to perform better than other two equation models in the presence of adverse pressure gradients. The model also formed the basis for Shear Stress Transport (SST) model by Menter [122], which aims to combine the advantages of the $k-\epsilon$ and the $k-\omega$ model. A subclass of the EVM models is the non-linear eddy viscosity models, in which the eddy viscosity is related to the mean flow in a non-linear relationship. These models offer better predictions than linear EVM models with a minor increase in the computational cost. The explicit algebraic Reynolds stress models (EARSM) [121], the elliptic relaxation models of Durbin [19] and Hanjalić [32], are more generally known models belonging to non-linear EVM class of models.

As stated earlier, a complete resolution of turbulence in a practical flow application might not be feasible computationally. But a partial resolution of turbulence, where modeled and resolved scales are separated based on a filtering approach might still be possible. Such a simulation methodology is known as the Large Eddy Simulation (LES) technique. The motivation behind partial resolution of turbulence comes from Kolmogorov's self-similarity hypothesis. The Kolmogorov's hypothesis considers large energy containing turbulent motions to be anisotropic under the influence of geometric and boundary conditions, while small scales have universal isotropic character. This universal character of small scales makes them an excellent candidate for modeling, also the resolution of large anisotropic and energy containing motions improves the prediction of flow. Today, there are a number of LES models available, but the approach was first demonstrated by Smagorinsky [93] for atmospheric flows. Later Deardorff [13] demonstrated the application of the same model for a three dimensional turbulent channel flow. The

model today is available in many commercial CFD codes as a standard model for performing LES. The Smagorinsky model suffers from some well known issues; the model fails to predict transition to turbulence and requires damping of the modeled turbulent viscosity in wall vicinity to recover correct wall behavior. Germano et al. [26] addressed these issues with a dynamic calculation procedure of the model constant. The Wall adapting local eddy viscosity (WALE) model [18] offers a solution to the issues encountered with the Smagorinsky model, without the dynamic calculation of the model coefficient. The eddy viscosity for modeled scales in the WALE model depends on the local strain as well as the rotation rates. For a deep insight into the LES and modeling approaches associated with incompressible LES, the reader may refer to the book from Sagaut [89].

Due to computational requirements, the use of LES techniques remain limited to research and academia for a foreseeable future. While RANS computations are affordable, the accuracy of predictions is still a concern. The hybrid RANS-LES approach emerged as an alternative to RANS and LES, with efforts to combine advantages of both techniques. In this regard, the Detached Eddy Simulation [96] model was proposed by Spalart in 1997. In the DES approach, a RANS model is modified to perform an LES in regions where the grid is fine enough for an LES. The switch between two approaches is based on a length scale. The original formulation of the DES model proposed by Spalart modified the S-A RANS model to perform a DES. A later proposal to modify Menter's SST model to a DES was presented by Strelets [104]. The DES model suffered from some problems associated with the location of RANS-LES interfaces. The modification of the original formulation was proposed in [95] to obtain the Delayed Detached Eddy Simulation (DDES) model. In an effort to make the DDES approach applicable as wall modeled LES the Improved-DDES (IDDES) model was proposed by Travin [113]. Many other studies have been conducted with different RANS turbulence models to work as a DES model, a detailed study of these approaches can be found in [68]. Another widely used hybrid model is the Scale Adaptive Simulation (SAS) model proposed by Menter [65]. A review of hybrid RANS-LES techniques has been provided by Fröhlich [25].

Turbulent FSI

This section highlights some important work in the field of the turbulent FSI. Numerous studies about FSI of parachutes has been conducted by the group of Tezduyar, including [107, 101, 106]. However in most of these studies the focus has been on numerical methods for FSI and just in [101] the use of the Smagorisnky model is mentioned. In [62], Lüdeke has performed FSI analysis of the Ariane-5 nozzle in the start-up phase by employing a DES model for the turbulent fluid simulation. Martinat et al. [63] has performed FSI

analysis for dynamic stall on a NACA0012 airfoil with different turbulence modeling approaches. The results from the study show a better agreement with the experimental data for Menter's SST model and it is argued that for accurate simulations of the dynamic stall more sophisticated unsteady RANS (URANS) models are required. Shinde et al. [92] employed URANS and DDES models to study the vortex induced vibration in tube arrays. The turbulent FSI of a NREL phase VI wind turbine has been studied in [39, 59]. In [59], an overset grid methodology is applied for the fluid simulation, while turbulence is modeled with a $k-\omega$ SST and a DES model. The application of LES models for turbulent fluid simulation has been studied by the group of Breuer in [29, 70, 7, 73, 72]. The same group has also proposed two experimental FSI test cases in [73, 72], for validation or benchmarking purposes. These test cases are presented as simplifications to the proposal by Gomes and Lienhart [30], for their proposal of a turbulent FSI test case. The test case proposed in [30] has been studied by Reimann [83], in a 2-d URANS flow configuration. In [115], a self adaptive airfoil designed for wind turbines is studied with RANS and hybrid RANS-LES modeling techniques.

1.3 Goals and Outline

The application of three different turbulence modeling techniques in the context of FSI simulations is studied with the help of benchmark FSI test cases. A comparison based on the oscillation characteristics and flow visualizations, between 2-d and 3-d URANS flow simulations for two different FSI test cases [73, 72] is performed. The same test cases are also studied with the DDES model for turbulence. Further a comparison between a DDES and a LES simulation is drawn for the turbulent FSI test case proposed in [30]. A Poisson equation based wall distance calculation procedure is implemented in FASTEST [2], for use in the DDES turbulence model. For computational efficiency, an universal wall function approach is implemented in the flow solver FASTEST. The implementation is first tested on static grids with a channel flow test case and then a test on moving grids is performed with the help of an FSI simulation on a coarse grid. Coupling acceleration techniques are studied with a lid-driven cavity test case in laminar and turbulent flow regimes. The turbulence modeling options in FASTEST are enhanced with the implementation and validation of the WALE model for LES.

The work is organized into six chapters. The first chapter gives an introduction to this work and previous works relating to this study. In the second chapter a short description of the physical governing principles of fluid and structure are given, while the formulation of governing principles for fluid dynamics in an Arbitrary Lagrangian Eulerian frame is also described. The third chapter deals with the numerical techniques for the solution of fluid and structure dynamics problem, also a short discussion of Finite Volume and Finite

Element methods is provided. The fourth chapter specifically deals with the issue of turbulence. The physical phenomena behind turbulence is discussed briefly, while the focus is on modeling of turbulence. The implementation of wall distance calculation, universal wall functions and the WALE model for LES are discussed in a separate section in chapter four. The discussion on results from FSI simulations is provided in the fifth chapter. This is provided by combining URANS and scale resolving simulations into respective subsections, with further division based on the studied test cases.

Chapter 2
Physical Modeling

In this chapter the fundamental equations governing the conservation principles of mass and momentum are described for fluid and solid subproblem, which are further employed in a coupled fluid-structure interaction framework. Concerning the simulation of the fluid subproblem in moving domains, the governing equations are also formulated in Arbitrary Lagrangian Eulerian (ALE) formulation. A detailed discussion about the topics in this chapter can be found in standard textbooks, e.g. [90, 127, 23].

2.1 Governing Equations of Fluid Dynamics

This section introduces the governing equations of fluid dynamics. The motion of fluids is governed by the conservation principles of mass, momentum and energy. The conservation principles are written here in differential form using Einstein's notation. The continuity equation, governing the conservation of mass is written as

$$\frac{\partial \rho}{\partial t} + \frac{\partial (\rho u_i)}{\partial x_i} = 0 \, , \tag{2.1}$$

where ρ is the fluid density, t is the time, and u_i are the velocity components in spatial directions x_i. The governing equation of momentum conservation is given as

$$\frac{\partial (\rho u_i)}{\partial t} + \frac{\partial (\rho u_i u_j)}{\partial x_j} = \frac{\partial \tau_{ij}}{\partial x_j} + \rho f_i \, , \tag{2.2}$$

with τ_{ij} representing the Cauchy stress tensor and f_i representing the body forces acting on the fluid such as gravity or buoyancy. For Newtonian fluids the stress tensor τ_{ij} is defined as

$$\tau_{ij} = \mu \left(\frac{\partial u_i}{\partial x_j} + \frac{\partial u_j}{\partial x_i} - \frac{2}{3} \frac{\partial u_k}{\partial x_k} \delta_{ij} \right) - p\delta_{ij} \ , \tag{2.3}$$

where p is the fluid pressure, μ is the dynamic viscosity of the fluid and δ_{ij} is the Kronecker delta.

Equations (2.1) and (2.2) are also known as the Navier-Stokes (NS) equations. The present work assumes the fluid to be incompressible, isothermal and Newtonian, while the incompressibility assumption is valid for flows with Mach number $Ma < 0.3$. With the assumption of an incompressible and isothermal fluid, the time derivative of density in continuity equation (2.1) vanishes transforming the equation to

$$\frac{\partial u_i}{\partial x_i} = 0 \ . \tag{2.4}$$

Further, using the continuity equation the divergence term in the definition of shear stress tensor (equation (2.3)) vanishes, and the momentum equation for an incompressible fluid is written as

$$\frac{\partial (\rho u_i)}{\partial t} + \frac{\partial (\rho u_i u_j)}{\partial x_j} = \frac{\partial}{\partial x_j} \left[\mu \left(\frac{\partial u_i}{\partial x_j} + \frac{\partial u_j}{\partial x_i} \right) - p\delta_{ij} \right] + \rho f_i \ . \tag{2.5}$$

Equations (2.4) and (2.5) define the conservation principles for an incompressible, isothermal and Newtonian fluid motion. These equations define the fluid subproblem of the coupled fluid-structure interaction study in this work. The solution techniques employed to solve these equations are described in the next chapter.

2.2 Arbitrary Lagrangian Eulerian Formulation

The incompressible Navier-Stokes equations in the previous section (equations (2.4) and (2.5)) are written for a Eulerian frame of reference. The Eulerian formulation of flow field is a way of looking at the fluid motion while focusing on a specific location in space, through which the fluid flows. The formulation is not suitable for moving boundaries with body-fitted meshes. In this work, the Arbitrary Lagrangian Eulerian formulation is used for the solution of conservation equations of the fluid subproblem on moving grids. The main idea of the ALE approach is that an observer is neither located at a fixed position in space nor moves with the material point, but it can move *arbitrarily*. To achieve this for the conservation laws already described, a relative velocity is introduced in the convective term. Equations (2.4) and (2.5) in ALE form reads as

$$\frac{\partial u_i}{\partial x_i} = 0 \ , \tag{2.6}$$

$$\frac{\partial(\rho u_i)}{\partial t} + \frac{\partial(\rho u_j(u_i - u_i^g))}{\partial x_j} = \frac{\partial}{\partial x_j}\left[\mu\left(\frac{\partial u_i}{\partial x_j} + \frac{\partial u_j}{\partial x_i}\right) - p\delta_{ij}\right] + \rho f_i \ , \quad (2.7)$$

where u_i^g is the grid velocity in x_i direction. It is evident that equations (2.6) and (2.7) reduce to the incompressible NS equations (2.4) and (2.5) in Eulerian formulation when the grid velocity $u_i^g = 0$ and turn into Lagrangian formulation when the grid velocity is $u_i^g = u_i$.

Space Conservation Law

The ALE formulation uses a relative velocity, i.e. $u_i - u_i^g$ for the calculation of convective fluxes at cell faces. In moving meshes, the mass balance is not necessarily ensured when the cell faces move. The conservation of mass for equations (2.6) and (2.7) require an additional condition to be fulfilled, which is called Space Conservation Law (SCL) [110, 16]. Consider a fluid domain Ω_f with control volumes V and surface S, then the space conservation law is stated as

$$\frac{\partial}{\partial t}\int_V \mathrm{d}V = \int_S u_i^g \mathrm{d}S \ . \quad (2.8)$$

The SCL can be thought of as a continuity equation in the limit of zero fluid velocity, as it ensures that the sum of fluxes through control volume faces due to grid movement are equal to the rate of change of the volume itself.

2.3 Governing Equations of Solid Mechanics

In structural dynamics simulation, the Lagrangian formulation of the governing equations of solid mechanics is preferred, as a deformed state is to be determined from a known reference configuration, which can naturally be done by tracking the corresponding material points [90]. For a structural subdomain Ω_s the deformations of the structure ϑ_i are defined in terms of the position in a reference configuration $X = X_i$ and the position in the current configuration $x = x_i$ as

$$\vartheta_i = x_i - X_i \ . \quad (2.9)$$

The basic equation of momentum balance for the solid domain Ω_s is then written as

$$\rho_s \frac{\partial^2 \vartheta_i}{\partial t^2} = \frac{\partial(S_{ji}F_{ij})}{\partial X_j} + \rho_s f_i \ , \quad (2.10)$$

where the deformation gradient F_{ij} is defined as

$$F_{ij} = \frac{\partial x_i}{\partial X_j} \ . \quad (2.11)$$

In equation (2.10) S_{ij} is the second Piola-Kirschhoff stress tensor, ρ_s is the density of the solid material and f_i represents the external forces acting on the solid. In the present study a simple hyper-elastic material model, the Saint Venant-Kirschhoff law, is employed. For the second Piola-Kirchhoff stress tensor the model states

$$S_{ij} = \lambda_s E_{kk} \delta_{ij} + 2\mu_s E_{ij} \ , \tag{2.12}$$

where the Green-Lagrange strain tensor is represented as

$$E_{ij} = \frac{1}{2}(F_{ki} f_{kj} - \delta_{ij}) \ , \tag{2.13}$$

with λ_s and μ_s as Lamé constants. These constants are expressed in terms of material properties Young's modulus E_s and Poisson's ratio ν_s as

$$E_s = \frac{\mu_s(3\lambda_s + 2\mu_s)}{\lambda_s + \mu_s} \ \text{ and } \ \nu_s = \frac{\lambda_s}{2(\lambda_s + \mu_s)} \ . \tag{2.14}$$

The momentum equation (2.10) represents a system of differential equations, which describe the deformation of the structure. These equations can be solved with appropriate boundary conditions. For linear elasticity problems either prescribed displacements or stresses on the boundary of the domain Ω_s can be employed as boundary conditions.

Chapter 3
Computational Methodology

The physical governing principles for fluid and structural dynamic subproblems have been described in the previous chapter. This chapter concerns the layout of the coupled FSI framework and numerical techniques to solve the individual subproblems, used in this work. The Finite Volume Method (FVM) is discussed for the fluid subproblem. The FVM methods described in this chapter are incorporated in the in-house code FASTEST [2], which is a multigrid solver for block-structured body fitted meshes. The parallelization in FASTEST is achieved with domain decomposition and communication via MPI. Further, the Finite Element Method (FEM) to solve the structural subproblem are also briefly discussed, where the FEM based code FEAP [108] is employed to solve the structural subproblem.

3.1 Finite Volume Method

The Navier-Stokes equations (2.4) and (2.5) are a set of non-linear partial differential equations. The set of equations can be solved with the help of various numerical techniques such as, the Finite Difference Method, the Finite Element Method (FEM), the Finite Volume Method (FVM) and the spectral methods. The FVM has been more popular for the solution of NS equations owing to the conservation property of the control volume formulation.

As a starting point the fluid domain Ω_f is decomposed into a finite number of Control Volumes (CVs). Equations (2.4) and (2.5) are then integrated over an arbitrary CV with volume V and surface S. For convective and diffusive terms of the incompressible Navier-Stokes equations, Gauß' theorem is used to convert volume integrals over V to surface integrals over S, to reach the following form of the continuity and momentum equations

$$\int_S u_i n_i \mathrm{d}S = 0, \tag{3.1}$$

$$\frac{\partial}{\partial t}\int_V \rho u_i \mathrm{d}V + \int_S \rho u_i (u_j - u_j^g) n_j \mathrm{d}S = \int_S \mu \left(\frac{\partial u_j}{\partial x_i} + \frac{\partial u_i}{\partial x_j} \right) n_j \mathrm{d}S - \int_S p \delta_{ij} n_j \mathrm{d}S + \int_V \rho f_i \mathrm{d}V. \tag{3.2}$$

The surface and volume integrals in the equations above are approximated using numerical integration, while the derivatives are estimated at a CV surface or faces via interpolation of cell center values. With these approximations the set of non-linear partial differential equations is converted into an algebraic system of equations, which can then be solved with a suitable iterative solution technique.

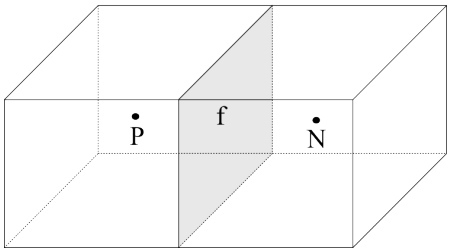

Fig. 3.1: A schematic representation of a control volume around a point P with neighboring control volume around point N and a shared face f between P and N.

We consider a hexahedral CV around a point P with coordinates (x_P, y_P, z_P), while N with coordinates (x_N, y_N, z_N) denotes the midpoint of the neighboring CV, as shown in figure 3.1. Also, f denotes the midpoint of the cell face between P and N, with coordinates (x_f, y_f, z_f). The task from here on is the approximation of surface and volume integrals in equations (3.1) and (3.2). The approximation of surface integrals will require the interpolation of quantities from cell centers to cell faces. The following sections give details about the approximation of these integrals and the interpolation practice to calculate cell face values.

Approximation of the convective term

The convective term in NS equations is a non-linear term and requires a special treatment. It is approximated as a product of *old* and *new* velocity fields. The mass flux required for the approximation of this term is assumed to be known from the previous iteration of the solution procedure. The calculation of the convective fluxes require the approximation of velocity at the CV faces. Nevertheless the convective term for the u_i velocity is calculated as

$$F_c = \int_S \rho u_i u_j n_j \mathrm{d}S = \sum_f \dot{m}_f (u_i)_f \ , \tag{3.3}$$

where f represents a CV face, and in 3-d corresponds to six faces of the hexahedral control volume. Now the u_i velocity at cell face f is approximated using a Central Differencing Scheme (CDS) between the point P and the neighbor N as

$$(u_i)_f = \gamma_f (u_i)_N + (1 - \gamma_f)(u_i)_P \ , \tag{3.4}$$

where γ_f represent the factor for linear interpolation scheme CDS between P and N and is calculated as

$$\gamma_f = \frac{(x_i)_f - (x_i)_P}{(x_i)_N - (x_i)_P} \ . \tag{3.5}$$

For orthogonal grids the CDS is second order accurate. The scheme is conditionally bounded and produces oscillation for rapid changes in the interpolated quantity across the cells. The boundedness criteria for the CDS is defined using the cell Péclet number defined for a generic transport quantity ϕ as

$$\mathrm{Pe} = \frac{\rho \phi \Delta x}{\Gamma_\phi} \ < \ 2 \ , \tag{3.6}$$

where Δx is the grid spacing and Γ_ϕ is the diffusion coefficient of ϕ. This condition may require very small grid spacings when the diffusion coefficient is very small. A solution to overcome this problem is to use the Upwind Differencing Scheme (UDS), which is a first order unconditionally bounded scheme, defined as

$$(u_i)_f = \begin{cases} (u_i)_P \text{ if } \dot{m}_f > 0 \ , \\ (u_i)_N \text{ if } \dot{m}_f < 0 \ . \end{cases} \tag{3.7}$$

The UDS has better properties regarding robustness and boundedness, but suffers from excessive numerical diffusion, which effects the accuracy of flow prediction. A blending between UDS and CDS can be performed to combine the bounded UDS scheme with the second order accurate CDS scheme as

$$(u_i)_f = (u_i)_f^{UDS} + \beta \left((u_i)_f^{CDS} - (u_i)_f^{UDS} \right) \ , \tag{3.8}$$

where $0 \leq \beta \leq 1$ is the flux blending factor. The above expression produces CDS approximation for $\beta = 1$ and a UDS for $\beta = 0$, a value between 0 and 1 produces a blending between UDS and CDS.

The current flow solver FASTEST uses the *deferred correction* approach with the flux blending technique to improve stability and accelerate the iterative solution procedure. In the deferred correction approach the blended part of the flux is treated explicitly and assumed to be know from the previous solver iteration. This helps improve the convergence properties by maintain-

ing the diagonal dominance of the coefficient matrix of linearized equation system.

Approximation of the diffusive term

The approximation of the diffusive term requires the evaluation of the stress τ_{ij} at cell faces, which in turn requires the gradients of velocity at cell faces. For equidistant cartesian grids a central differencing formula can be used to evaluate the gradients at the cell face f as

$$\left(\frac{\partial u}{\partial x}\right)_f \approx \frac{u_N - u_P}{x_N - x_P} \,. \tag{3.9}$$

Here the variation in the gradient is assumed to be linear. For equidistant cartesian grids, the expression leads to a second order accurate approximation. The accuracy drops to first order for non-equidistant grids. However, the fluid solver FASTEST also has a Taylor based interpolation (TBI) [56] method available, which produces an overall accuracy of second order even on distorted grids.

Approximation of integrals

The integrals in equation (3.2) are approximated using the second order accurate midpoint rule for numerical integration. The value at the control volume center is used to evaluate the volume integrals as

$$\int_V \rho f_i \mathrm{d}V \approx (\rho f_i)_P \delta V \quad , \qquad \frac{\partial}{\partial t}\int_V \rho u_i \mathrm{d}V \approx \left(\frac{\partial u_i}{\partial t}\right)_P \delta V \,. \tag{3.10}$$

Here the index P denotes a value at the midpoint, while δV denotes the volume of the CV.

Temporal discretization

The time derivative in (3.10) can be approximated analogous to the approximation of spatial derivatives. In general, the time integration methods are classified into explicit and implicit time discretization schemes. In explicit methods the solution at time step $n+1$ involves the calculation of convective, diffusive and source terms from known solution at previous time steps, whereas for implicit methods these terms have to be discretized at the un-

known time level $n+1$. The explicit methods suffer from a lack of stability at large time steps and hence are conditionally stable. The most commonly used time integration methods in computational fluid dynamic codes are explicit and implicit Euler methods, the Runge-Kutta methods and the Crank-Nicolson method. The second order backward differencing scheme (BDF2) is employed in this study, which reads as

$$\left(\frac{\partial u_i}{\partial t}\right)^{n+1} = \frac{3u_i^{n+1} - 4u_i^n + u_i^{n-1}}{2\Delta t} \,, \tag{3.11}$$

where the superscripts $n+1,\ n,\ n-1$ denote the time levels and Δt is the time step size.

Assembly and solution of the equations

The discretization and interpolation practices described earlier result in a system of algebraic equations, with terms depending only on cell centered values of u_i, p and the geometrical information of the grid. At this point the system matrix can be assembled. To improve stability of the solution procedure, the flow solver FASTEST employs the deferred correction approach as mentioned earlier. This means that the source terms have contributions from convective and diffusive fluxes calculated explicitly using the values from the previous solution iteration. The implicit part of these terms end up on the left hand side of the equation system and hence contributes to the system matrix. Other source terms such as body forces or the ones arising from a specified pressure gradient are added to the right hand side of the equation system. The system can then be represented as

$$a_P^k u_P^{k+1} - \sum_N a_N^k u_N^{k+1} = b_P^k \,, \tag{3.12}$$

where N is the index of neighboring cells of P, and $k\ ,\ \ k+1$ represent the iteration number. For incompressible flows, the system of equations lack a separate equation for pressure. The absence of a separate equation for pressure means that the system is severely ill-conditioned and cannot be solved directly, and hence needs special treatment. In practical flow simulation codes, these problems are overcome by employing *pressure correction methods*. The Semi-Implicit Method for Pressure-Linked Equations (SIMPLE) [74] algorithm is used in this study. The main idea in the SIMPLE algorithm is to use the continuity equation to derive an equation for pressure correction. The momentum equation is then used to calculate preliminary velocities using a pressure field from the previous time step, or a guessed pressure field is used as initial condition. The velocities and pressure are then corrected using the pressure correction equation, to satisfy the continuity equation. Also,

the method of Rhie and Chow [86] is used to avoid pressure oscillations that arise on collocated grids, when the continuity equation is discretized with the central differencing scheme. The resulting system of equations is solved with the Strongly Implicit Precedure (SIP) of Stone[103] .

3.2 Finite Element Method

The term Finite Element was first coined by Clough in 1960. In the early 1960s, engineers used the method to obtain approximate solution of problems in stress analysis, fluid flow, heat transfer, and other areas. Today Finite Element Methods are a standard tool used in the investigation of problems related to solid mechanics [90].

The first step towards solving a problem with FEM is to write the weak or variational formulation of the partial differential equation. We consider equation (2.10) for the solid domain Ω_s with Dirichlet and Neumann conditions at boundaries Γ_D and Γ_N, respectively. The momentum equation is then multiplied by an arbitrary test function η_i. By partial integration and with the condition $(\eta_i)_{\Gamma_D} = 0$, the following weak form of the problem is derived

$$\int_{\Omega_s} \delta E_{ij} S_{ij} \mathrm{d}V - \int_{\Omega_s} \eta_i \rho_s \frac{\partial^2 \vartheta_i}{\partial t^2} \mathrm{d}V - \int_{\Gamma_N} \eta_i t_i \mathrm{d}S - \int_{\Omega_s} \eta_i \rho_s f_i \mathrm{d}V = 0 \quad (3.13)$$

where δE_{ij} is the variation in Green-Lagrange strain tensor and t_i represents the surface forces on an element. The use of the weak formulation reduces the continuity requirement on approximation functions, thereby allowing the use of easy-to-construct polynomials. Another advantage is the natural and easy incorporation of Neumann boundary condition in the weak formulation.

Spatial Discretization

Similar to the FVM, the structural domain is divided into a finite number of discrete elements on which the geometrical and physical quantities are approximated. For integrals in equation (3.13) to be well defined, the surface integrals between adjacent cells must vanish. This occurs under the condition that functions η_i and ϑ_i are continuous in Ω_s, while the first derivatives can be discontinuous. According to the Ritz method, any function can be approximated as a linear combination of linearly independent functions and coefficients. The exact solution in an element e can be approximated as

$$(\vartheta_i)^e = \sum_{I=1}^{N_{el}} N_I^e(\mathrm{x})(\vartheta_i)_I^e, \tag{3.14}$$

where $N_I^e(\mathrm{x})$ represents the local shape function at node I with x being the position vector, $(\vartheta_i)_I^e$ represents the unknown solution for displacements at node I, while the local shape functions satisfies the following condition

$$N_I^e(\mathrm{x}_j) = \begin{cases} 1 \text{ for } j = I \\ 0 \text{ for } j \neq I \end{cases}, \tag{3.15}$$

which implies that N_I^e has a value of unity at node I and zero at all other nodes in the element e. Also using the local shape functions to represent the test functions η_i leads to the Galerkin Method. The choice of shape functions is determined by the dimensionality of the element and the desired order of the overall numerical method. In this study, 8-node hexahedera elements with linear shape functions are employed.

After the numerical integration of each term in equation (3.13) for individual elements, the resulting algebraic set of equations can be represented in matrix form. These individual element matrices are used to formulate the complete problem by superposition, which results in

$$M_{ij}^S \frac{\partial^2 \vartheta_i}{\partial t^2} + K_{ij}^S \vartheta_i = b_j^S, \tag{3.16}$$

where M_{ij}^S is the system mass matrix, K_{ij}^S is the stiffness matrix and b_j^S represents the load vector. More details concerning the discretization practices in FEM can be found in standard textbooks, for example [127, 90].

Temporal Discretization

Equation (3.16) still contains the 2$^{\text{nd}}$ time derivative, a suitable method for time integration is required for the solution. The Newmark beta method is a widely used time integration scheme for computational solid dynamics problems. The Newmark beta method can be derived from a Taylor series expansion of the velocity and displacement around a time step $n+1$. The resulting scheme states:

$$\vartheta_i^{n+1} = \vartheta_i^n + \Delta t \dot{\vartheta}_i^n + \frac{\Delta t^2}{2} \ddot{\vartheta}_i^n + \beta \Delta t^2 (\ddot{\vartheta}_i^{n+1} - \ddot{\vartheta}_i^n) \tag{3.17}$$

and

$$\dot{\vartheta}_i^{n+1} = \dot{\vartheta}_i^n + \Delta t \ddot{\vartheta}_i^n + \gamma \Delta t^2 (\ddot{\vartheta}_i^{n+1} - \ddot{\vartheta}_i^n). \tag{3.18}$$

Depending upon the choice of Newmark parameters β and γ different schemes can be recovered. The method is unconditionally stable for $\beta \geq \frac{1}{4}\left(\gamma + \frac{1}{2}\right)^2$,

whereas for $\gamma < \frac{1}{2}$ the method produces numerical dissipation and is conditionally stable.

An extension of the Newmark Method is the Hilber-Hughes-Taylor (HHT) Method [35]. An additional parameter α is introduced in equation (3.16) as

$$M_{ij}^S \frac{\partial^2 \vartheta_i^{n+1}}{\partial t^2} + (1+\alpha) K_{ij}^S \vartheta_i^{n+1} - \alpha K_{ij}^S \vartheta_i^n = b_j^{S,n+1}, \tag{3.19}$$

where the parameter α blends two time levels n and $n+1$ for the structural distortions, and can be used to control numerical dissipation in the system. In HHT method, to reduce the properties to a single parameter following relations for β and γ are employed as

$$\beta = \frac{(1-\alpha)^2}{4} \text{ and } \gamma = \frac{1}{2} - \alpha. \tag{3.20}$$

The method reduces to the Newmark method for $\alpha = 0$. The HHT method has been extensively analyzed with respect to stability and dissipative properties by Hughes [41].

Solution of the System of Equations

The resulting system of equations is a non-linear set of equations, which needs to be linearized. The solution of the system is sought by employing the Newton-Raphson method and the problem becomes a root finding problem where the solution is progressed iteratively from iteration k to $k+1$. For a system of equations represented as $A\phi = b$ the Newton-Raphson iteration process is represented as

$$\phi^{k+1} = \phi^k - \left[\frac{\partial r(\phi^k)}{\partial \phi}\right]^{-1} r(\phi^k) \text{ with } r(\phi^k) = A\phi^k - b \tag{3.21}$$

where $r(\phi^k)$ represents the residual at the k^{th} iteration. The resulting system can be solved with a suitable algorithm for the linear equation system. This work employs a direct solver based on the LU factorization for this purpose.

3.3 Solution of Coupled Fluid-Structure Problem

The solution methods to solve individual subproblems of a coupled FSI problem have already been defined. In this work the FSI simulations have been performed employing an implicit partitioned coupling algorithm, which is described in the following section.

3.3.1 Implicit Partitioned Coupling Algorithm

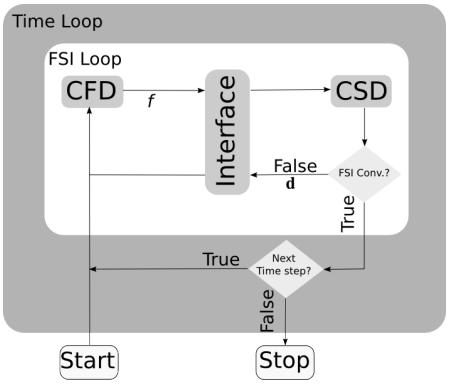

Fig. 3.2: A schematic representation of the implicit partitioned coupling algorithm

In a partitioned coupling strategy, the fluid-solid interface $\Sigma = \Gamma_S \cap \Gamma_F$ is treated with the following coupling conditions

$$d_i^f = \vartheta_i^s \tag{3.22}$$

$$u_i^f = \dot{\vartheta}_i^s \tag{3.23}$$

$$\sigma_{ij}^s = \sigma_{ij}^f \tag{3.24}$$

where superscript f and s represent the fluid and the solid quantities, d_i^f are displacements at the interface on the fluid subdomain, σ_{ij} represents the Cauchy stress tensor and u_i^f is the fluid velocity at the interface.

Let $\mathcal{F} : d \mapsto f$ be the mapping of the interface displacements to forces by the fluid solver $\mathcal{F}$ and $\mathcal{S} : f \mapsto d$ be the mapping of forces to displacements by the structural solver $\mathcal{S}$, where d and f represent displacements and forces at the interface, respectively. In an iterative coupling strategy, the two mappings can be represented as

$$\tilde{f}_i^{k+1} = \mathcal{F}(d_i^k) \text{ and } \tilde{d}_i^{k+1} = \mathcal{S}(f_i^k), \tag{3.25}$$

where a tilde on $\tilde{d}^{k+1}$ and $\tilde{f}^{k+1}$ represents the intermediate result before forces and displacements are used to perform the next iteration and k is the iteration number of the coupling algorithm. The Implicit Coupling algorithm used in this work is represented in figure 3.2. The coupling procedure starts with the solution of the fluid subproblem with the flow solver FASTEST [2]. The calculated forces at the interface are then transferred to the coupling

software MpCCI [1] or preCICE [9], which handles the data transfer and interpolation between non-matching grid interfaces. The interpolated forces are then passed to the structural solver FEAP [108], and the structural subproblem is solved. The resulting displacements from the structural solver are tested for convergence. If the convergence criterion is not satisfied, displacements are sent to the fluid solver through the coupling interface and another iteration of the process starts with an updated fluid grid. The process continues until the convergence criterion is satisfied, after which either the next time step of the coupled process is calculated or the simulation is finished.

The convergence criterion is based on the residual of the structural displacements between two successive iterations of the coupling algorithm as

$$r^{k+1} = ||\tilde{d}_i^{k+1} - d_i^k|| < \epsilon \tag{3.26}$$

where r^{k+1} defines the residual at iteration $k+1$, $||.||$ defines a suitable norm (e.g. L_2 norm) and ϵ is the convergence criterion for the coupled process.

Under-relaxation and Coupling Acceleration Algorithms

Partitioned coupling algorithms are known to be unstable under certain physical and geometrical conditions. Among known issues to effect the convergence of coupling scheme is the Artificial Added Mass effect [10] in FSI with incompressible flow simulation. The implicit coupling algorithm deals with the instability by employing a relaxation technique for displacements from the structural solver, and the iterative coupling technique ensures a balance of energy at the interface. The under-relaxation factor $\omega^{FSI} : 0 < \omega^{FSI} < 1$ is used for the structural displacements as

$$d_i^{k+1} = \omega^{FSI} \tilde{d}_i^{k+1} + (1 - \omega^{FSI}) d_i^k. \tag{3.27}$$

However, where the under-relaxation helps to stabilize the coupling scheme, it may also slow down the convergence. Another issue is finding an optimal value for the relaxation parameter, which is problem dependent, and is not known a priori. The dynamic under-relaxation methods like IQN-ILS [15] and Aitken method [52, 42] can be more helpful in this regard, absolving the user of finding an optimal value for maximum acceleration of the convergence. The Aitken method uses the information from two previous iterations to calculate the ω^{FSI} dynamically in every coupling iteration as

$$\omega^{FSI,k+1} = -\omega^{FSI,k} \frac{(\Delta d_i^k)^T (\Delta d_i^{k+1} - \Delta d_i^k)}{(\Delta d_i^{k+1} - \Delta d_i^k)^2}, \tag{3.28}$$

where

$$\Delta d_i^k = \tilde{d}_i^k - d_i^{k-1} \quad \text{and} \quad \Delta d_i^{k+1} = \tilde{d}_i^{k+1} - d_i^k.$$

An estimation of forces or displacements at the start of a coupling iteration, also helps accelerate the convergence. For this purpose, information about forces or displacements from previously calculated time steps is used to predict forces or displacements at the interface, before start of the calculation for a new time step, for details see [88].

3.3.2 Grid Movement

The fluid solver FASTEST employs an ALE formulation on block-structured and body-fitted grids where the grid needs to be updated in every iteration of the coupling algorithm. The grid movement and update in FASTEST is performed block-wise, while the grid is only moved and updated but the grid topology remains unchanged. The grid deformation is defined by the user and works on a bottom to top strategy in three stages. First the edges are updated either with a linear interpolation or a cubic spline approximation, which preserves the angle between edge and the face it connects. In the second stage, the block face mesh is regenerated with a linear, transfinite [31] or an elliptic [99] grid generation method. Once the edge and block face mesh has been updated, the volume grid of the block is updated, which can be done with a linear, transfinite or an elliptic grid generation method. The input for the grid update strategy must also resolve the inter block dependencies as well. More details about implementation of these methods in the fluid solver FASTEST can be found in [78].

Chapter 4
Turbulence and Turbulence Modeling

Turbulence is a behavior of fluid motion, which manifests itself by pseudo-random fluctuations of the flow quantities. The turbulent behavior of fluids is present in many naturally occurring and industrial flow applications, e.g. atmospheric flow, the flow in circulatory and respiratory systems of animals and the flow through pipes and jet engines, to name a few. The analytical methods to study the phenomenon are rendered inefficient due to the complexity of the problem. On the other hand, experimental methods are becoming more and more reliable. But even the measurement techniques might not be able to give all important information about the turbulence in flow, specially in complex geometries where placing an instrument might not be feasible or cost efficient. Alternative to experimental methods, numerical techniques to simulate the turbulent flow are becoming popular with the help of rapid advancements in computational technology, while the role of experimental setups is becoming important for generating data to validate turbulence modeling approaches.

This chapter gives a short description of the important physical aspects of turbulence and techniques to model the turbulence in fluid flows. The chapter has two main sections, the first section concerns the physics of turbulence, while the second section is concerned with the description of models employed in this work. The theory of turbulence described here is based on information provided in the textbook by Pope [80].

4.1 Physical Background

It is often claimed that turbulence lacks a single comprehensive definition, and researchers are inclined to define turbulent flow in terms of characteristics of the flow. The turbulence in flow is characterized most notably by: pseudo-random fluctuations of flow quantities, higher diffusion and dissipation rates and the presence of strong 3-dimensional vorticity. These random fluctuations can be observed in smoke from a cigarette, where initially the

smoke rising from the cigarette can exhibit a very smooth and laminar behavior, and after some distance the smoke can become turbulent and exhibit randomness, before mixing completely into the surrounding air. The investigation of this phenomenon of laminar to turbulent transition, was performed by O. Reynolds [84] in 1883, by injecting a dye streak in a water channel with smooth transparent walls. His observations led to the identification of a single non-dimensional parameter now called the Reynolds number Re defined as

$$Re = \frac{\mathcal{U}\mathcal{L}}{\nu} , \tag{4.1}$$

where $\mathcal{U}$ and $\mathcal{L}$ are the velocity and length scale, and $\nu = \mu/\rho$ is the kinematic viscosity of the fluid. The Reynolds number is the ratio of inertial to viscous forces, which can help to identify whether a flow would be turbulent or laminar. For example, based on the Reynolds Number many different flow regimes can be identified for a flow over a circular cylinder [105]. The flow in a cylinder wake starts becoming turbulent for $Re > 200$, while this transition to turbulence for the boundary layer flow over a cylinder starts for approximately $Re > 300,000$. The flow regime $300 < Re < 300,000$ is called sub-critical as the boundary layer flow over a cylinder is laminar while the wake flow is fully turbulent.

Turbulence is also associated with enhanced transport and mixing properties of the flow. This phenomena of mixing is much desired in many industrial applications, like mixing of different reactants in combustion devices. A turbulent flow can also transport heat better than a laminar flow, which is a design consideration for cooling devices that use fluids to transport heat. Higher transport rates of momentum also cause friction drag to increase as a result of higher wall shear compared to a laminar flow, which is an undesired situation. An increase in drag causes a drop in the fuel economy in aircrafts, for this reason a reduction of the friction drag is an active research topic in aircraft industry.

Lewis F. Richardson in 1922 [87] proposed the idea of an *energy cascade*, which tries to explain the transfer of energy from large scale turbulent motions to smaller and smaller scales, before these turbulent motions get dissipated under the action of viscosity. Richardson summarized his idea in a poetic way:

> Big whorls have little whorls,
> Which feed on their velocity;
> And little whorls have lesser whorls,
> And so on to viscosity.

Andrei N. Kolmogorov in 1941 published three papers [49, 50, 51], which are very important to the modern ideas and understanding of the turbulence. Kolmogorv extended the ideas proposed by Richardson with identification of the smallest scales possible, which are then named after him. These ideas played an important role for the development of modeling approaches in the

second half of the 20^{th} century, and hence are briefly described in the next section.

4.1.1 Turbulent Scales and Energy Cascade

Richardson viewed turbulence in fluids to be composed of eddies with different sizes, and proposed that smaller eddies are produced as a result of instability and breakup of large eddies. The smaller eddies can undergo similar breakup process and transfer their energy to even smaller eddies, until the Reynolds number based on length and velocity scale is small enough for a stable eddy motion and molecular viscosity can effectively dissipate these small scale motions. The largest eddies have characteristic length scale l_o and velocity scale u_o, comparable to the length and velocity scale of the flow $\mathcal{L}$ and $\mathcal{U}$ respectively. Consequently the Reynolds number for these eddies is also comparable to the Reynolds number of the flow, so the effect of viscosity on these scales is negligible. The time scale of these motions τ_o associated with the velocity and length scale is l_o/u_o. The rate at which the energy is dissipated is also determined by the rate of energy transfer from these large scale motions. The kinetic energy of these large scale motions is of the order of u_o^2, hence the rate of energy transfer or dissipation ϵ can be considered to scale as $u_o^2/\tau_o = u_o^3/l_o$. In accordance with the experimental observations, this indicates that ϵ scales as u_o^3/l_o, independent of ν.

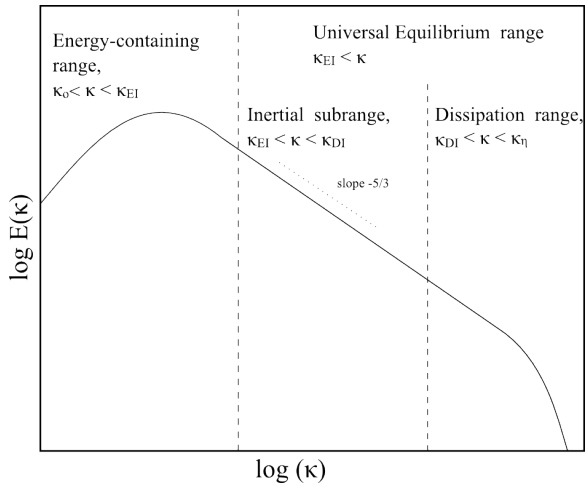

Fig. 4.1: Schematic representation of turbulent energy spectrum.

Richardson's theory of energy cascade explains the energy transfer mechanism, but does not address the issue related to the size of turbulent scales. Kolmogorov explored this matter and many more with his theory which he stated in the form of three hypotheses. The first hypothesis concerns the local isotropy of turbulent scales. Kolmogorov suggested that the large scale motions are anisotropic and are influenced by the flow topology, while this anisotropy is lost through the breakup process that results in smaller motion scales. Not only does the directionality but also the geometric information of the large scales is lost, as a consequence the smaller scales have a universal state. The second similarity hypothesis of Kolmogorov states the dependence of these small scale motions on the viscosity ν and the energy dissipation rate ϵ. Consider l_{EI} to be the size of smallest anisotropic eddies, then according to Kolmogorov, $l < l_{EI}$ is referred to as *universal equilibrium range*, as shown in the figure 4.1 for wave-number $\kappa > \kappa_{EI}$. Based on this hypothesis the smallest possible length scale η, called the Kolmogorov length scale, and the corresponding velocity and time scale, u_η and τ_η respectively, can be uniquely determined as

$$\begin{aligned} \eta &= \left(\frac{\nu^3}{\epsilon}\right)^{\frac{1}{4}}, \\ u_\eta &= (\epsilon\nu)^{\frac{1}{4}}, \\ \tau_\eta &= \left(\frac{\nu}{\epsilon}\right)^{\frac{1}{2}}. \end{aligned} \tag{4.2}$$

It can be readily observed that the Reynolds number for Kolmogorov scales is unity i.e. $\eta u_\eta/\nu = 1$, which is consistent with the notion that the breakup of large scales to small scales results in a reduction of Reynolds number to an extent where dissipation is effective. Another inference from the hypothesis is that for a sufficiently high Reynolds number flows the small scales are statistically identical when normalized with the Kolmogorov scales.

Using the definition of Kolmogorov scales and $\epsilon \sim u_o^3/l_o$, the ratio of smallest to largest scales can be determined as

$$\begin{aligned} \frac{\eta}{l_o} &\sim Re^{-3/4}, \\ \frac{u_\eta}{u_o} &\sim Re^{-1/4}, \\ \frac{\tau_\eta}{\tau_o} &\sim Re^{-1/2}. \end{aligned} \tag{4.3}$$

It is evident from the relations above that the ratio η/l_o decreases with increasing Reynolds number. This means a wide range of scales can be identified between η and l_o, with increasing Re. The third hypothesis from Kolmogorov states that for a sufficiently high Reynolds number turbulent flow, the motion of scales with length $l : l_o \gg l \gg \eta$ has a universal form that is determined by

ϵ, independent of ν. This further divides the *universal equilibrium range* into the *inertial subrange* and the *dissipation range*, with a demarcation wavenumber κ_{DI} as shown in figure 4.1. The energy spectrum in the inertial subrange follows a power law, (as represented in figure 4.1) which is written as

$$E(\kappa) = C_K \kappa^{-5/3} \epsilon^{2/3}, \tag{4.4}$$

also referred to as Kolmogorov's 5/3 law.

This picture of turbulence has important consequences for the turbulence modeling and the understanding of influences from assumptions made to develop these models.

4.1.2 Wall Vicinity

Solid impermeable boundaries are part of many flow devices known to us, both external and internal, e.g. flow through channels, pipes and jets. The discussion above pertaining to the energy cascade and turbulent scales does not consider the presence of solid boundaries. The principal effect of wall vicinity on turbulence is the damping of fluctuations in velocity normal to the wall. The energy of these fluctuations gets redistributed to the tangential velocity components. As a result, the turbulence close to the wall is highly anisotropic, and the isotropy is recovered with an increasing distance from the wall. Also the viscosity effects are more dominant very close to walls.

Apart from the instantaneous turbulent characteristics of the flow in a wall vicinity, the mean flow shows a universal character in the turbulent boundary layer flow. This universality of the mean flow is also referred to as the *law of wall*. The universal character is defined with normalized quantities in terms of wall shear stress τ_w, defined as

$$\tau_w = \mu \left(\frac{\partial u}{\partial y} \right)_w , \tag{4.5}$$

where the subscript w indicates a velocity gradient at the wall, y is assumed to be the wall normal direction and u is a velocity in wall tangential direction. Further using the wall shear stress, the friction velocity is defined as

$$u_\tau = \sqrt{\frac{\tau_w}{\rho}}. \tag{4.6}$$

The friction velocity is used to normalize the velocity and wall normal distance as

$$y^+ = \frac{u_\tau y}{\nu} \quad , \quad u^+ = \frac{u}{u_\tau}, \tag{4.7}$$

where such a scaling is also called the *wall normal units*. The wall friction Reynolds number Re_τ is defined as

$$Re_\tau = \frac{u_\tau \delta}{\nu}, \tag{4.8}$$

where δ represents the boundary layer thickness. A description of different regions in boundary layer flow, identified by y^+ and y/δ is given by Pope [80], a short summary is given in the following:

Inner Layer ($y/\delta < 0.1$): The mean velocity profile is determined by u_τ and y^+, independent of the bulk inflow velocity and the boundary layer thickness δ.

Viscous wall region ($y^+ < 50$): The viscous contribution to shear stress is significant.

Viscous sublayer ($y^+ < 5$): The Reynolds shear stress is negligible compared to the viscous stress. The velocity profile is linear, given as

$$u^+ = y^+. \tag{4.9}$$

Outer layer ($y^+ > 50$): The effect of molecular viscosity on the mean velocity profile is negligible.

Overlap region ($y^+ > 50$ and $y/\delta < 0.1$): The region where inner ($y/\delta < 0.1$) and outer $y^+ > 50$ boundary layers overlap, which occurs only for high Re flows.

Log-law region ($y^+ > 30$ and $y/\delta < 0.3$): The normalized velocity profile shows a universal character described by the log law as

$$u^+ = \frac{1}{\kappa}\ln(y^+) + B, \tag{4.10}$$

where $\kappa = 0.41$ is known as the von Kármán constant and $B = 5.2$. The mean velocity profile with a DNS data from a channel flow at $Re_\tau = 590$ is plotted along with results from equation (4.9) and (4.10) in figure 4.2.

Buffer Layer ($5 < y^+ < 30$): The region between viscous sublayer and the log-law region.

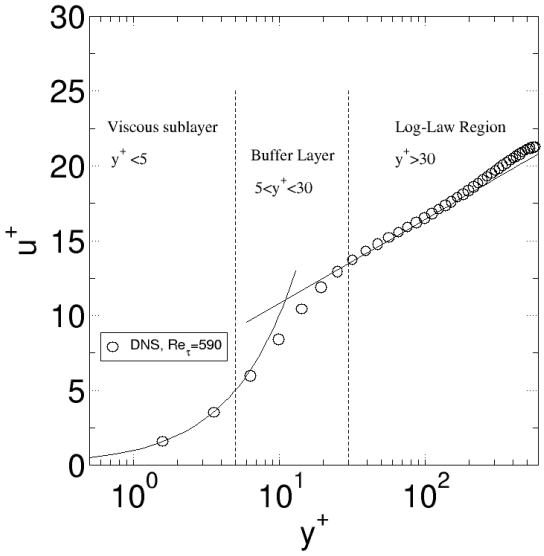

Fig. 4.2: Velocity profile for channel flow at $Re_\tau = 590$, Direct Numerical Simulation (DNS) data from Moser et al. [69], solid line from equations (4.9) and (4.10).

4.2 Turbulence Modeling

Simulation of the turbulent fluid motion poses a challenging task, mainly due to the wide range of scales present in a turbulent flow. The effects of turbulent flow can be represented in a simulation with a wide variety of methods, depending upon the information required and the purpose of simulation. These methods have their own advantages and shortcomings, in terms of the computational cost and the simulation quality. In principle, resolving turbulent scales to the smallest extent is possible to achieve a perfect accuracy and the highest level of details about a flow, in practice such simulations would require unreasonable computational resources.

4.2.1 Direct Numerical Simulation (DNS)

Though DNS can not be classified as a modeling approach as it resolves the turbulence in the flow rather than modeling the effect of turbulence, it is still included here for completeness. The properties of the turbulent flow discussed in previous sections can shed some light on why a DNS is computationally the most expensive technique. It has been discussed that the

smallest known length scales i.e. the Kolmogorov scales, decrease in length with an increasing Reynolds number, which means that the computational cost of a DNS increases with an increase in Reynolds number. For isotropic turbulence, the computational cost based on a required number of grid points and time steps has been found to be proportional to $160Re_{l_o}^3$ or $0.55Re_\lambda$, by Pope [80]. For non-isotropic flows, this required number of grid points increases even more quickly.

Apart from stringent demands on resolution in space and time, adequate numerical schemes and appropriate boundary conditions are required for an accurate DNS. The DNS is definitely not an appropriate technique to be employed in the design process, but the use of DNS is important for the fundamental turbulence research. An important use of the DNS method is to generate data for validation and calibration of methods to model turbulence.

4.2.2 Reynolds Averaged Navie-Stokes (RANS) Modeling

The information about instantaneous turbulent flow is often not necessary and a mean flow information is what is desired in many industrial applications. The RANS equations form the basis for a statistical modeling of the turbulence. These equations are derived from Navier-Stokes equations by using the Reynolds decomposition, where a fluctuation quantity $\phi(x_i, t)$ is divided into an ensemble or a time averaged part $\bar{\phi}$ and a fluctuation part ϕ' as

$$\phi(x_i, t) = \bar{\phi}(x_i) + \phi'(x_i, t). \tag{4.11}$$

The Reynolds decomposition in this sense is an assumption that the turbulent flow has a statistical steady state and all fluctuations are about a mean quantity. The application of such a process to Navier-Stokes equations results in the so called Reynolds averaged Navier-Stokes equations. The Reynolds averaging process applied to NS equations (2.4) and (2.5), leads to the Reynolds averaged continuity and momentum equation, given as

$$\frac{\partial \bar{u}_i}{\partial x_i} = 0 \,, \tag{4.12}$$

$$\frac{\partial \rho \bar{u}_i}{\partial t} + \frac{\partial \rho \bar{u}_i \bar{u}_j}{\partial x_j} = \frac{\partial}{\partial x_j}\left[\mu\left(\frac{\partial \bar{u}_i}{\partial x_j} + \frac{\partial \bar{u}_j}{\partial x_i}\right) - \bar{p}\delta_{ij}\right] - \frac{\partial \overline{\rho u_i' u_j'}}{\partial x_j} + \rho f_i \,. \tag{4.13}$$

These equations are similar in form to Navier-Stokes equations except the fact that these equations are written for the time averaged quantities and $\overline{\rho u_i' u_j'}$ has emerged as an extra term in these equations. This term is called the Reynolds stress tensor and describes the influence of turbulent fluctuations on mean quantities. The emergence of the Reynolds stress tensor gives rise

to the so called closure problem, i.e. there are more unknowns than number of equations. Even though the equations can be derived for six components of the Reynolds stress tensor, but solving such a system adds significant additional costs and numerical difficulties.

In a RANS modeling approach Reynolds stresses are approximated based on the Boussinesq hypothesis [4]. According to the hypothesis, the momentum transfer caused by turbulent eddies can be modeled with an eddy viscosity. This is analogous to the quantification of momentum transfer caused by molecular motion, based on the molecular viscosity in a gaseous fluid. The Boussinesq relationship for the Reynolds stress tensor is written as

$$\rho\overline{u_i' u_j'} = -2\mu_t(S_{ij}) + \frac{2}{3}\rho\delta_{ij}k, \tag{4.14}$$

where the turbulent kinetic energy k and the strain rate tensor S_{ij} are defined as

$$k = \frac{1}{2}(\overline{u_i' u_i'}) \quad \text{and} \quad S_{ij} = \frac{1}{2}\left(\frac{\partial \bar{u}_i}{\partial x_j} + \frac{\partial \bar{u}_j}{\partial x_i}\right) \quad \text{respectively,}$$

and μ_t is the turbulent eddy viscosity assumed as an isotropic scalar quantity. It has been mentioned in the previous section that turbulence at large scales is anisotropic under the influence of geometric and boundary constraints. This contradicts with isotropic assumption of the eddy viscosity. However, despite this contradiction with a physical observation, the hypothesis has been widely used to approximate Reynolds stresses in many widely used turbulence models. The turbulence models that provide the eddy viscosity as a scalar to close RANS equations are also known as eddy viscosity models (EVM). There is a significant number of turbulence models used for approximation of the turbulent eddy viscosity, which can be characterized based on different levels of physical approximation and mathematical complexity. The most widely used models are the one equation S-A model [97] and the two equation $k-\epsilon$ model [11], to name a few.

FASTEST has several two-equation models available and a four equation turbulence model $k-\epsilon-\zeta-f$ model [32]. The $k-\epsilon-\zeta-f$ model is employed to conduct FSI simulations in this study and is discussed in the following section.

4.2.2.1 $k-\epsilon-\zeta-f$ model for RANS

The $k-\epsilon-\zeta-f$ model [32] is based on Durbin's elliptic relaxation concept [21], which makes use of the wall normal velocity scale $\zeta = v^2/k$ sensitized by an elliptic relaxation parameter to model wall blocking effects, with v being the wall normal velocity fluctuation. The turbulent viscosity is calculated as

$$\nu_t = C_\mu \zeta k \tau, \tag{4.15}$$

where τ defines a time scale of turbulence and C_μ is a model constant . The calculation of turbulent viscosity requires the turbulent kinetic energy k, dissipation rate ϵ and the wall normal velocity scale ζ. The three transport equations for k, ϵ and ζ together with an equation for the elliptic relaxation function f are given as

$$\frac{Dk}{Dt} = \mathcal{P} - \epsilon + \frac{\partial}{\partial x_i}\left[\left(\nu + \frac{\nu_t}{\sigma_k}\right)\frac{\partial k}{\partial x_i}\right], \tag{4.16}$$

$$\frac{D\epsilon}{Dt} = \frac{C_{\epsilon 1}\mathcal{P} - C_{\epsilon 2}\epsilon}{\tau} + \frac{\partial}{\partial x_i}\left[\left(\nu + \frac{\nu_t}{\sigma_\epsilon}\right)\frac{\partial \epsilon}{\partial x_i}\right], \tag{4.17}$$

$$\frac{D\zeta}{Dt} = \underbrace{f}_{f_{source}} - \frac{\zeta}{k}\mathcal{P} + \frac{\partial}{\partial x_i}\left[\left(\nu + \frac{\nu_t}{\sigma_\zeta}\right)\frac{\partial \zeta}{\partial x_i}\right], \tag{4.18}$$

$$L^2\nabla^2 f - f = \frac{1}{\tau}\left(c_1 + C_2{}'\frac{\mathcal{P}}{\epsilon}\right)\left(\zeta - \frac{2}{3}\right), \tag{4.19}$$

where $\mathcal{P}$ is the production of turbulent kinetic energy, while L and τ are the length and time scales limited by the Kolmogorov scales as a lower bound and by Durbin's realizability constraints [20] as an upper bound, defined as

$$\tau = \max\left[\min\left(\frac{k}{\epsilon}, \frac{a}{\sqrt{6}C_\mu|S|\zeta}\right), C_\tau\left(\frac{\nu^3}{\epsilon}\right)^{1/2}\right], \tag{4.20}$$

$$L = C_L \max\left[\min\left(\frac{k^{3/2}}{\epsilon}, \frac{k^{1/2}}{\sqrt{6}C_\mu|S|\zeta}\right), C_\eta\left(\frac{\nu^3}{\epsilon}\right)^{1/4}\right]. \tag{4.21}$$

The model coefficients are:

$$\begin{aligned} C_\mu = 0.22, \quad C_{\epsilon 1} = 1.4(1 + 0.012/\zeta), \quad C_{\epsilon 2} = 1.9, \quad c_1 = 0.4, \\ C_2' = 0.65, \quad \sigma_k = 1, \quad \sigma_\epsilon = 1.3, \quad \sigma_\zeta = 1.2, \\ C_\tau = 6.0, \quad , C_L = 0.36, \quad C_\eta = 85, \quad , a = 0.6 \quad . \end{aligned} \tag{4.22}$$

A major advantage of the $k - \epsilon - \zeta - f$ model is the ability to account for the near wall anisotropic behavior of turbulence without the use of damping functions, contrary to the use of empirical damping functions for a calculation of the viscosity in the low-Re model of Chien [11]. The use of Durbin's realizability for the time scale τ also solves the problem of the stagnation point anomaly [20], which is known to cause excessive production of the turbulent kinetic energy after a stagnation point in bluff body flows.

4.2.3 Large-Eddy Simulation (LES)

DNS and RANS lie at the extreme ends of the turbulence simulation spectrum. On the other hand, aim of the large-eddy simulation is a partial resolution of turbulent scales of motion. The physical justification behind a partial resolution of turbulent scales comes from Kolmogorov's self similarity hypothesis, which states that at large scales the turbulence exhibits an anisotropic character, while the small scales have a more universal isotropic character. This makes a compelling argument for the modeling of small scales, based on their universal character. Also as the large scale motions carry most of the energy and their effect on the transport phenomena and mixing is much more prominent than the small scales, resolving them is more important for accurate predictions of the flow. The idea was initially proposed by Smagorinsky [93] for an atmospheric flow simulation.

A spatial filtering approach is used to separate large scale motions also called the grid scale, from small scales also called the sub-grid scales (SGS). The filtering operation results in the following decomposition of a general flow variable

$$\phi(x_i, t) = \bar{\phi}(x_i, t) + \phi'(x_i, t), \tag{4.23}$$

where $\bar{\phi}$ represents a large scale filtered or a resolved part of the quantity, while ϕ' represents the small scale fluctuations from the filtered value. The filtering operation when applied to Navier-Stokes equations leads to the filtered equations written as

$$\frac{\partial \bar{u}_i}{\partial x_i} = 0 \,, \tag{4.24}$$

$$\frac{\partial \rho \bar{u}_i}{\partial t} + \frac{\partial \rho \bar{u}_i \bar{u}_j}{\partial x_j} = \frac{\partial}{\partial x_j}\left[\mu\left(\frac{\partial \bar{u}_i}{\partial x_j} + \frac{\partial \bar{u}_j}{\partial x_i}\right) - \bar{p}\delta_{ij}\right] - \frac{\partial \tau_{ij}}{\partial x_j} + \rho f_i \,, \tag{4.25}$$

where τ_{ij} is the sub-grid scale stress and is given as

$$\tau_{ij} = \overline{u_i u_j} - \bar{u}_i \bar{u}_j. \tag{4.26}$$

The filtered Navier-Stokes equations look similar in form to the RANS equations given in the previous section, except the fact that Reynolds stress tensor $\rho u_i' u_j'$ has been replaced by the SGS stress term τ_{ij}. Regardless of the similarity in form, the averaging process and the filtering process are different. In the filtered Navier-Stokes equations, the fields involved i.e. $\bar{u}_i, \bar{p}$ and τ_{ij} are random, three dimensional and unsteady, even if the flow is statistically stationary or homogeneous.

The filtered equations, as the RANS equations, have a closure problem arising with the emergence of SGS stress τ_{ij}. This term is approximated using the Boussinesq hypothesis to relate SGS stresses to the strain rate tensor, as with the RANS modeling approach. The sub-grid scale eddy viscosity is then approximated by a LES model. As mentioned earlier the idea was first proposed by Smagorinsky in 1963 for the simulation of an atmospheric flows,

but the first application to a three dimensional wall bounded turbulent flow in a channel was presented by Deardorff in 1970 [13]. The model proposed is still the most popular model for performing a LES and is named after Smagorinsky. The Smagorinsky model estimates the sub-grid scale eddy viscosity as

$$\nu_{SGS} = (C_s\Delta)^2 S^*, \tag{4.27}$$

where $S^* = \sqrt{2S_{ij}S_{ij}}$, C_s is the model constant with a value between 0.065 and 0.2 depending on the flow. The filter-width Δ for LES has been calculated differently by various researchers. However, in this work the filter-width is calculated as a cube root of the product of individual grid spacings, as suggested by Deardorff [13]

$$\Delta = \sqrt[3]{\Delta_x\Delta_y\Delta_z}. \tag{4.28}$$

The model has a number of inherent deficiencies, one of which has already been mentioned, i.e. a model constant should really be a constant and not flow dependent. The model does not recover the correct behavior close to walls, normally this problem is circumvented by introducing the van Driest damping [117] for the expression for SGS viscosity. These problems were addressed by a dynamic calculation of the Smagorinsky constant C_s by Germano et al. [26]. The method calculates appropriate values of $C_s = C_s(x_i, t)$ locally in space and time using a test-filter. In this work the dynamic Smagorinsky constant is estimated by a least squares method as suggested by Lilly [60]. For further details about LES modeling the reader can refer to [89],[77].

LES puts stringent requirements on grid resolution and time step sizes. According to Piomelli [77] in a wall resolved LES the grid needs to fulfill $y^+ < 2$ in the wall normal direction and in stream-wise and span-wise directions the grid must be of the order of $\Delta x^+ \simeq 50 - 150$ and $\Delta z^+ \simeq 15 - 40$, assuming a bulk flow in x-direction. Even though the aim of an LES is to model small scale isotropic turbulence, the wall resolved LES still remain very expensive. The situation can be improved with a wall modeled LES, where the use of wall functions can relax the grid requirements in a near wall region.

4.2.4 Hybrid RANS-LES approach

The RANS predictions lack the accuracy required for flows dominated by large scale anisotropic flow structures such as the wake flow behind a bluff body. While the LES approach is a good candidate to handle these kind of flows, but a wall resolved LES can be very expensive for wall bounded flows due to grid requirements to resolve a boundary layer flow. In a hybrid RANS-LES approach the LES model is coupled with a RANS model to reduce the computational costs drastically. Many different approaches have been suggested and used for different flow configurations, which can be categorized

into zonal and non-zonal approaches. In a zonal approach, the application region for RANS or LES is defined by the user before the start of a simulation. While in a non-zonal approache, region for a RANS or a LES application is identified by the model itself depending upon the flow. A detailed overview of hybrid RANS-LES methods is provided in [25].

The most popular hybrid RANS-LES method is the *detached-eddy simulation* (DES) model proposed by Spalart in 1997 [96]. The DES method until now has been used with many different RANS turbulence models. The DES model is a non-zonal approach, where a RANS model is modified so that an LES is performed in regions where grid is fine enough to support it. The model performs a RANS calculation near solid boundaries, and switches to the LES mode away from walls, where the grid can support a LES. The switching between two modes is actuated by introducing a length scale into the RANS model equations, which is defined as

$$l_{DES} = \min(l_{RANS}, C_{DES}\Delta), \tag{4.29}$$

where $l_{RANS} = k^{3/2}/\epsilon$ is the integral length scale from a RANS turbulence model, Δ defines the length scale for the LES mode, and C_{DES} is the model constant. The model switches between a RANS or a LES mode based on the two length scales used to define l_{DES}. The original DES formulation exhibited some short-comings, which were later circumvented by a proposal of the *delayed detached-eddy simulation model* (DDES) [95]. This work employs the DDES model based on the $k-\epsilon-\zeta-f$ RANS model [32] for FSI simulations, which is discussed in the following section.

4.2.4.1 $k-\epsilon-\zeta-f$ based DDES

In this work the delayed detached-eddy simulation (DDES) model with the $k-\epsilon-\zeta-f$ as a baseline RANS model is used to perform hybrid RANS-LES simulations. The $k-\epsilon-\zeta-f$ model has been adapted to work as a DDES in [83, 116]. An expression for the RANS length scale is used to replace the dissipation term (ϵ) in k equation (4.16) to involve the length scale as $\epsilon = k^{3/2}/l_{RANS}$. The k equation after the modification can be written as

$$\frac{Dk}{Dt} = \mathcal{P} - \underbrace{\frac{k^{3/2}}{l_{RANS}}}_{\text{dissipation}} + \frac{\partial}{\partial x_i}\left[\left(\nu + \frac{\nu_t}{\sigma_k}\right)\frac{\partial k}{\partial x_i}\right]. \tag{4.30}$$

The length scale in the above equation is replaced with the DDES length scale l_{DDES} defined as

$$l_{DDES} = l_{RANS} - f_d \max(0, l_{RANS} - l_{LES}), \tag{4.31}$$

where l_{LES} represents the LES length scale defined as: $l_{LES} = C_{DES}\Delta\psi$, with C_{DES} being the model constant and ψ is the low Reynolds correction term which is derived and tested in [83] and is given as

$$\psi^2 = \min\left(100, \left(\frac{C_{\epsilon 1}}{C_{\epsilon 1} C_\mu \zeta}\right)\right). \tag{4.32}$$

A calibration study of the model constant C_{DES} in [83] suggests a value of 0.2 for the model constant. The term f_d in (4.31) represents the shielding function given as

$$f_d = 1 - \tanh([8r_d^3]), \;\; r_d = \frac{\nu_t + \nu}{\kappa^2 d_w^2 \max\left(10^{-10}, \sqrt{\frac{\partial u_i}{\partial x_j}\frac{\partial u_i}{\partial x_j}}\right)}, \tag{4.33}$$

where d_w represents the normal wall distance. For a detailed description and model validation the reader can refer to [83].

4.3 Extensions to Turbulence Modeling

The following sections discuss extensions to the turbulence modeling in FASTEST, during this work.

4.3.1 Modification to $k - \epsilon - \zeta - f$ model

Modifications were proposed by Davidson [12] for original formulation of the $v^2 - f$ model to limit $v^2 < 2k/3$. The modified model produced a better agreement for the wall normal stress v^2 in channel flows, specially in the equilibrium logarithmic layer, where $\zeta \approx 0.4$. Following same arguments, modifications are made to the ζ equation in the $k - \epsilon - \zeta - f$ model.

The elliptic relaxation parameter f in the ζ equation (4.18) models the pressure strain term. The normal wall stress modeled by ζ should be smaller than other two normal stresses due to the wall blocking effect and also ζ should be less than 2/3. In a homogeneous flow away from walls, the Laplace term in equation (4.19) is expected to be negligible, i.e. $\nabla^2 f \rightarrow 0$ so the equation reduces to

$$f_{hom} = -\frac{1}{\tau}\left(c_1 + {C_2}'\frac{\mathcal{P}}{\epsilon}\right)\left(\zeta - \frac{2}{3}\right). \tag{4.34}$$

As it turns out the Laplace term does not go to zero far away from walls as a consequence ζ gets too large away from walls. A simple modification suggested in [12] is to limit the f source term in the ζ equation by f_{hom} as

$$f_{source} = \min\left(f, f_{hom}\right) \tag{4.35}$$

Further it is argued that in regions, where $\zeta \approx 2/3$, the turbulent viscosity from the current model gets considerably large than the standard value of the $k-\epsilon$ model. So, a modification to the turbulent viscosity is made to limit the value by the standar $k-\epsilon$ value of viscosity as

$$\nu_t = \min\left(C_\mu \zeta k \tau, 0.09\frac{k^2}{\epsilon}\right), \tag{4.36}$$

where $0.09k^2/\epsilon$ is the tubulent viscosity from the $k-\epsilon$ model.

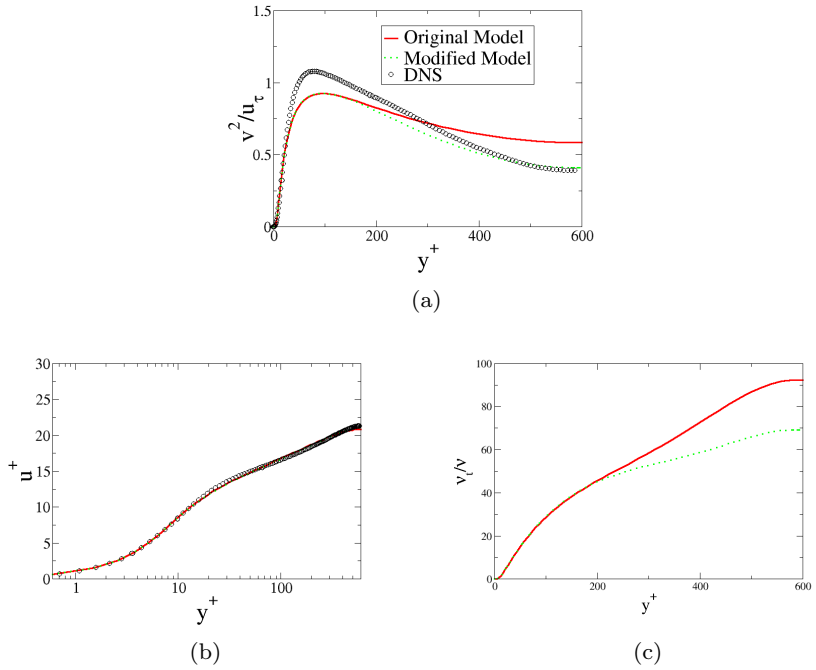

Fig. 4.3: Comparison between original and modified $k-\epsilon-\zeta-f$ model for: (a) v^2/u_τ, (b) u^+ and (c) ν_t/ν. DNS data for $Re_\tau = 590$ [69].

The modified model is tested against the original model for a 2-d channel flow test case at $Re_\tau = 590$. The channel half width is discretized with 64 cells in the wall normal direction with 1^{st} cell $y^+ \approx 0.5$. Figure 4.3 shows the comparison between original and modified models, with the DNS data from [69]. The velocity profile u^+ for both models does not show any significant difference. However, prediction of the wall normal Reynold stress v^2 has significantly improved with the modification, specially away from the wall near

the channel half width as shown in figure 4.3a. Both models predict similar values of the turbulent viscosity in the near wall region, while differences occur away from the wall.

4.3.2 WALE model for LES

The wall adapting local-eddy viscosity model (WALE) proposed by Ducros & Nicoud [18] in 1998 is implemented in the flow solver FASTEST to extend the range of LES models. The WALE model offers significant improvements over the Smagorinsky model without a dynamic calculation procedure for the model constant. In contrast to the Smagorinsky model, the WALE model takes into account the local strain as well as the rotation rates to calculate the turbulent eddy viscosity. The model recovers a correct scaling of the eddy viscosity in the near wall region without the use of damping functions. Furthermore the eddy viscosity vanishes in laminar flow, thereby enabling the model to predict transitional flow regimes. The model calculates the sub-grid scale viscosity as

$$\nu_{SGS} = (C_w \Delta)^2 \frac{(S_{ij}^d S_{ij}^d)^{3/2}}{(\bar{S}_{ij}\bar{S}_{ij})^{5/2} + (S_{ij}^d S_{ij}^d)^{5/4}}, \tag{4.37}$$

where S_{ij}^d is the traceless symmetric part of a square of the velocity gradient tensor $\bar{g}_{ij} = \frac{\partial u_i}{\partial x_j}$, given by

$$S_{ij}^d = \frac{1}{2}(\bar{g}_{ij}^2 + \bar{g}_{ji}^2) - \frac{1}{3}\delta_{ij}\bar{g}_{kk}^2,$$

where C_w represents the WALE model constant and Δ represents the filter-width.

Even though there has been reported values of C_w in literature, it is always a good idea to calibrate the model constant in a new code as the model constant is influenced by the discretization practices employed in the code. Calibration of the WALE modal constant C_w is performed by simulating *decaying homogeneous isotropic turbulence* (DIT) to adjust the model constant against the energy spectrum from a DNS by Wray [124]. The geometry of the test case is a cube of normalized dimension 2π in each direction. Simulations are performed with two different grids containing 64^3 and 128^3 grid points, with periodicity in all three directions. The flow is initialized with a DNS data from [44]. Furthermore, the 2^{nd} order CDS is applied for spatial discretization and the 2^{nd} order BDF for temporal discretization.

Figure 4.4 shows the variation of C_w for the two grids. The effect of varying C_w appears to be stronger for the coarse grid, which is in accordance with the general properties of a LES as a course grid increases the influence of

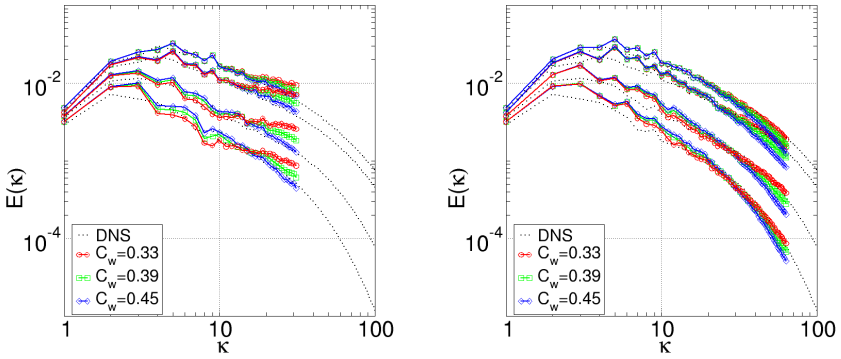

(a) (b)

Fig. 4.4: Energy spectra for DIT testcase with the WALE model for LES at $t = 0.2,\ 0.45,\ 1.45$ and 3.0 (a) variation of C_w for 64^3 grid (b) variation of C_w for 128^3 grid.

a sub-grid scale model. From figure 4.4a, a value of $C_w = 0.45$ seems to be appropriate, but a value of $C_w = 0.39$ is chosen in this study. The choice is made by comparing energy spectra for both grids and considering the fact that dense grids are more likely to be encountered for a LES, hence a value agreeing well with 128^3 grid is chosen.

4.3.3 Wall Distance Calculation

The normal wall distance d_w appears in equation (4.33). A calculation of the normal wall distance is necessary for some turbulence modeling approaches, e.g. the Spalart-Allmaras model [97], Menter's $k - \omega$ SST model [66] and the DDES model. Search procedures or a differential equation based method can be employed to estimate d_w, however search procedures could be very expensive in terms of the computational time. For a fluid-structure interaction scenario the distance would need to be evaluated many times in each time step for every iteration of the coupling algorithm.

A review of different differential equation based wall distance calculation methods has been reported in [114]. In this work, a Poisson equation based wall distance calculation, first proposed by Spalding [98] and reported by Tucker [114], is implemented in the flow solver FASTEST. A Poisson equation for the distance function ϕ is given as

$$\Delta\phi = -1, \tag{4.38}$$

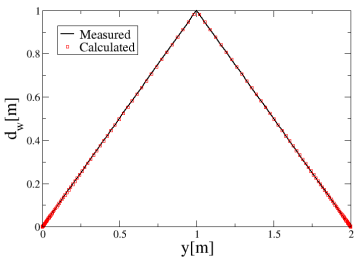

(a)

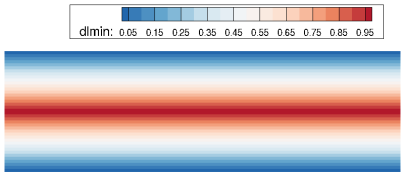

(b)

Fig. 4.5: d_w calculation for channel flow test case (a) comparison between measured and calculated values (b) contour plot of d_w.

with Dirichlet boundary condition at walls

$$\phi = 0,$$

and Neumann type boundary conditions at all other boundaries

$$\frac{\partial \phi}{\partial n} = 0. \tag{4.39}$$

The wall distance is calculated from a solution of the Poisson equation for the distance function ϕ as

$$d_w = \sqrt{\nabla\phi \cdot \nabla\phi + 2\phi} - \sqrt{\nabla\phi \cdot \nabla\phi}, \tag{4.40}$$

where "$\cdot$" represents a dot product between two vectors. The calculation of d_w assumes infinite coordinates in the non-normal wall direction, which implies that d_w would have better accuracies close to walls [114]. This effect is demonstrated by simulating two different test cases. However, the accuracy of the wall distance predictions is important for turbulence modeling only close to walls.

A calculation of the wall distance has been demonstrated for a channel flow test case in figure 4.5. Figure 4.5a shows a comparison between measured and computed values of d_w. The figure demonstrates a very accurate prediction, which is owing to the geometry of the channel i.e. the absence of any solid boundaries in the x-direction. Another calculation of the wall distance d_w is performed in a 2-d square, with all four sides of the square defined as wall. The purpose is to demonstrate the effect of multiple solid boundaries and corners on the calculation of d_w. The calculation of d_w in a square duct is shown in figure 4.6. A comparison between measured and calculated values of d_w at $x = 1$ shows a good agreement near the wall as can be seen in figure 4.6a, however away from walls the prediction is deteriorated. Figure

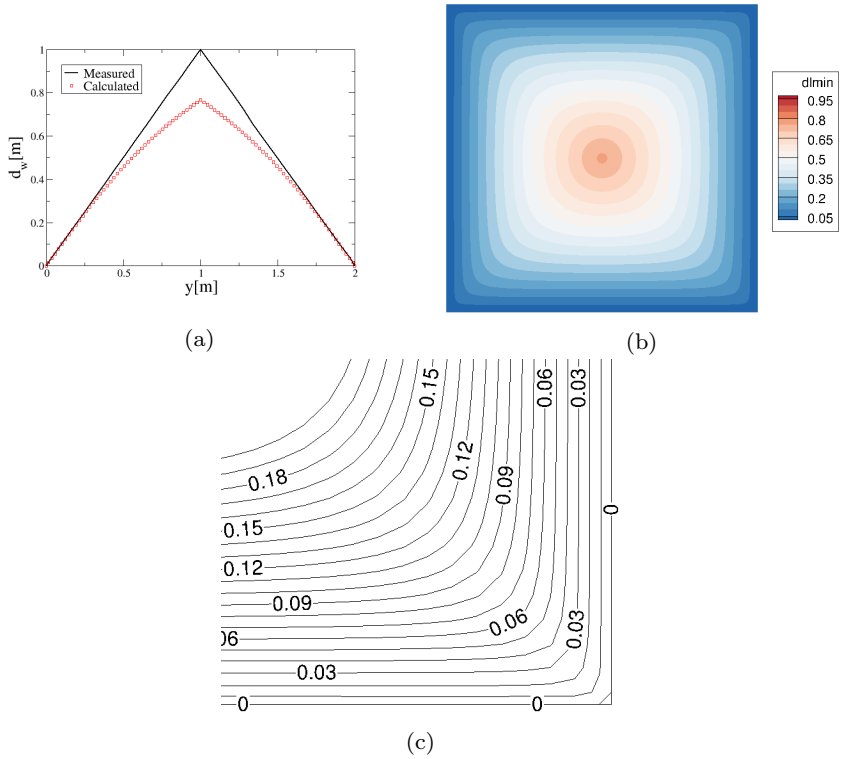

Fig. 4.6: d_w calculation for 2-d square test case (a) comparison between measured and calculated values at $x = 1$ (b) contour plot of d_w (c) isolines of d_w in bottom right corner of 2-d square.

4.6c shows isolines of d_w in a corner of the 2-d square, the shape of isolines becomes less sharp going away from the corner, which is also an indication of a decreasing accuracy away from walls.

4.3.4 Compound Wall Treatment (CWT)

The treatment of wall boundary conditions in a computation of the turbulent flow requires a grid with a wall y^+ value in a specific range, depending on the turbulence model. In the *integration to wall* (ITW) approach (also termed as *low-Re model*), the first grid node adjacent to the wall needs to be inside the viscous sublayer and the wall sheer stress τ_w can be evaluated from equation (4.5). Resolving the boundary layer up to the viscous sublayer requires a grid with wall $y^+ \approx 1$, resulting in dense grids and higher computational

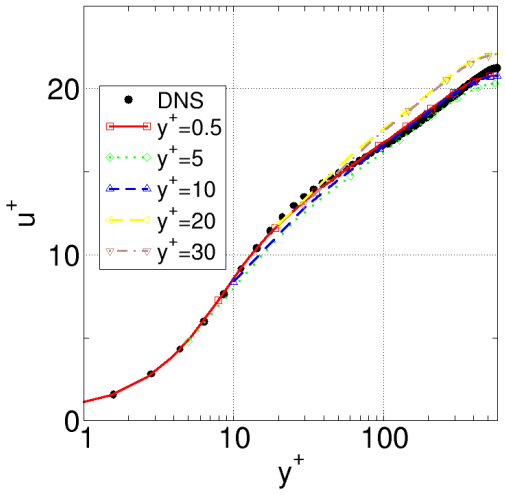

Fig. 4.7: Channel flow $Re_\tau = 590$: On different grids, with y^+ from 0.5 to 30, normalized velocity vs. normalized wall distance.

cost. However, in the *wall functions* (WF) approach (also termed as *high-Re model*), the wall shear stress is estimated by employing the log law (4.10), and first cell on the wall has a $y^+ > 30$.

Even when a finer grid for the ITW approach is computationally feasible, meeting a strict wall y^+ criteria in a complex geometry might not be possible. Instead, the first grid point might often lie in the buffer region ($5 < y^+ < 30$), making neither the ITW nor the WF approach applicable. This situation might also arise as a result of a systematic grid refinement/coarsening or in moving grids as encountered in a FSI scenario. The CWT approach proposed by Popovac and Hanjalić [81] automatically applies the ITW or the WF approach, depending upon the position of the first grid cell on the wall. When the first grid cell lies in the buffer region, appropriate wall boundary conditions are recovered by the use of exponential blending functions between viscous and fully turbulent expressions of boundary conditions. These exponential blending functions provided by Popovac are a generalization of expressions proposed by Kader [46] for the approximation of mean velocity and temperature profiles of a boundary layer. The CWT has been employed in this work in conjunction with the $k - \epsilon - \zeta - f$ model, while the approach can work with other turbulence models as well that permit an ITW approach.

The primary variables for which boundary conditions need to be modified by a blending approach are: the wall shear stress τ_w and its relation to the mean velocity, the production of turbulent kinetic energy $\mathcal{P}$ and its dissipation ϵ, and the elliptic function f. Following the expression used by Kader, a

blending between viscous and fully turbulent values of a general variable ϕ is defined as

$$\phi = \phi_\nu e^{-\Gamma} + \phi_t e^{-1/\Gamma}, \tag{4.41}$$

where ν denotes a viscous (i.e. wall limiting) and t denotes a fully turbulent value of the variable, and Γ is a function $y^+ = u_\tau y/\nu$ given as

$$\Gamma = \frac{0.01y^{+4}}{1 + 5y^+}. \tag{4.42}$$

The above expression can be used to blend normalized wall velocity expressions from the viscous sublayer (equation (4.9)) and the log-law (equation (4.10)) to generate a unified expression as

$$u^+ = y^+ e^{-\Gamma} + \frac{1}{\kappa} \ln(Ey^+) e^{-1/\Gamma}. \tag{4.43}$$

Blending expressions for the wall shear stress τ_w, the turbulent kinetic energy production $\mathcal{P}$ and the dissipation rate ϵ for the $k-\epsilon-\zeta-f$ model are given in [81]. The blending formulation described earlier can not be applied to the elliptic relaxation function f, as f changes sign from a negative value at the boundary to a positive value in the homogeneous region. However, an unchanged boundary condition for f still gives an acceptable approximate solution for f. The CWT implemented in the fluid solver FASTEST is tested for a channel flow test case with $Re_\tau = 590$. For this purpose, the channel flow is simulated on different grid densities with a varying wall y^+ value. The velocity profile obtained on different grids with a varying wall y^+ value is shown in figure 4.7.

Figure 4.8 shows a profile for the normalized turbulent kinetic energy (k^+) and its dissipation rate (ϵ^+), the wall normal velocity scale (ζ) and the elliptic relaxation function (f^+). The results show a good agreement with the DNS data, except for f^+ with coarse meshes, and some minor differences in the buffer region for k^+ and $\epsilon+$.

The wall function approach used here does not account for non-equilibrium effects (e.g. pressure gradients, separation and others). The CWT with wall functions that does not account for non-equilibrium effects would suffer inaccuracies in flows with boundary layer separation or pressure gradients. However, the non-equilibrium effects can be included in a wall function approach, as described in [81].

Application of CWT with LES

The compound wall treatment can also be applied for a LES simulation. However, a major difference between the application of CWT in a RANS turbulence modeling approach and a LES is the calculation of the wall friction velocity u_τ. It can be calculated by using equation (4.6) but in practical CFD

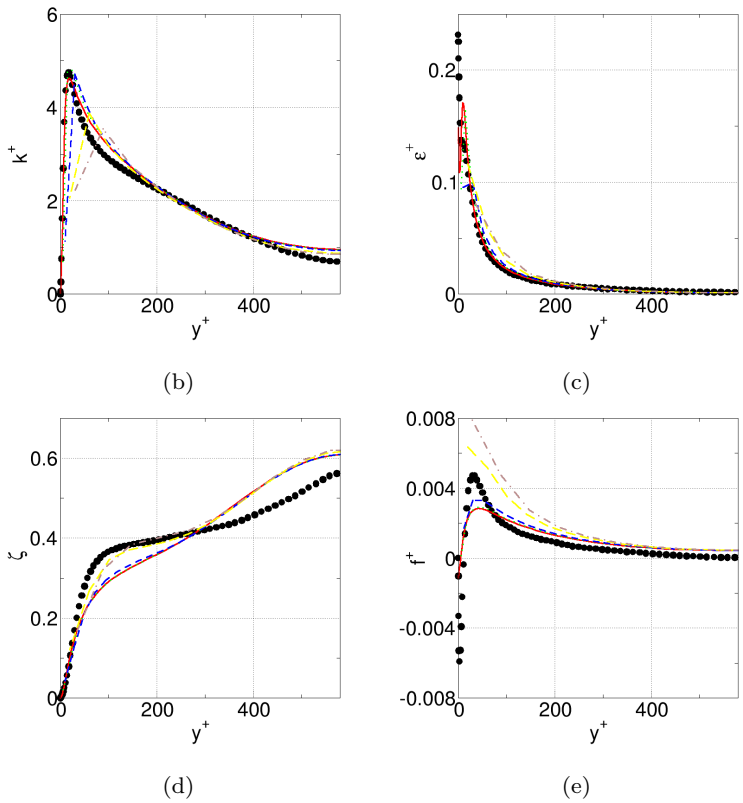

Fig. 4.8: Channel flow $Re_\tau = 590$: On different grids, with y^+ from 0.5 to 30,(a) turbulent kinetic energy k^+ (b) dissipation rate ϵ^+ (c) wall normal velocity scale ζ (d) elliptic relaxation function f^+. DNS data for $Re_\tau = 590$ from [69].

codes, to avoid singularity when u_τ tends to zero, the wall friction velocity is calculated as

$$u_k = C_\mu^{1/4} k^{1/2}, \tag{4.44}$$

where C_μ is a constant from the turbulence model and k is the turbulent kinetic energy. In a LES calculation, the turbulence kinetic energy k is not available directly. A solution is to employ an indirect approach for calculation of the wall friction velocity using the CWT expression (4.43). Since, equation (4.43) requires y^+ which again depends on u_τ, an iterative procedure can be employed to solve the equation for u_τ. The procedure has also been demonstrated in [45]. Newton's method can be used to iteratively solve for u_τ as

$$u_\tau^{n+1} = u_\tau^n - \frac{f(u_\tau)}{f'(u_\tau)}, \tag{4.45}$$

where the function $f(u_\tau)$ can be formed by rearranging CWT expression for u^+ as

$$f(u_\tau) = -\frac{u_{par}}{u_\tau} + y^+ e^{-\Gamma} + \frac{1}{\kappa}\ln(Ey^+)e^{-1/\Gamma},$$

and the derivative of $f(u_\tau)$ is given as

$$\begin{aligned} f'(u_\tau) =& \frac{u_{par}}{u_\tau^2} + Ae^{-\Gamma} + y^+\left(-\frac{4\Gamma}{u_\tau} + \frac{A\Gamma}{1+5y^+}\right)e^{-\Gamma} \\ &+ \frac{1}{u_\tau\kappa}e^{-1/\Gamma} + \frac{1}{k}\ln(Ey^+)\left(-\frac{5}{0.01u_\tau y^{+3}} + \frac{4}{u_\tau\Gamma}\right)e^{-1/\Gamma}, \end{aligned}$$

where $A = \frac{y}{\nu}$ with y representing the wall distance and u_{par} is the velocity parallel/tangential to the wall. The u_τ obtained in such a manner can be used to calculate the wall shear stress as $\tau_w = u_\tau^2\rho$, for application in the boundary condition for the velocity.

Chapter 5
Turbulent Flow and FSI test cases

This chapter provides a discussion on results of the turbulent and FSI simulations conducted in this work. The WALE model for LES is validated with the help of a 2-d periodic hill flow test case at a $Re = 10600$. The lid driven cavity flow with a flexible bottom wall is used to perform the coupling acceleration tests, in laminar and turbulent flow regimes. The compound wall treatment is tested for a FSI simulation of a benchmark test case. Further FSI simulations of three turbulent FSI test cases are studied with three different turbulence modeling approaches.

5.1 Periodic Hill Flow with WALE Model

The 2-d periodic hill flow test case is simulated to validate the implementation of the WALE model in the flow solver FASTEST. The results of the simulation are compared against a reference LES study conducted by Temmerman et al. [109]. A detailed analysis of the reference LES study is also

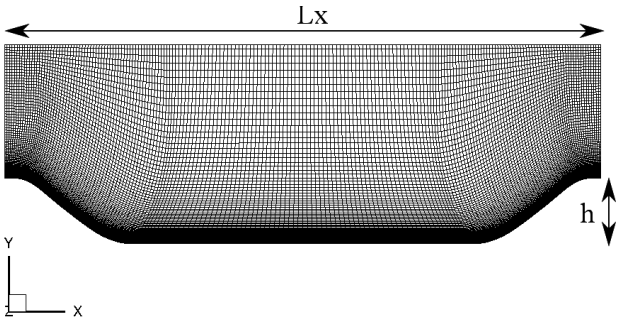

Fig. 5.1: Computational mesh of the 2-d hill test case

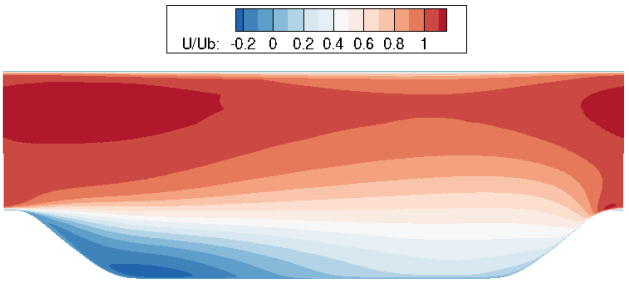

Fig. 5.2: Averaged streamwise velocity in 2-d hill flow

provided by Frölich et al. [24]. The results from the reference LES conducted in [24] have also agreed well with experiments in [8]. The test case has been widely used as a standard benchmark for validation of turbulence modeling approaches. It is well suited to access the capabilities of turbulence resolving approaches like LES and hybrid RANS-LES, since it constitutes various physical flow features like separation, reattachment and depending upon the Reynolds number, turbulent transition and relaminarization. The accurate predictions of separation and reattachment locations in the channel is a challenging task as the locations are not clearly determinable by the geometry. For such a flow scenario, RANS modeling approaches are known to perform inadequately, as some calculations reported in [115] show.

The computational domain consists of a channel with a length $L_x = 9h$ and a height $L_y = 3.035h$, whereas in spanwise direction the domain has a size of $L_z = 4.5h$, with h being the hill height. Figure 5.1 shows the computational mesh used for this study. The flow Reynolds number based on the bulk inflow velocity U_b and the hill height h is $R_e = 10600$. The flow boundaries normal to the streamwise and spanwise directions are treated with periodic boundary conditions, while a no-slip boundary condition is applied at the upper and lower walls of the domain. The mesh consists of $192 \times 96 \times 128$ control volumes in x, y and z directions, respectively. It is designed to have the first cell $y^+ < 1$ on the lower wall, while on the upper wall the first cell height is designed to have a $y^+ \approx 15$. The compound wall treatment is employed on the top wall of the computational domain. In the spanwise direction, the mesh spacing in wall normal units is $\Delta z^+ < 25$, while in the streamwise direction $\Delta x^+ \approx 20 - 40$, with higher grid densities on and around the hill slopes. The grid stretching ratio near the lower wall is 1.05 in the wall normal direction, while in the streamwise direction a stretching ratio of 1.1 is used. The mesh is considerably coarser than the one used in the reference LES study [109], but still fulfills requirements described in [77]. A dimensionless time-step size of $\Delta t U_b/h = 5.98 \times 10^{-3}$ is chosen to have $CFL \approx 1$.

For spatial discretization, the 2^{nd} order central differencing scheme is applied and the 2^{nd} order implicit backward differencing scheme is used for time

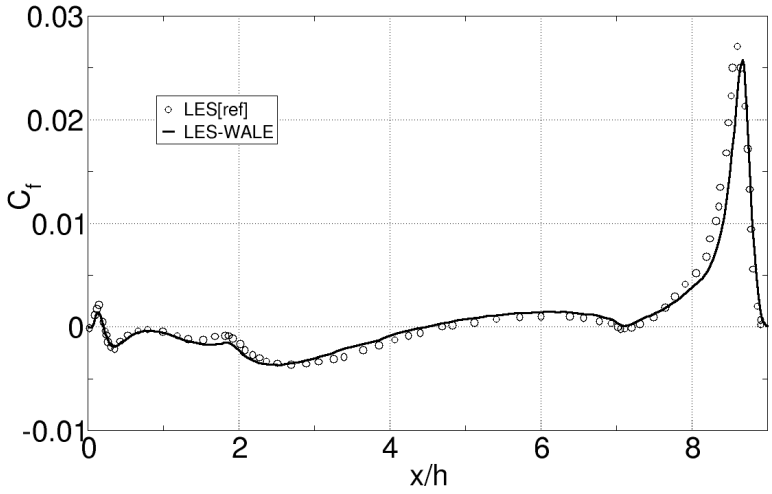

Fig. 5.3: Skin friction coefficient along lower wall of the 2-d hill channel

discretization. The simulation is performed for 23 flow through cycles to allow the flow to develop in the channel. After the initial 23 flow through times, the averaging is turned on for the next 55 flow through times, as suggested in [24]. The flow averaging is also performed in the spanwise direction. Figure 5.2 shows contours of the averaged streamwise velocity.

	LES[109]	LES-WALE
x_s/h	0.22	0.22
x_r/h	4.72	4.47

Table 5.1: Separation and re-attachment points for 2-d hill flow

Figure 5.3 show a plot of the skin friction coefficient ($C_f = \frac{\tau_w}{0.5\rho U_b^2}$) at the lower wall with C_f from the reference LES study. The prediction of the skin friction coefficient agree very well with prediction from the reference. Table 5.1 draws a comparison between separation and reattachment locations predicted by the current simulation and the reference LES study. Both locations are predicted with a reasonable accuracy. The reattachment location is under-predicted by 5.5% compared to the reference LES study.

Figure 5.4 shows the velocity profile at different locations along the channel length. A very good agreement with the reference velocity profiles can be observed, apart from minor differences near the upper wall where the grid is coarse and the CWT is applied.

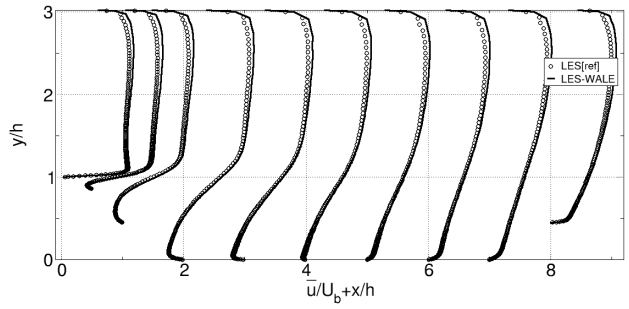

(a)

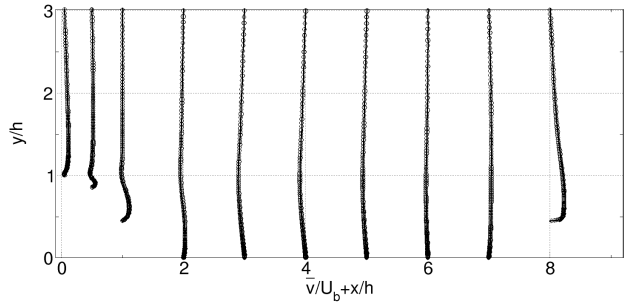

(b)

Fig. 5.4: Averaged velocity profile for 2-d hill at different locations along channel length, with reference LES data from [109] (a) Comparison of averaged u-velocity profile (b) Comparison of averaged v-velocity profile

The averaged Reynolds stresses are compared with the reference LES data in figure 5.5. In general, a good agreement with the reference LES profiles can be observed, apart from minor differences near the separation location. Overall agreement with the reference LES for separation and reattachment locations, and velocity profiles is satisfactory, specially considering the resolution of the mesh. Also the agreement of velocity profiles with the reference data close to the upper wall demonstrates a correct application of the compound wall treatment in an LES flow simulation.

5.2 Coupling acceleration tests

The coupling acceleration tests have been performed employing the lid driven cavity with a flexible bottom wall as a test case. A 2-d study of the test case has been conducted by Küttler and Wall [52] and Kassiotis et al. [48], while

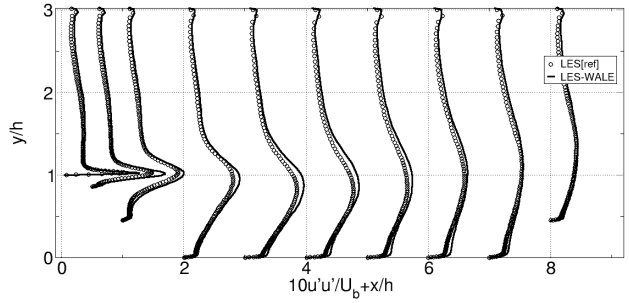

(a)

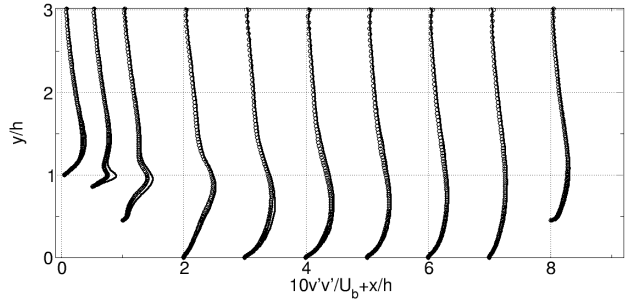

(b)

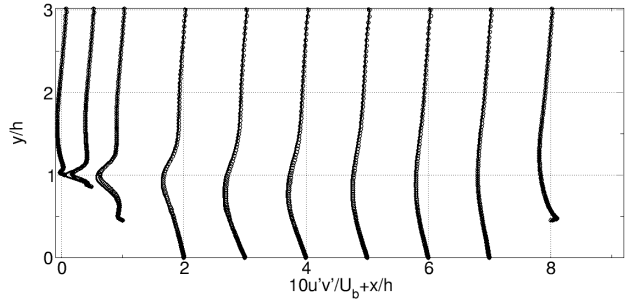

(c)

Fig. 5.5: Averaged Reynolds stress for 2-d hill at different locations along channel length, with reference LES data from [109] (a) $u'u'$ (b) $v'v'$ (c) $u'v'$

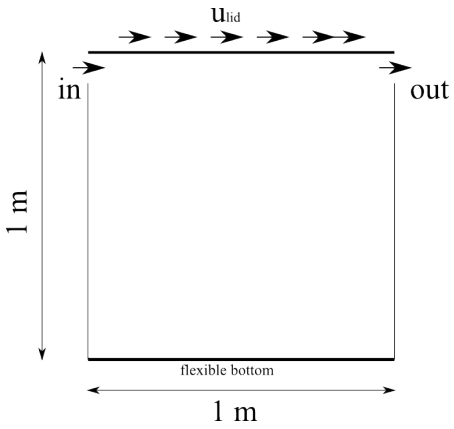

Fig. 5.6: Lid driven cavity with flexible bottom configuration

3-d studies have been performed by Sternel et al. [102] and Heck et al. [33]. The setup consists of a driven cavity flow with a flexible bottom wall, while the top wall moves with a prescribed oscillating velocity, as shown in figure 5.6. The velocity of the top wall is defined as a function of time t, given as

$$u_{lid} = u_0 - u_{osc} \cos \frac{2\pi t}{T_0}, \tag{5.1}$$

where T_0 is the time period of the oscillating velocity u_{osc}. The velocity at the inlet is equal to the oscillating velocity of the moving lid. The test case is

Fluid	Laminar	Turbulent
u_0 [m/s]	1	150
u_{osc} [m/s]	1	30
T_0 [s]	5	1/5
ν_f [m^2/s]	0.01	0.01
ρ_f [kg/m^3]	1	1
Structure	Laminar	Turbulent
E [N/m^2]	2500	250000
Poisson ratio ν_s	0.0	0.0
Thickness [m]	0.002	0.1254
ρ_s [kg/m^3]	1000	500

Table 5.2: Parameters for turbulent and laminar lid driven cavity with a flexible bottom

studied in laminar and turbulent flow regimes. Fluid and structural properties of both configurations are described in table 5.2. The coupling between

the fluid and the structural solver for coupling acceleration tests is performed with the open-source multi-physics coupling tool preCICE [9]. The coupling acceleration techniques studied are built into preCICE. Apart from the built-in coupling acceleration and different coupling strategies, preCICE also offers the capability to couple more than two codes. This could be useful for performing multi-physics simulations with more than two physical phenomena that require separate simulation environments.

Laminar Driven Cavity FSI

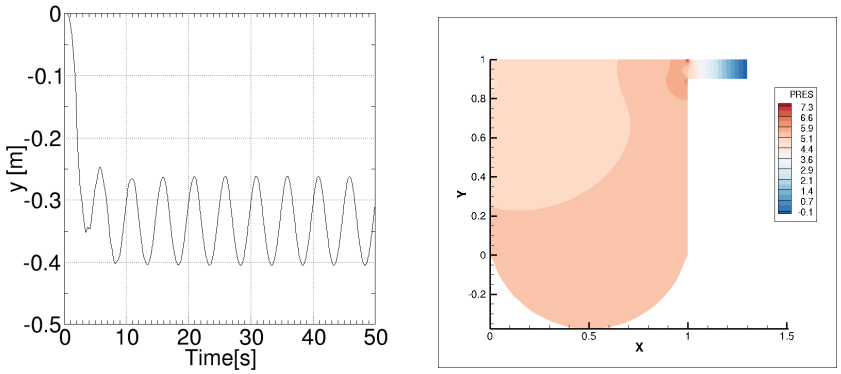

(a) (b)

Fig. 5.7: Laminar driven cavity flow with a flexible bottom wall (a) y-displacement of midpoint of the flexible bottom wall (b) contours of pressure at $t = 32.5$s

The FSI tests with a laminar flow in the driven cavity are performed with the fixed under-relaxation and the dynamic under-relaxation methods Aitken and IQN-ILS. The flow Reynolds number based on the oscillating lid velocity and cavity length varies between 0 and 200. The mesh used for this study consists of 40×46 control volumes in x and y direction for the flow solver, while for the structural solver a mesh of 32×1 8-node brick elements with enhanced strain formulation is employed. Both the fluid and the structural solver use a second order accurate time discretization scheme. A time step size of $\Delta t = 0.05$s is used for all simulations. The fluid solver employs a first order upwind scheme for discretization of the convective fluxes. Figure 5.7 shows the y-displacement of midpoint of the flexible bottom wall and pressure contours at $t = 32.5$s.

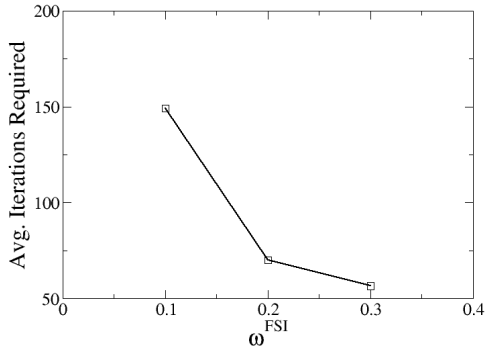

Fig. 5.8: Laminar driven cavity with a flexible bottom wall: average iterations required for convergence per time-step with a variation of the under-relaxation parameter ω^{FSI}

Figure 5.8 shows the average number of coupling iterations required for convergence per time-step with a variation of the fixed under-relaxation parameter ω_{FSI}. A convergence criterion of $\epsilon_{FSI} < 1 \times 10^{-9}$ is used for displacements of the bottom wall. The lowest number of required iterations are for $\omega^{FSI} = 0.3$, while increasing the under-relaxation further resulted in divergence of the coupling algorithm. The structural material for the laminar driven cavity is very flexible and the main source of resistance to the fluid pressure is the mass of the structure [52], therefore the structure oscillates close to the time period T_0 of the oscillating lid velocity. The average number of iterations required per time step for each method are shown in table 5.3. The IQN-ILS(4) method which reuses information from four previous time-steps can be observed to perform better than all other methods tested. The dynamic under-relaxation methods show a significant performance gain over the fixed under-relaxation technique.

Acceleration method	$\omega^{FSI} = 0.3$	Aitken	IQN-ILS(2)	IQN-ILS(4)
Avg. iterations required	56.6	14.7	16.5	11.9

Table 5.3: Average iterations required for convergence per time-step for different coupling acceleration methods with a laminar driven cavity flow

Turbulent Driven Cavity FSI

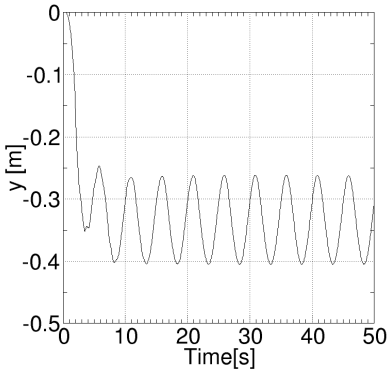

(a)

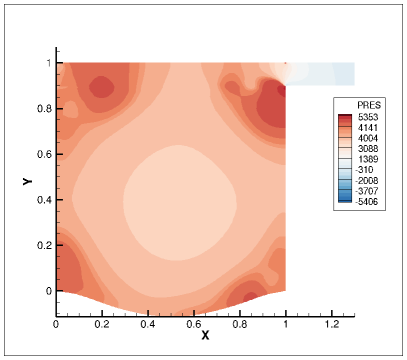

(b)

Fig. 5.9: Turbulent driven cavity flow with a flexible bottom wall (a) y-displacement of midpoint of the flexible bottom wall (b) contours of pressure at $t = 0.6$s

For the turbulent flow in driven cavity the Reynolds number varies between 1200 and 1800 based on the oscillating lid velocity and the cavity length. The material chosen for these tests is more stiff than the laminar driven cavity, to limit the structural deflections. The thickness of the structure and the material are chosen to have a natural frequency close to the oscillation frequency of the lid velocity. The y-displacement of midpoint of the flexible bottom and contours of pressure at $t = 0.6$s are shown in figure 5.9.

The fluid mesh for the problem consists of 208×76 control volumes in x and y direction. The first order upwind scheme is used for discretization of convective fluxes in the fluid solver. The $k - \epsilon - \zeta - f$ model is used to simulated turbulence in the flow. The structural mesh consists of 32×1 8-node brick elements with enhanced strain formulation. A time-step size of $\Delta t = 0.0003$s is employed with second order accurate time discretizations applied for both solver. A convergence criterion of $\epsilon_{FSI} < 1 \times 10^{-9}$ is used for displacements at the FSI interface.

Figure 5.10 shows the average number coupling iterations required for convergence per time-step with a variation of the under-relaxation parameter ω^{FSI}. The stiffness of the structure allows for higher values of the under-relaxation, compared to the laminar case. From figure 5.10 a minimum number of iterations required is for $\omega_{FSI} = 0.9$, while increasing the value further results in an increase in the number of iterations required for convergence. The average number of coupling iterations required for different acceleration

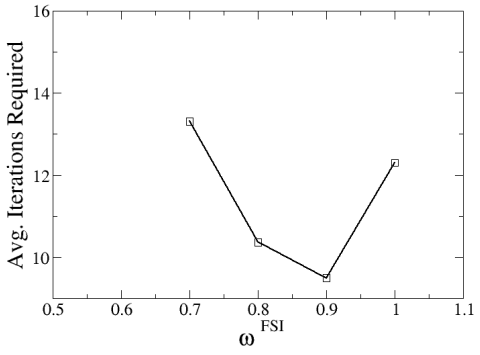

Fig. 5.10: Turbulent driven cavity with a flexible bottom wall: average iterations required for convergence per time-step with a variation of the under-relaxation parameter ω^{FSI}

techniques is shown in table 5.4. IQN-ILS requires the minimum number of average coupling iterations, where IQN-ILS(2) with two reused time-steps performs the same as IQN-ILS(4). The gain in performance with dynamic under-relaxation techniques is very little, contrary to the laminar driven cavity case.

Acceleration method	$\omega^{FSI} = 0.9$	Aitken	IQN-ILS(2)	IQN-ILS(4)
Avg. iterations required	9.5	8.2	7.1	7.1

Table 5.4: Average iterations required for convergence per time-step for different coupling acceleration methods with a turbulent driven cavity flow.

5.3 Description of FSI test cases

Three different turbulent FSI test cases are studied in this work. A description of these test cases along with the material and geometric details is provided in the following.

TL1

The TL1 test case has been proposed by Gomes and Lienhart [30]. The test case consists of a thin flexible stainless steel sheet attached to a revolvable cylinder with a rectangular mass attached to the other end of the sheet as shown in figure 5.11. Table 5.5 gives densities of materials and the modulus

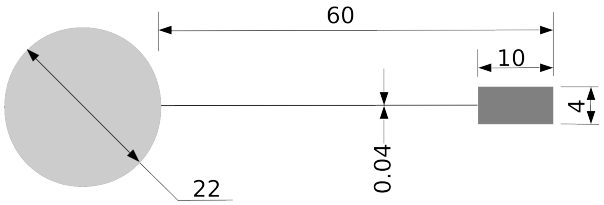

Fig. 5.11: TL1: Structural model dimensions in mm.

of elasticity of the flexible structure.

Cylinder density	$\rho_{cylinder} = 2828$ kg/m^3
Flexible sheet density	$\rho_{flexible\ sheet} = 7855$ kg/m^3
End mass density	$\rho_{end\ mass} = 7800$ kg/m^3
Young's modulus of flexible sheet	$E_{flexible\ sheet} = 2 \times 10^{11}$ N/m^2

Table 5.5: TL1: Material properties of the structure.

The structure is placed inside a vertical tunnel with a test section cross-sectional area of 180×240 mm^2 and a length of 338 mm. The fluid inside the test section is water at $25°C$, with a kinematic fluid viscosity $\nu_{fluid} = 0.97 \times 10^{-6}$ m^2/s and a density of $\rho_{fluid} = 998$ kg/m^3. The bulk fluid velocity measured in experiments at the inlet is $u_\infty = 0.68$ m/s. The flow Reynolds number based on the bulk fluid velocity and the cylinder diameter is $Re = 15400$. The cylinder flow is considered to be in sub-critical regime. This flow configuration is considered challenging for turbulence models, since the boundary layer is laminar and the transition to turbulence occurs in separated shear layers and the wake. The structure rotates and the thin flexible sheet deflects in the first bending mode. The instability mechanism is characterized as the Instability Induced Excitation (IIE)[71], and the structure oscillates in the first mode. The time phase-averaged displacement of the end mass and the rotation angle of the revolvable cylinder against the phase angle are provided from the experimental observations for the purpose of validation.

FSI-PfS-1a

The FSI-PfS-1a test case has been proposed by De Nayer et al. [73]. The test case offers a simpler geometry than the TL1 test case, consisting of a circular cylinder with a flexible rubber sheet attached to it, as shown in figure 5.12. Unlike the TL1 test case, the cylinder is not allowed to rotate

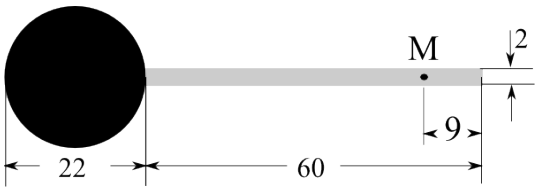

Fig. 5.12: FSI-PfS-1a: Structural model dimensions in mm.

and there is no end mass attached to the end of the flexible structure. The FSI excitation process is similar to the TL1 case, where the structure bends in the 1st mode close to its natural frequency. Apart from a simple geometry, another advantage is the availability of a parametric study on the influence of material and geometric properties of the structure in FSI simulations. Table 5.6 details the properties of the fluid and the structure. The structure is placed

Structure	
Density	$\rho_{rubber\ plate} = 1360$ kg/m^3
Young's Modulus	$E_{rubber\ plate} = 16 \times 10^6$ N/m^2
Fluid	
Inflow velocity	$u_{inflow} = 1.385$ m/s
Density	$\rho_f = 1000$ kg/m^3
Dynamic viscosity	$\mu_f = 1.0 \times 10^{-3}$ N.s/m^2

Table 5.6: TL1: Material properties of the structure.

inside a wind-tunnel test section, where the flexible rubber plate oscillates under the influence of flow disturbances caused by the cylinder in front. The flow Reynolds number $Re = 30470$ is higher than in the TL1 setup, but still in the sub-critical flow regime for a cylinder. The averaged deflections of a monitoring point M on the structure (as shown in figure 5.12), the averaged oscillation frequency and the velocity field around the oscillating structure are available from the experiments for validation purposes.

FSI-PfS-2a

The test case has been proposed by Kalmbach and Breuer [47] as a complement of the FSI-PfS-1a by providing a different excitation mechanism of the FSI phenomenon. The structural geometry and the flow properties are similar to the FSI-PfS-1a, except that the rubber plate is less stiff with a Young's modulus of $E_{rubber\,plate} = 4.1 \times 10^6 \mathrm{N/m^2}$ and a steel end mass is attached at the end of the rubber plate to limit the structural deflection in 2-d. The geometry of the structure and dimensions are shown in figure 5.13. A more

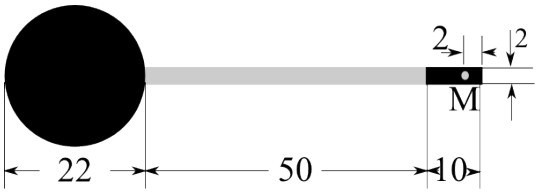

Fig. 5.13: FSI-PfS-2a: Structural model dimensions in mm.

flexible rubber material with the same flow configuration as in FSI-PfS-1a, gives rise to a different excitation phenomenon. It is termed as the Movement Induced Excitation (MIE), where forces on an accelerating body in a fluid are modified by the unsteady flow induced due to the movement of the body [71]. The data for comparison is provided for a monitoring point M on the structure, shown in figure 5.13. The averaged characteristics of oscillation and the phase-averaged velocity fields from the experiment are provided for comparison.

5.4 CWT tests with FSI

In a turbulent fluid simulation with a moving grid, ensuring a desired wall y^+ value[1] (equation 4.7) might not be possible. A grid not satisfying the wall y^+ criterion according to the turbulence modeling approach would deteriorate the predictions of the near wall turbulent behavior (i.e. law of the wall, equations 4.9 and 4.10). Incorrect predictions of the wall behavior would lead to a wrong estimation of the shear stress at the wall which can introduce an error in predicted structural deflections. The application of the compound wall treatment (CWT) [81] on stationary grids is demonstrated in chapter 4, by simulating a channel flow on grids with varying wall y^+ values. The

[1] Ensuring a specific wall y^+ value would require fixed distance of the first cell center control volume on the wall

purpose here is to demonstrate an advantage in a situation where the CWT could be useful in a moving grid scenario.

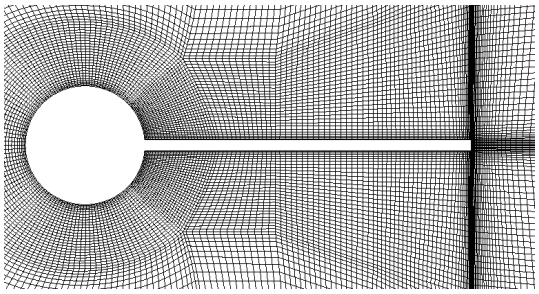

Fig. 5.14: Grid for FSI-PfS-1a with wall $y^+ \approx 15$.

The CWT is tested in a FSI scenario by studying 2-d FSI-PfS-1a simulations. To demonstrate the advantage of CWT in moving grid scenarios, a grid with a wall $y^+ \approx 15$ is designed [2], having a total of 39352 control volumes. The FSI simulations are conducted with the $k-\epsilon-\zeta-f$ model, with and without the application of CWT. A snapshot of the grid around the structure is shown in figure 5.14. The structural code FEAP employs the linear 8-node brick elements with enhanced strain formulation and the Newmark method for time discretization. The grid used for the structure has 32×1 elements. The fluid solver FASTEST employs a blending between the UDS and the CDS for convective fluxes with a blending factor of 0.5, and the second order implicit backward differencing scheme for time discretization. A time step size of $\Delta t = 7 \times 10^{-5}$s is chosen.

Figure 5.15 shows the averaged y-displacement of the monitoring point on the structure. The results are time phase-averaged as explained in [73], with averaging performed for 23 oscillation cycles of the structure for both simulations. Table 5.7 shows a comparison between the maximum and the

	$\overline{f_{FSI}}$[hz]	$Err.\%$	$\overline{U_y^*\|_{max}}$	$Err.\%$	$\overline{U_y^*\|_{min}}$	$Err.\%$
Exp. [73]	7.10	-	0.418	-	-0.420	-
CWT	7.15	0.7	0.383	-8.4	-0.381	-9.3
w/o CWT	7.33	3.2	0.358	-14.4	-0.347	-17.4

Table 5.7: FSI-PfS-1a: Comparison of the y-displacement and the oscillation frequency with and without the application of CWT.

[2] The grid is prepared by modifying the grid used by Prof. Breuer's group for their LES studies on FSI-PfS-1a [73] and FSI-PfS-2a [72]. The grid used here has the same block structure.

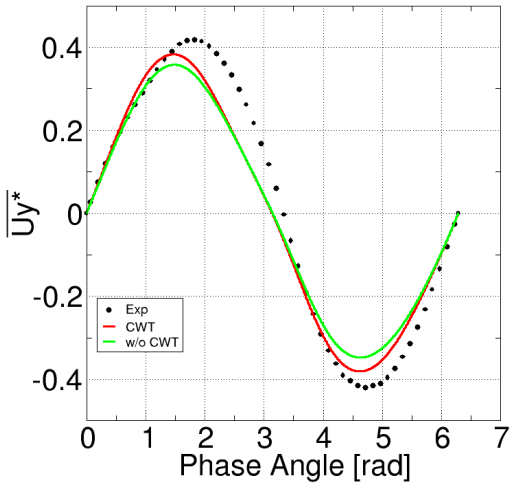

Fig. 5.15: FSI-PfS-1a: Averaged y-displacement for two FSI simulations with and without the CWT application (Exp. from [73]).

minimum y-displacement of the monitoring point, the oscillation frequency and the corresponding percentage differences with the experimental data. The application of CWT improves the accuracy of predictions for the oscillation frequency and the averaged maximum and minimum y-displacement of the structural deflection. A slight asymmetry in the prediction of y-displacement can also be observed for both simulations. However, results from the simulation without the application of CWT show more asymmetry. This asymmetry is expected to reduce if averaging is performed for more oscillation cycles, but the averaged maximum and minimum y-displacement would still be under-predicted compared to the simulation with CWT.

5.5 Simulation of the FSI test cases

The FSI test cases that has already been discussed in a previous section, are simulated with a RANS and scale-resolving simulation models. A comparison between a linear and a higher order element in the structural solver is also performed with two simulations of the FSI-PfS-1a test case. The two test cases, FSI-PfS-1a and FSI-PfS-2a are studied in 2-d and 3-d RANS simulation setups with the $k-\epsilon-\zeta-f$ turbulence model. Both test cases are also simulated with the $k-\epsilon-\zeta-f$ based DDES model. The TL1 test case is

studied in the DDES fluid simulation as well as an LES with the dynamic Smagorinsky model.

5.5.1 Comparison between linear and higher order Elements in FEAP

The effect of employing higher order elements in a FSI simulation is studied with two simulations of FSI-PfS-1a with a higher order 20-node node brick element and a 8-node linear element for the structural subproblem. The 8-node linear brick elements a in FEM analysis are known to cause the shear locking [82] phenomena. The locking phenomena causes the material to behave more stiff than the actual stiffness of the material. For 8-node brick elements, the enhanced strain formulation in the structural code FEAP is employed to prevent the shear locking.

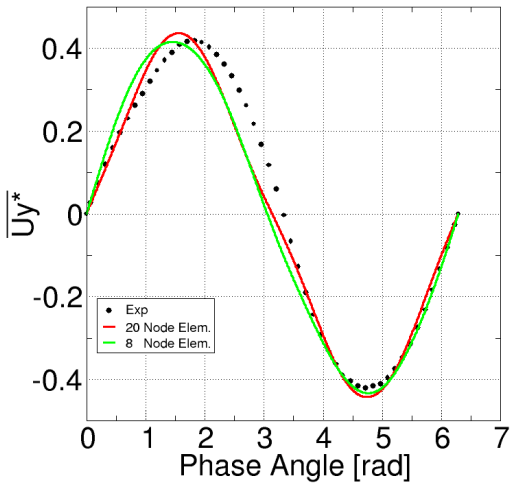

Fig. 5.16: FSI-PfS-1a: Averaged y-displacement for two FSI simulations with the 8-node linear and the 20-node higher order element (Exp. from [73]).

The fluid domain for two simulations is discretized with a coarse grid containing 19676 control volumes, and a blending between UDS and CDS with a blending factor of 0.5 is used for convective fluxes. The fluid solver employs the 2^{nd} order implicit backward differencing scheme for time discretization. The structure for both simulations is discretized with 32×1 elements. The 2^{nd} order implicit Newmark method is used for time discretization in FEAP.

From figure 5.16 a good agreement for the averaged y-displacements of the structural deflection can be observed for two simulations.

	$\overline{f_{FSI}}$[hz]	$Err.\%$	$\overline{U_y^*\|_{max}}$	$Err.\%$	$\overline{U_y^*\|_{min}}$	$Err.\%$
Exp. [73]	7.10	-	0.418	-	-0.420	-
8-node Elem.	7.57	6.6	0.437	4.5	-0.442	5.2
20-node Elem.	7.42	4.5	0.436	4.3	-0.435	3.6

Table 5.8: FSI-PfS-1a: Comparison of the y-displacement and the oscillation frequency with the 8-node linear and the 20-node higher order element.

Table 5.8 shows the maximum and minimum averaged y-displacements and the oscillation frequencies with the corresponding errors. The two elements produce very similar structural deflection and the oscillation frequencies. The advantage of the 20-node element in comparison to the 8-node element with enhanced strain formulation is not very clear. However, in the FSI context both simulations showed different convergence characteristics. The FSI simulation with 20-node elements required approximately 50% more iterations to converge on average than with the 8-node brick elements.

5.5.2 FSI tests with URANS

Even though the advancements in computing technology has been tremendous in the last two decades, but still the fluid simulations with an LES model or a DNS of turbulence might not be feasible in a near future for practical applications. The use of hybrid RANS-LES technique and the wall modeled LES technique is going to become more frequent. The performance of these hybrid methods is influenced by accuracy of the underlying RANS model. For these reasons, the application of RANS turbulence modeling approach for flows with practical relevance is going to remain significant for a foreseeable future.

The two test cases FSI-PfS-1a and FSI-PfS-2a are simulated with 2-d and 3-d URANS simulation, employing the $k-\epsilon-\zeta-f$ turbulence model. The following sections provide a discussion on results of these simulations.

FSI-PfS-1a: URANS computations

The mesh employed for the two simulations, i.e. 2-d and 3-d URANS is similar in the x-y plane. The mesh contains 54676 control volumes in the x-y plane for 2-d URANS. Figure 5.17 shows a snapshot of the mesh in x-y plane. The mesh extends $3.5D$ from the center of the cylinder to the inlet of the

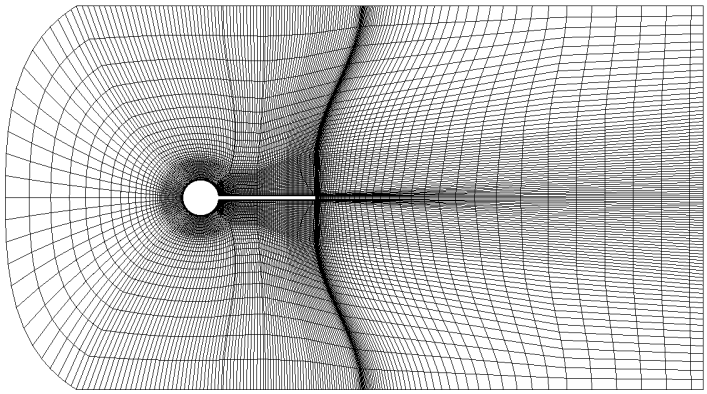

Fig. 5.17: 2-d and 3-d URANS mesh for FSI-PfS-1a in the x-y plane, every 2^{nd} grid line is visible.

computational domain, where D represents the cylinder diameter. In the downstream direction, the mesh extends approximately $14D$ from the center of the cylinder to the outlet of the domain. The 3-d mesh extends equal to the length of the rubber plate in spanwise direction with 32 equidistant control volumes and having a total of 32×54676 control volumes in the mesh. The multi-block structured mesh contains 30 blocks, and is created by modifying the mesh used in [73].

For the discretization of convective fluxes, the fluid solver FASTEST employs the UDS and the GAMMA scheme [43], for the 2-d and the 3-d URANS, respectively. The second order implicit backward differencing scheme is used for time discretization. A time step size of $\Delta t = 7 \times 10^{-5}$s is used, resulting in a CFL number between 1.5 and 3.0. However an inspection of the CFL in the whole domain revealed that around the cylinder and in separated shear layers the CFL remains below unity. The upper and lower boundaries in the simulation are treated as slip walls, to avoid unnecessary refinement of the mesh near these boundaries. In 3-d simulation, the two side planes are also treated with a symmetry boundary condition. While the cylinder and the rubber plate are treated with a no-slip wall boundary condition. The inlet of the computational domain is specified with a fixed velocity, while the outlet is treated with a zero gradient boundary condition.

For the structural subproblem, the structural solver FEAP employs 30×1 8-node linear brick elements with enhanced strain formulation. The second order implicit Newmark method is used for time discretization. The structural material is modeled utilizing the Saint Venant-Kirchoff law. The rubber plate is fixed at one end, while displacements in spanwise direction are constrained to limit the deflection in the x-y plane only.

The implicit coupling algorithm, to solve the FSI problem has been described in section 3.3.1. The data exchange and interpolation between the

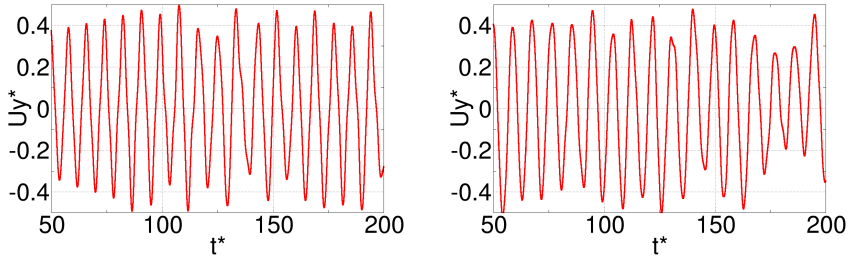

Fig. 5.18: FSI-PfS-1a: Dimensionless y-displacement of the structural deflection vs. dimensionless time (a) 2-d URANS (b) 3-d URANS.

structural and the flow solver is handled with the coupling code MpCCI. A fixed under-relaxation of structural displacements with a factor of $\omega^{FSI} = 0.3$ is used to insure stability of the coupling iterations. For acceleration of the coupling algorithm a 0^{th} order force extrapolation is employed. The coupling algorithm required approximately 12 iterations to meet a convergence criterion of $\epsilon_{FSI} < 1 \times 10^{-9}$ for both simulations. Simulations are initialized with structure initially at rest in a undeformed state. As the flow develops, the rubber plate starts to oscillate under the influence of alternating loads produced by the vortex shedding from the cylinder. The amplitude of deflection increases with every cycle and a quasi periodic state of oscillations is reached.

	Variation of					
	$U_y^*\|_{max}$		$U_y^*\|_{min}$		f_{FSI}[hz]	
	max.	*min.*	*max.*	*min.*	*max.*	*min.*
2-d URANS	0.499	0.347	-0.316	-0.493	7.97	6.50
3-d URANS	0.476	0.266	-0.195	-0.518	7.61	6.43

Table 5.9: FSI-PfS-1a: Variation of maxima and minima of dimensionless y-displacement from 2-d URANS and 3-d URANS.

Figure 5.18 shows the dimensionless y-displacement $U_y^* = U_y/D$ of a point $9mm$ from the free end of the plate against the dimensionless time $t^* = tu_{inflow}/D$. A quasi periodic behavior of the structural deflections can be observed. Table 5.9 shows the variation of maxima and minima of U_y^* and f_{FSI} from individual oscillation cycles. The maxima of U_y^* are observed to vary between 0.499 and 0.347 for the 2-d simulation and 0.476 and 0.266 for the 3-d simulation. The minima of U_y^* also show a variation of a similar magnitude between -0.316 and -0.493 for the 2-d simulation and between -0.195 and -0.518 for the 3-d simulation. The standard deviations of the displacement signal for the 3-d simulation (± 0.09) is significantly higher than

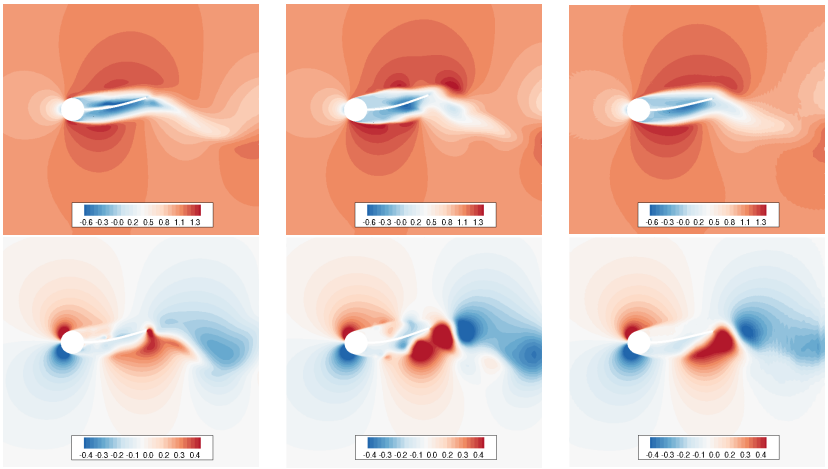

(a) (b) (c)

Fig. 5.19: FSI-PfS-1a: Comparison between (a) 2-d URANS, (b) 3-d URANS and (c) LES [73], for normalized u (top row) and v (bottom row) velocity at time $t = T_{FSI}/4$.

the experimental standard deviation (± 0.05), while for the 2-d simulation the standard deviation (± 0.06) of the signal shows a better agreement with the experimental result. The frequency of oscillation f_{FSI} shows a similar trend, where for the 2-d simulation the oscillation frequency varied between 7.97 and 6.50, and for the 3-d simulation a variation between 7.61 and 6.43 is observed. Both simulations are averaged for 23 cycles of the oscillation, after the oscillation behavior exhibits a quasi periodic state.

The flow field for FSI-PfS-1a is also compared with the phase-averaged LES flow field, that complements the experimental data available in [73], where the two flow fields show a good agreement. The phase-averaging process, as explained in [73], is necessary to have a comparison between highly chaotic turbulent flow from the experiment and the LES simulation. However, for a URANS simulation the flow field does not exhibit an instantaneous turbulent character and a comparison with phase-averaged LES data is performed without phase-averaging for two URANS simulations. Only the 3-d URANS simulation is averaged in spanwise direction. The comparison is performed for four critical phases in the oscillation cycle, which also visualizes the coupling process between structural and fluid motions that results in a periodic oscillation behavior of the structure. Figure 5.19 shows a comparison of the two simulations with the phase-averaged LES flow field for $t = T_{FSI}/4$. At this phase of the oscillation, the structure has reached its maximum deflection in the upward direction. Similarities between main flow features, such as the length of shear layers, recirculation regions near the plate surface and the

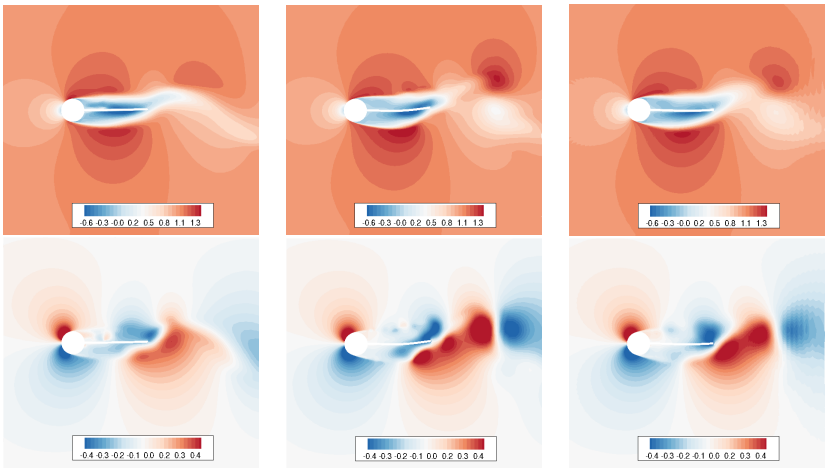

(a) (b) (c)

Fig. 5.20: FSI-PfS-1a: Comparison between (a) 2-d URANS, (b) 3-d URANS and (c) LES [73], for normalized u (top row) and v (bottom row) velocity at time $t = T_{FSI}/2$.

flow structures in the wake, are easily recognizable. For 2-d URANS the low and high velocity regions can be seen to be weaker, specially for v-velocity.

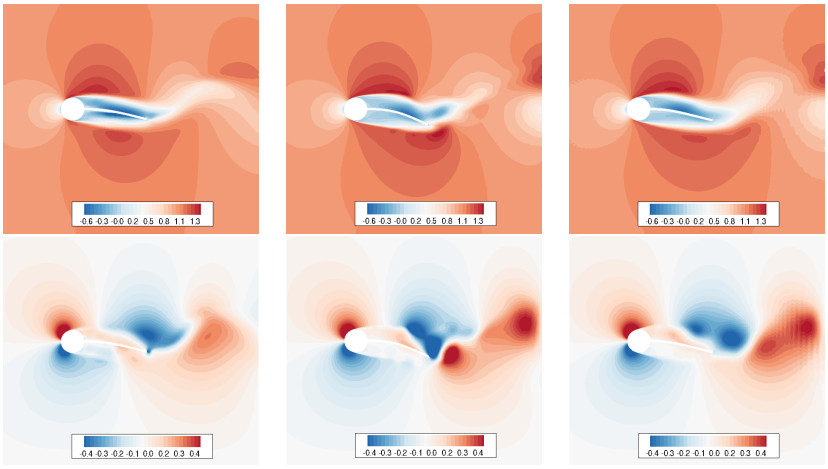

(a) (b) (c)

Fig. 5.21: FSI-PfS-1a: Comparison between (a) 2-d URANS, (b) 3-d URANS and (c) LES [73], for normalized u (top row) and v (bottom row) velocity at time $t = 3T_{FSI}/4$.

Figure 5.20 shows the u and v velocity contours for $t = T_{FSI}/2$. At this phase, the structure is in its un-deformed state, and is moving downward. The flow features from the 2-d URANS and the 3-d URANS show similarities with the LES simulation. A similarity between the location of high and low velocity regions from the two simulations and the phase-averaged LES can be observed, however as previously noted the strength of these regions can be observed to be weaker for the 2-d URANS than for the 3-d URANS .

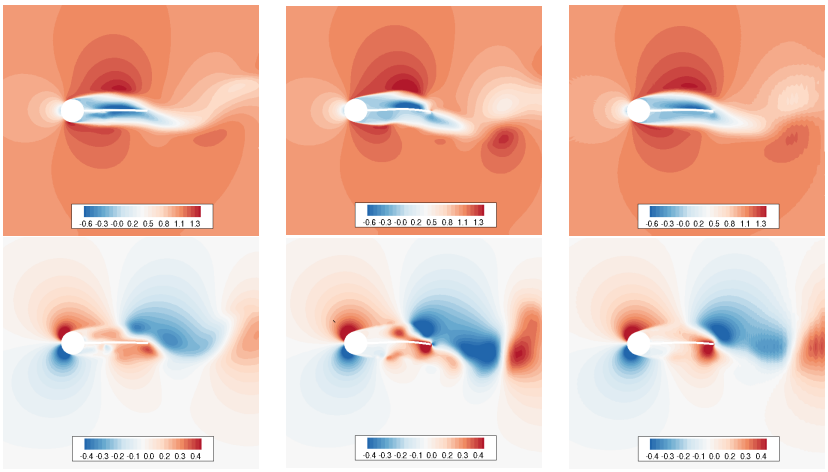

(a) (b) (c)

Fig. 5.22: FSI-PfS-1a: Comparison between (a) 2-d URANS, (b) 3-d URANS and (c) LES [73], for normalized u (top row) and v (bottom row) velocity at time $t = T_{FSI}$.

Figure 5.21 shows the u and v velocity contours for $t = 3T_{FSI}/4$. The structure at this phase has reached its maximum deflection in the downward direction. The flow features for streamwise velocity u at this phase are expected to be symmetric with $t = T_{FSI}/4$. This can be observed by comparing figures 5.21 and 5.19, where a symmetric behavior from the reference LES is much more prominent. The 3-D URANS shows a better estimation of the main flow features predicted by the phase-averaged LES.

Figure 5.22 shows the contour of two velocities for $t = T_{FSI}$. At this phase, the structural oscillation has completed one cycle of motion and the structure is again traveling upwards. The flow features are again symmetric with the phase $t = T_{FSI}/2$. Again the strength of low and high velocity regions for the transverse velocity is weaker for the 2-d URANS in comparison to the 3-d URANS and the reference LES flow field.

Figure 5.23 shows a comparison of the averaged y-displacement of the monitoring point on the structure against the averaged phase angle. A good agree-

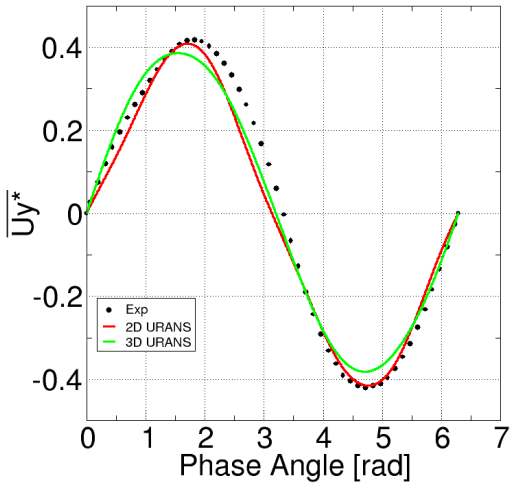

Fig. 5.23: FSI-PfS-1a: Averaged y-displacement comparison for 2-d and 3-d URANS (Exp. from [73]).

ment with the experimental y-displacement can be observed for both simulations. Table 5.10 shows the averaged maxima and minima of y-displacements,

	$\overline{f_{FSI}}$[hz]	$Err.\%$	$\overline{U_y^*\|_{max}}$	$Err.\%$	$\overline{U_y^*\|_{min}}$	$Err.\%$
Exp. [73]	7.10	-	0.418	-	-0.420	-
2-d URANS	7.35	3.5	0.417	-2.1	-0.410	-1.2
3-d URANS	6.96	-2.0	0.387	-7.4	-0.388	-7.6

Table 5.10: FSI-PfS-1a: Comparison between 2-d and 3-d URANS for averaged y-displacement of structural deflections and oscillation frequency.

the averaged frequencies and the corresponding error with respect to the experimental observations. Though the 3-d URANS shows a better agreement with the reference LES in terms of the flow field, the deflections are still under-predicted in comparison to the 2-d URANS. The errors from both simulations are in an acceptable range.

An interesting observation here is the over-prediction of the averaged oscillation frequency by the 2-d URANS flow simulation. From flow simulation studies conducted over a circular cylinder in 2-d URANS configurations [125, 75] the shedding frequency is noted to be over-estimated. The same over-estimation of the vortex shedding frequency is responsible for an over-

estimation of the oscillation frequency here. This has also been observed for the 2-d URANS simulation of the TL1 test case in [83].

FSI-PfS-2a: URANS computations

The FSI-PfS-2a is also studied in 2-d and 3-d URANS fluid simulations. The geometry of this test case is similar to the FSI-PfS-1a. The fluid mesh and the simulation setup remains the same as used for FSI-PfS-1a 2-d and 3-d URANS simulations. The rubber plate and the end mass are discretized with 30×1 and 7×1 8-node linear elements with enhanced strain formulation. An under-relaxation factor of $\omega_{FSI} = 0.25$ is employed and a convergence criterion $\epsilon_{FSI} < 1 \times 10^{-9}$ is satisfied in approximately 15 iterations of the coupling algorithm for both simulations. In the following results of the two simulations i.e. 2-d and 3-d URANS are presented.

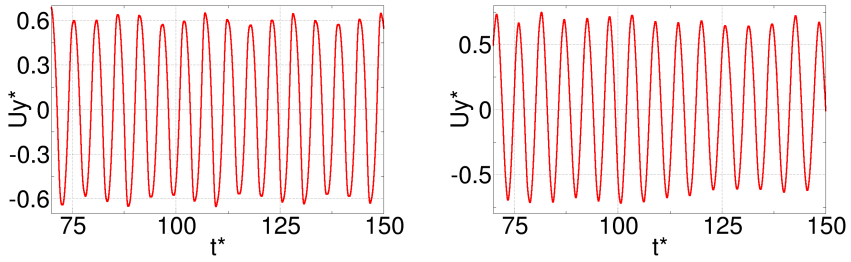

(a) (b)

Fig. 5.24: FSI-PfS-2a: Dimensionless y-displacement of structural deflection vs. dimensionless time (a) Fluid simulations with 2-d URANS (b) Fluid simulation with 3-d URANS.

	Variation of					
	$U_y^*\|_{max}$		$U_y^*\|_{min}$		f_{FSI}[hz]	
	max.	*min.*	*max.*	*min.*	*max.*	*min.*
2-d URANS	0.689	0.551	-0.566	-0.680	12.16	11.33
3-d URANS	0.745	0.640	-0.584	-0.721	12.12	10.95

Table 5.11: FSI-PfS-2a: Variation of maxima and minima of dimensionless y-displacement from 2-d URANS and 3-d URANS.

The dimensionless y-displacement U_y^* against the dimensionless time t^*, for the two simulations is shown in figure 5.24. Table 5.11 shows the variation

of maxima and minima of the y-displacement signal and the frequency from individual oscillation cycles. The maxima of y-displacements from the 2-d and the 3-d URANS are between 0.551 and 0.689, and 0.640 and 0.745, respectively. The minima of displacements lie between -0.566 and -0.680, and -0.584 and -0.721 for the 2-d and the 3-d URANS, respectively. 3-d URANS in this case is producing higher deflections of the structure. The variation of the oscillation frequencies is between 12.16 and 11.33, and 12.12 and 10.95 for the 2-d and the 3-d URANS, respectively. The predicted values of the oscillation frequency for the 2-d URANS is higher than the 3-d URANS. The same was observed for the 2-d URANS simulation of FSI-PfS-1a, as discussed in the previous section.

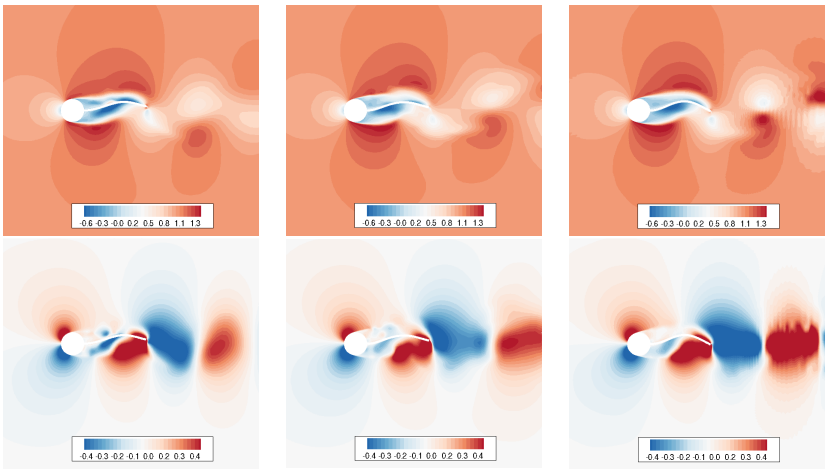

(a) (b) (c)

Fig. 5.25: FSI-PfS-2a: Comparison between (a) 2-d URANS, (b) 3-d URANS and (c) LES [72], for normalized u (top row) and v (bottom row) velocity at time $t = T_{FSI}/24$.

The velocity fields from the two simulations are also compared with the phase-averaged LES velocity field, for three phases in one half of the oscillation cycle. Since the FSI phenomenon is anti-symmetric, it is sufficient to observe the flow features in one half of the oscillation cycle. Figure 5.25 shows a comparison for the streamwise and the transverse velocity at $t = T_{FSI}/24$. The structure at this phase is traveling upwards. From observation, the flow structures from 3-d URANS show a better agreement with the reference flow field in comparison to the 2-d URANS.

Figure 5.26 shows a comparison of the velocity fields at $t = 5T_{FSI}/24$. The structure at this stage has reached its maximum deflection in the upward direction and starts to move in the downward direction. Again from observation

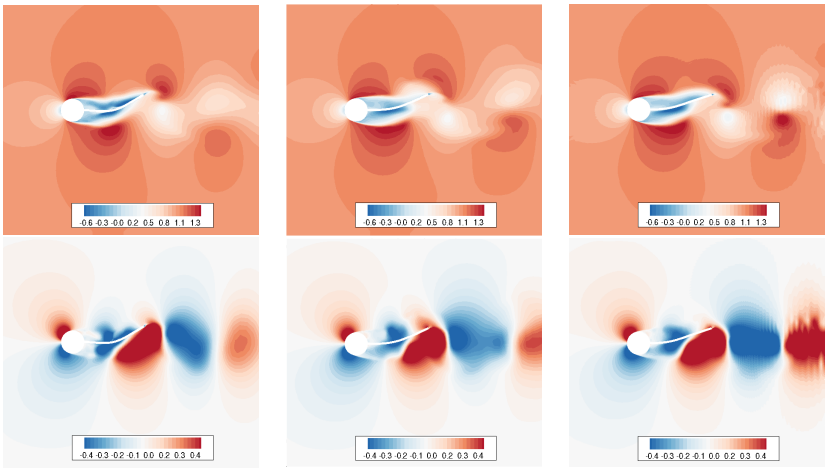

(a) (b) (c)

Fig. 5.26: FSI-PfS-2a: Comparison between (a) 2-d URANS, (b) 3-d URANS and (c) LES [72], for normalized u (top row) and v (bottom row) velocity at time $t = 5T_{FSI}/24$.

the flow structures from 3-d URANS tend to show a better agreement with the phase-averaged LES flow field.

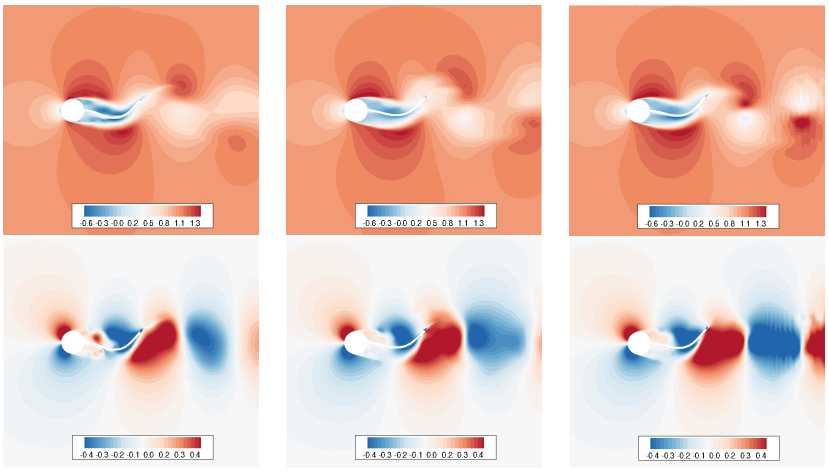

(a) (b) (c)

Fig. 5.27: FSI-PfS-2a: Comparison between (a) 2-d URANS, (b) 3-d URANS and (c) LES [72], for normalized u (top row) and v (bottom row) velocity at time $t = 9T_{FSI}/24$.

Figure 5.27 shows a comparison for the velocity fields at $t = 9T_{FSI}/24$. The structure is traveling downward and bends in a concave form. The flow features from 3-d URANS can be observed to have a better agreement with phase-averaged LES in comparison to the 2-d URANS.

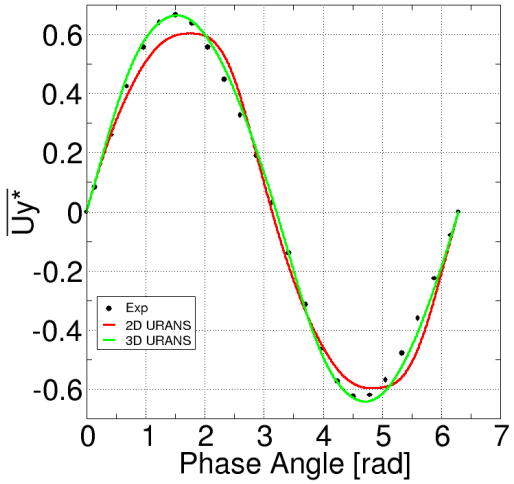

Fig. 5.28: FSI-PfS-2a: Averaged y-displacement comparison for 2-d and 3-d URANS (Exp. from [72]).

	$\overline{f_{FSI}}$[hz]	$Err.\%$	$\overline{U_y^*\|_{max}}$	$Err.\%$	$\overline{U_y^*\|_{min}}$	$Err.\%$
Exp. [72]	11.25	-	0.667	-	-0.629	-
2-d URANS	11.79	4.8	0.603	-9.6	-0.596	-5.2
3-d URANS	11.45	1.8	0.682	2.2	-0.658	4.6

Table 5.12: FSI-PfS-2a: Comparison between 2-d and 3-d URANS for averaged y-displacement of structural deflections and oscillation frequency.

Figure 5.28 shows the averaged y-displacement of the monitoring point on the structure against the averaged phase angle of the oscillation. The 3-d URANS produces a very good prediction of the averaged structural deflection, while for the 2-d URANS the difference with experimental result is higher than for 3-d URANS. Table 5.12 shows the averaged maximum and minimum y-displacements and the averaged oscillation frequencies from the two simulations in comparison to the experimental results. From the 2-d URANS, the averaged deflections predicted are lower than the experimental observations,

also the oscillation frequency is over-predicted. The 3-d URANS simulation show a better agreement with the experimental data. The observation about over-prediction of the oscillation frequency from the 2-d URANS has been discussed in the previous section for the 2-d URANS simulation of FSI-PfS-1a.

5.5.3 FSI tests with Scale Resolving Models

The three turbulent FSI cases are also studied in a DDES simulation with $k-\epsilon-\zeta-f$ as the baseline RANS model. An LES with dynamic Smagorinsky model is also studied for the TL1 test case. A simulation for FSI-PfS-1a with material damping model is also performed. The results and discussion is divided based on the test cases in the following sections.

TL1: DDES and LES

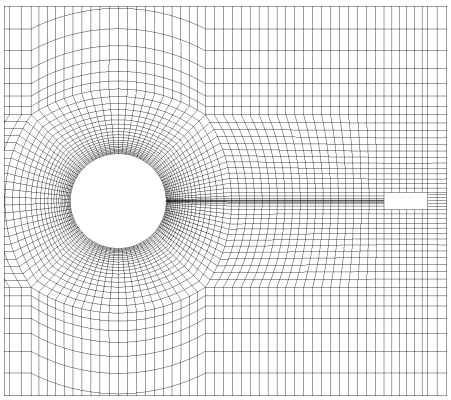

Fig. 5.29: TL1: Fluid grid around the structure, every 4^{th} grid line is visible.

Figure 5.29 shows the grid[3] employed for the TL1 simulation with the DDES turbulence model. The grid used for the LES has similar block structuring but more control volumes. The grid extends 300mm in the upstream direction and 800mm in the downstream direction from the center of the cylinder. While in the y and z direction the grid is 240mm and 180mm re-

[3] The grid for both simulations is provided by a study previously conducted at FNB, TU Darmstadt by Reimann [83]

spectively, matching the dimension of the test section in the experimental setup. Table 5.13 gives the number of control volumes for both grids and the

	No. of CVs	Δt	No. of processors
DDES	12.5×10^6	1.5×10^{-4}s	48
LES	39.8×10^6	1.5×10^{-4}s	196

Table 5.13: TL1: Number of control volumes and time-step sizes.

time-step sizes used to perform the simulation. The number of processors[4] employed for the parallel fluid simulation are also shown in the table.

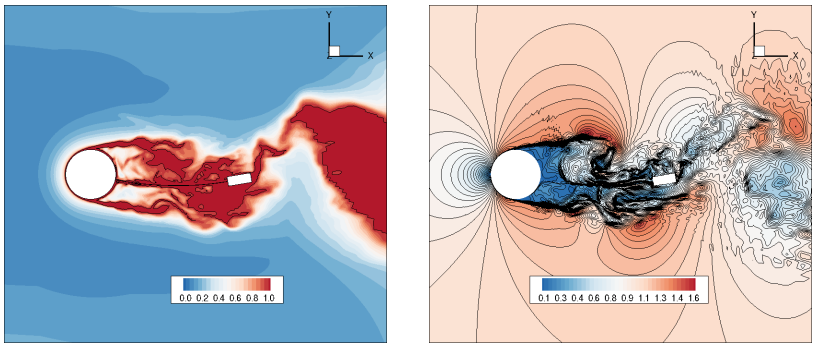

(a) (b)

Fig. 5.30: TL1: DDES (a) DES length scale to RANS length scale ratio l_{DES}/l_{RANS} (b) Normalized velocity magnitude u_{mag}/u_∞.

The structural subproblem for both simulations is discretized with 1840 8-node linear brick elements with enhanced strain formulation. The second order implicit Newmark method is used to advance the solution in time for the structural subproblem. For discretization of convective fluxes in the fluid solver a hybrid blending approach between CDS and GAMMA [43] schemes is employed. This approach employed for the DDES is described in [112], while the FASTEST implementation has been studied in [83]. In the LES simulation with the dynamic Smagorinsky model, the non-dissipative 2nd order CDS is employed. For both simulations time discretization is performed with the 2nd order implicit backward differencing scheme.

Interpolation and data transfer between two codes has been handled via MpCCI. Both simulations required a very low value of the under-relaxation

[4] Both simulations are performed on the high performance computing machines at HHLR TU Darmstadt.

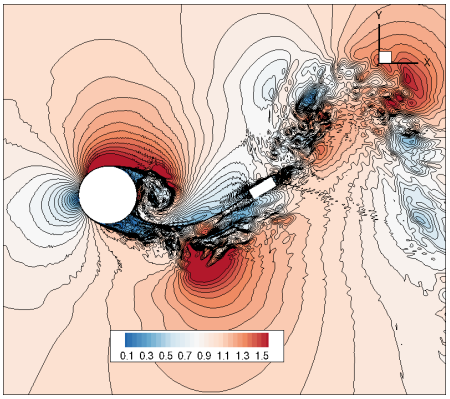

Fig. 5.31: TL1: LES with Smagorinsky model, instantaneous normalized velocity magnitude u_{mag}/u_{∞}.

parameter $\omega^{FSI} = 0.04$ for the structural displacements. For coupling acceleration 0^{th} order force extrapolation is employed. The convergence criterion of $\epsilon_{FSI} < 5 \times 10^{-9}$ is satisfied in approximately 30 coupling iterations for both simulations. Figure 5.30 shows the normalized instantaneous velocity magnitude and the DES to RANS length scale ratio. The contours of l_{DES}/l_{RANS} in figure 5.30 are plotted to identify the RANS and the LES regions in the hybrid simulation, where $l_{DES}/l_{RANS} < 1$ signifies an LES region and $l_{DES}/l_{RANS} \geq 1$ indicates a RANS region. The solid line in the plot of l_{DES}/l_{RANS} indicate a l_{DES}/l_{RANS}=1. From the figure it can be seen that the shear and the boundary layers are in a RANS region, as expected of a DDES simulation. Instantaneous velocity magnitude contours in the same figure show the presence of small scale motions in the wake of the cylinder, indicating a resolution of small scale motions in an LES region. Figure 5.31 shows the contours of instantaneous velocity magnitude for the LES. The contours indicate the presence of small scale fluid motions resolved by the LES model.

	$\overline{f_{FSI}}$[hz]	$Err.\%$	$\overline{\phi_{shift}}$[deg]	$Err.\%$	$\overline{U_y^*\|_{max}}$	$Err.\%$	$\overline{U_y^*\|_{min}}$	$Err.\%$
Exp. [30]	4.45	-	95	-	1.12	-	-1.11	-
DDES	4.37	-1.8	84	-11.6	1.24	10.7	-1.25	12.6
LES	4.37	-1.8	83	-12.6	1.25	11.6	-1.26	13.5

Table 5.14: TL1: Comparison between DDES and LES for averaged y-displacement of structural deflections and oscillation frequency.

Table 5.14 draws a quantitative comparison for the oscillation frequency of the structure f_{FSI}, the end mass phase delay ϕ_{shift} i.e. phase shift between

$y = 0$ crossing of the rotating cylinder and the end mass, and y extrema of the end mass normalized by the cylinder diameter. The corresponding differences with the experimental data are also shown. The prediction of the averaged frequency from the two simulations show a very good agreement with the experimental data. While higher differences are observed for the maximum and minimum y-displacement of the end mass excursions. The difference between phase delay from the simulation and the experiment is also higher.

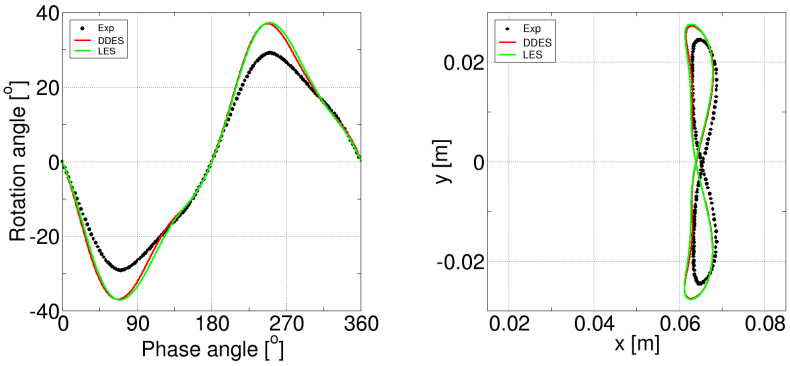

(a) (b)

Fig. 5.32: TL1: (a) Averaged cylinder rotation angle plotted against time phase angle (b) Trailing edge trajectory, Exp. data from [30].

Figure 5.32 plots the phase-averaged rotation angle of the cylinder against the averaged phase angle, and the averaged trailing edge trajectory. The averaging for the DDES simulation has been performed for 13 oscillation cycles, while for the LES averaging has been performed for just 7 oscillation cycles. The rotation angle of the cylinder and the end mass trajectory show a good agreement with the experimental trajectories, except at the extrema, where the differences are maximal. However, both simulations agree very well with each other and the differences between extrema predicted from the two simulations are within 2% of each-other.

FSI-PfS-1a: DDES

This section discusses the results of FSI-PfS-1a with a DDES simulation. The material damping is known to effect the oscillation characteristics of the structure, specially in the first bending mode. Therefore an FSI simulation accounting for the material damping is also performed. A calibration of

the Rayleigh damping parameters performed in [73] is used for the material damping model.

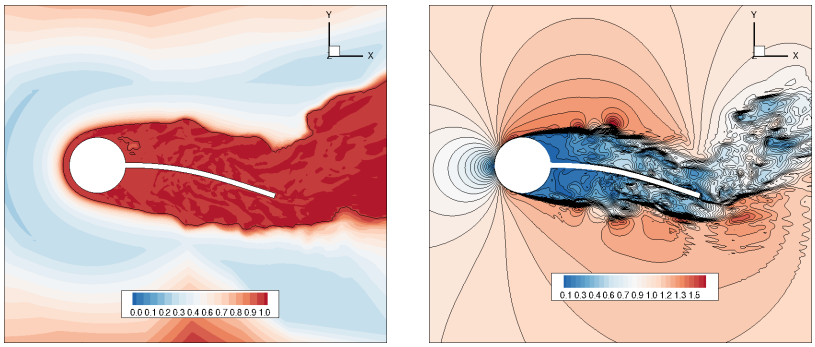

(a) (b)

Fig. 5.33: FSI-PfS-1a: DDES a) DES length scale to RANS length scale ratio l_{DES}/l_{RANS} (b) Normalized velocity magnitude u_{mag}/u_{∞}.

The fluid mesh for the study is the same that has been discussed earlier for the 3-d URANS simulations of FSI-PfS-1a test case, and contains 1.7 million control volumes approximately. The structural mesh also remains unchanged and contains 30×1 8-node linear brick elements with enhanced strain formulation. The hybrid blending approach is employed for discretization of convective fluxes. The fluid solver employs the 2^{nd} order implicit backward differencing scheme for time discretization and the structural solver employs the Newmark method to advance the solution in time. A time-step size of $\Delta t = 7 \times 10^{-5}$s is used to perform the simulation, where the CFL number varied between 1.2 and 2.6. However, the CFL number remains less than unity around the cylinder and in the separated shear layers. The coupling acceleration is performed with a 0^{th} order force extrapolation. An under-relaxation factor of $\omega^{FSI} = 0.3$ is applied for structural displacements, which resulted in approximately 8 coupling iterations to satisfy a convergence criterion of $\epsilon_{FSI} < 1 \times 10^{-9}$. For the simulation with material damping the Rayleigh damping parameters are set as $\alpha = 0$ and $\beta = 0.017$, as calibrated in [73]. The mass proportional damping parameter α is assumed to be zero, with the reason that it models the decay of damping effects in higher modes of the oscillation.

Figure 5.33 shows the DES to RANS length scale ratio and normalized instantaneous velocity magnitude contours around the structure. From figure 5.33 it can be seen, that the flow in the wake of the cylinder and around the rubber plate is in the RANS modeling region, where $l_{DES}/l_{RANS} \geq 1$. It is expected that with a dense mesh some part of the flow in the cylinder wake

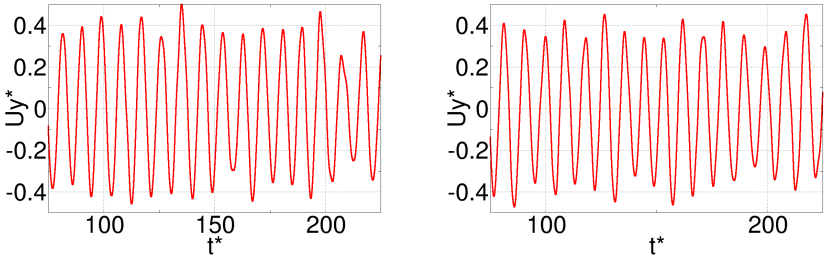

(a) (b)

Fig. 5.34: FSI-PfS-1a: Dimensionless y-displacement of structural deflection vs. dimensionless time (a) without material damping (b) with material damping.

and around the plate can be resolved with an LES in a hybrid RANS/LES approach, as it was observed for the TL1 simulation in figure 5.30.

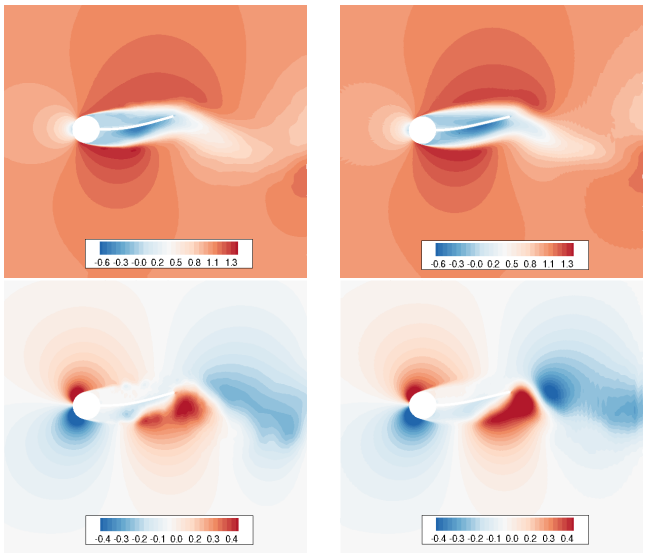

(a) (b)

Fig. 5.35: FSI-PfS-1a: Comparison between (a) DDES without material damping, (b) LES [73], for normalized u (top row) and v (bottom row) velocity at time $t = T_{FSI}/4$.

Figure 5.34 shows a variation of the dimensionless y-displacement of the monitoring point with respect to the dimensionless time. A quasi-periodic

	Variation of					
	$U_y^*\|_{max}$		$U_y^*\|_{min}$		f_{FSI}[hz]	
	max.	*min.*	*max.*	*min.*	*max.*	*min.*
DDES	0.505	0.254	-0.250	-0.451	7.40	6.43
DDES with Damping	0.452	0.178	-0.169	-0.472	7.59	5.92

Table 5.15: FSI-PfS-1a: Variation of maxima and minima of dimensionless y-displacement from DDES simulations with and without material damping.

behavior of the structural deflections, with minor cycle to cycle variations can be observed. Table 5.15 shows the variation of maxima and minima of the y-displacement signal and frequency from individual oscillation cycles. The maxima of U_y^* from the two simulations are observed to vary between 0.505 and 0.254 for the simulation without damping and between 0.452 and 0.178 for the simulation with damping. The minima of U_y^* for the two simulations also show a variation between -0.250 and -0.451 for the simulation without damping and between -0.169 and -0.472 for the simulation with damping. The oscillation frequency of the structure varied between 7.40 and 6.43 for the simulation without damping and between 7.59 and 5.92 for the simulation with damping. The standard deviation of the extrema from both simulations is less than ± 0.07. The observations presented here and the averaged results presented later are based on 37 oscillation cycles for both simulations.

Figure 5.35 shows a comparison of normalized u and v velocities from the DDES without material damping against the reference LES study for $t = T_{FSI}/4$. The contour plots are time phase-averaged for 10 oscillation cycles of the structure, as well as averaged in spanwise direction. The structure at this phase is at its maximum displacement in upward direction. The similarities in flow instabilities is very clear and a good agreement with the flow field from the reference LES can be observed.

Figure 5.36 shows the normalized velocity contours comparison with LES at $t = T_{FSI}/2$. The structure at this phase is at its undeformed position and it is going in the downward direction. The comparison between flow instabilities and length of shear layers can be observed. The magnitude of instabilities for the transverse flow velocity are weaker than predicted by the reference LES.

Figure 5.37 shows a comparison between the current simulation and the reference LES for $t = 3T_{FSI}/4$. The structure is at its maximum displacement in the downward direction. The similarities between flow features from the DDES and the reference LES is very obvious. However, the strength of instabilities in the transverse flow velocity is under-predicted. Also the antisymmetry in the transverse flow velocity features with $t = T_{FSI}/4$ (figure 5.35) can be observed.

Figure 5.38 shows a comparison of the normalized velocity contours at $t = T_{FSI}$. Again the similarities in the flow features can be observed very

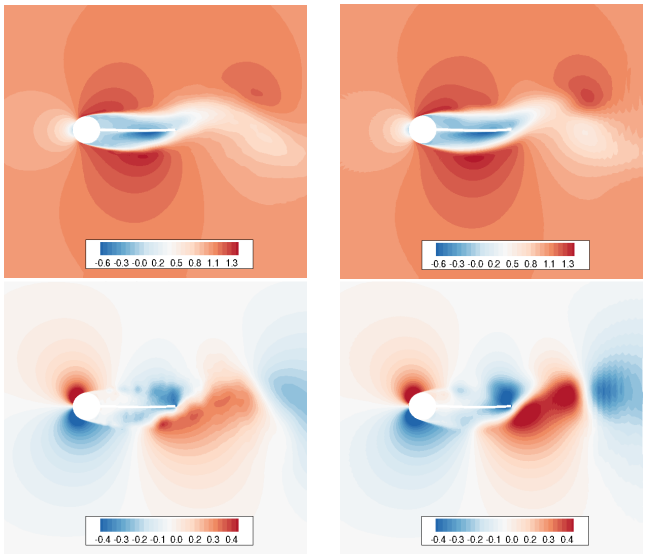

(a) (b)

Fig. 5.36: FSI-PfS-1a: Comparison between (a) DDES without material damping, (b) LES [73], for normalized u (top row) and v (bottom row) velocity at time $t = T_{FSI}/2$.

clearly. The same antisymmetry of the flow features can be observed for $t = T_{FSI}$ in figure 5.38 and $t = T_{FSI}/2$ in figure 5.36.

Figure 5.39 shows the percentage differences between the velocity magnitude from the DDES and the reference LES. The differences are calculated between the averaged flow field variables, and by interpolating LES flow field onto the DDES grid. The minimum differences are observed away from the structure in the wake flow while highest differences are immediately after the cylinder and in shear layers.

A comparison of the averaged y-displacement of the monitoring point on the structure from the two simulations and the experiment is compared in figure 5.40. The difference between simulation with damping and without damping can also be observed for the averaged y-displacement of the structure, where the effect of damping is seen as a reduction in the averaged extrema of the structure.

Table 5.16 shows a comparison for the averaged y extrema of structural deflections, the oscillation frequency and the corresponding errors. The percentage errors for the simulation with damping are clearly higher than without damping. The LES study of this test case [73] with and without damping revealed a better agreement with the experimental results for a simulation taking into account the material damping. In the same study, the structural deflections without damping are significantly higher than the experimental

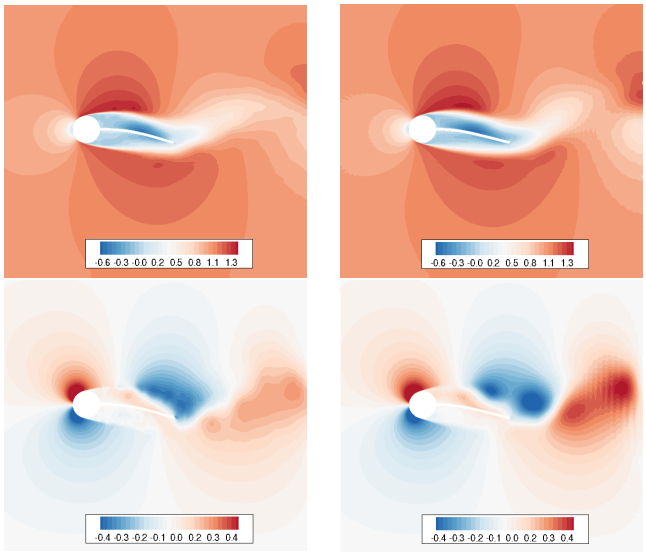

(a) (b)

Fig. 5.37: FSI-PfS-1a: Comparison between (a) DDES without material damping, (b) LES [73], for normalized u (top row) and v (bottom row) velocity at time $t = 3T_{FSI}/4$.

	$\overline{f_{FSI}}$[hz]	$Err.\%$	$\overline{U_y^*\|_{max}}$	$Err.\%$	$\overline{U_y^*\|_{min}}$	$Err.\%$
Exp. [73]	7.10	-	0.418	-	0.420	-
DDES	6.97	-1.8	0.381	-8.8	-0.382	-9.0
DDES with Damping	6.85	-3.5	0.345	-17.5	-0.354	-15.7

Table 5.16: FSI-PfS-1a: Comparison between DDES with and without damping for averaged y-displacement of structural deflections and oscillation frequency.

results and damping reduced the y-displacement by approximately 10% with respect to the reference data. However, in this study the structural deflections are already under-predicted without the material damping, where the damping further reduces the deflections by 8-9%. It is noteworthy, that the the FSI simulations in [73] by De Nayer, not only differ in terms of the turbulence model, but also in terms of the structural model. The study conducted by De Nayer uses shell elements and the material damping is calibrated by simulating the oscillating structure alone with a variation of the damping parameter, which is then compared with the experimental behavior of structural oscillation to estimate the correct value of the damping parameters.

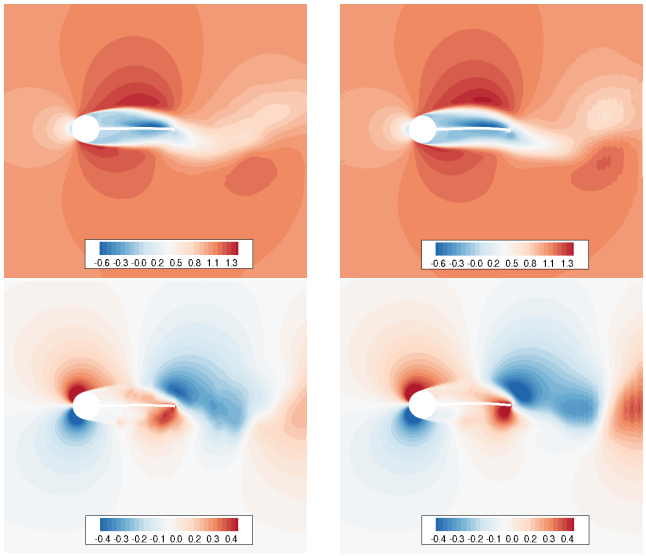

(a) (b)

Fig. 5.38: FSI-PfS-1a: Comparison between (a) DDES without material damping, (b) LES [73], for normalized u (top row) and v (bottom row) velocity at time $t = 3T_{FSI}$.

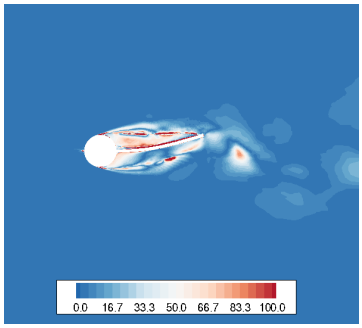

Fig. 5.39: FSI-PfS-1a: Percentage difference of velocity magnitude between DDES and LES[73] at $t = T_{FSI}/4$.

FSI-PfS-2a: DDES

The FSI-PfS-2a test case is simulated again with DDES based on the $k - \epsilon - \zeta - f$ model. The fluid mesh for the study is the same as used for the DDES simulation of FSI-PfS-1a. The structure for the problem is discretized with 30×1 and 7×1 8-node linear brick elements for the rubber plate and

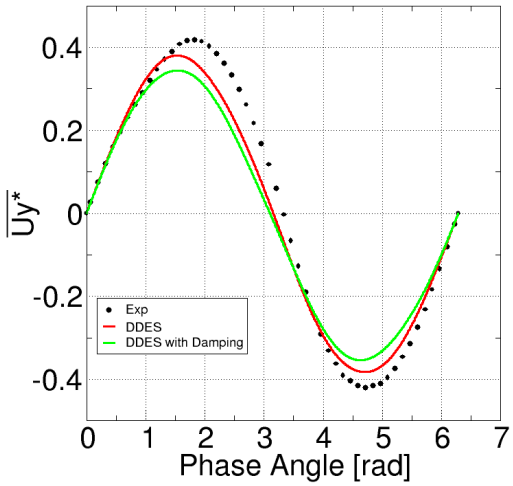

Fig. 5.40: FSI-PfS-1a: Averaged y-displacement comparison DDES with and without damping with experimental data from [73].

the end mass. The discretization employed for the fluid and the structural subproblem is the same as for the FSI-PfS-1a DDES simulations. As for the 2-d and 3-d URANS simulations of FSI-PfS-2a, an under-relaxation factor of $\omega_{FSI} = 0.25$ is used, while the convergence criteria is satisfied in 12 iterations of the coupling algorithm on average. In the following detailed results of the simulation are presented.

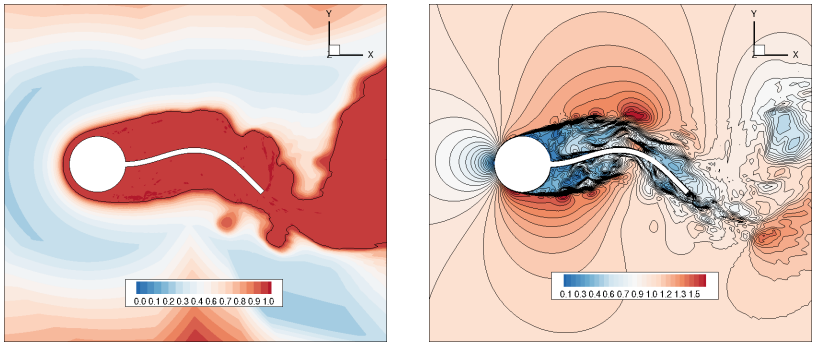

(a) (b)

Fig. 5.41: FSI-PfS-2a: DDES a) DES length scale to RANS length scale ratio l_{DES}/l_{RANS} (b) Normalized velocity magnitude u_{mag}/u_{∞}.

Figure 5.41 shows the DES to RANS length scale ratio and normalized instantaneous velocity magnitude contours. The contours for l_{DES}/l_{RANS} provide and indication of flow regions where the DDES model acts as an LES or as a RANS. Similar to the FSI-PfS-1a the cylinder wake and the shear layers are completely in RANS regions. However a denser mesh would help the model to resolve some parts of the wake in an LES region as observed for the TL1 simulation with DDES. The instantaneous velocity contours show small scale fluctuations in the wake of the cylinder and around the structure, regardless of the region being in RANS mode.

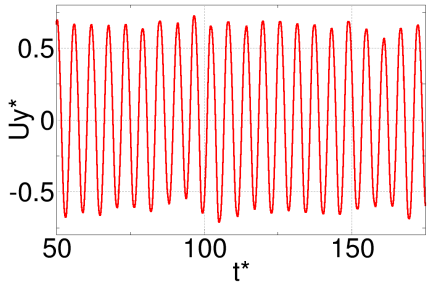

Fig. 5.42: FSI-PfS-2a: Dimensionless y-displacement of structural deflection vs. dimensionless time.

	Variation of					
	$U_y^*\|_{max}$		$U_y^*\|_{min}$		f_{FSI}[hz]	
	max.	*min.*	*max.*	*min.*	*max.*	*min.*
DDES	0.722	0.567	-0.584	-0.721	11.56	10.37

Table 5.17: FSI-PfS-2a: Variation of maxima and minima of dimensionless y-displacement from DDES simulation.

Figure 5.42 shows the dimensionless y-displacement of the monitoring point on the structure plotted against the dimensionless time. The displacement signal is recorded and then averaged for 37 oscillation cycles of the structure. Table 5.17 shows the variation of maxima and minima of y-displacement and the frequency from individual oscillation cycles. The maxima of displacement signal from the monitoring point varied between 0.722 and 0.567, while the variation of the minima is between -0.584 and -0.721. The standard deviations of the maxima and minima are less than 0.04, i.e. within 6% of the averaged maxima, which indicates a very good periodic behavior of the structural oscillations. The frequency of oscillation varies between 11.56 and 10.37.

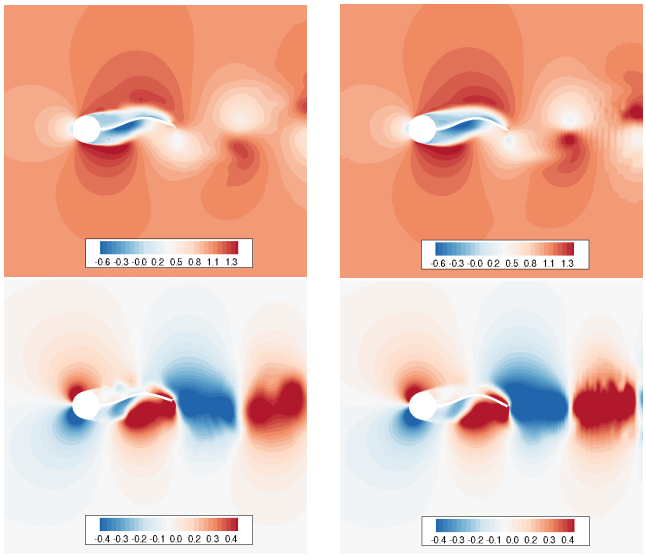

(a) (b)

Fig. 5.43: FSI-PfS-2a: Comparison between (a) DDES (b) LES [72], for normalized u (top row) and v (bottom row) velocity at time $t = T_{FSI}/24$.

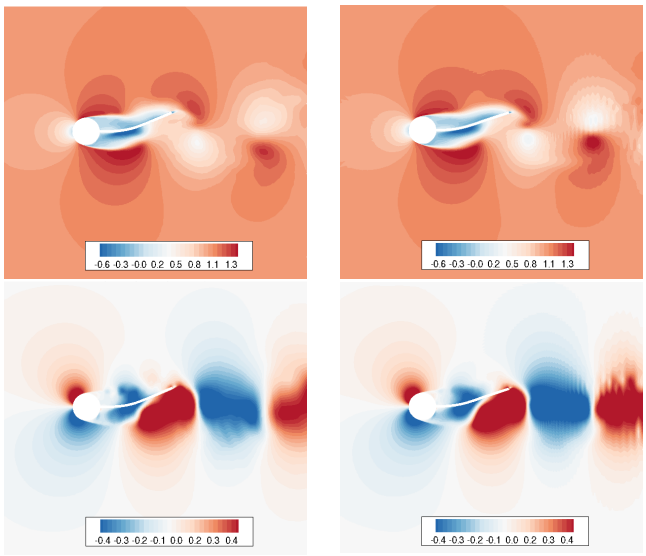

(a) (b)

Fig. 5.44: FSI-PfS-2a: Comparison between (a) DDES (b) LES [72], for normalized u (top row) and v (bottom row) velocity at time $t = 5T_{FSI}/24$.

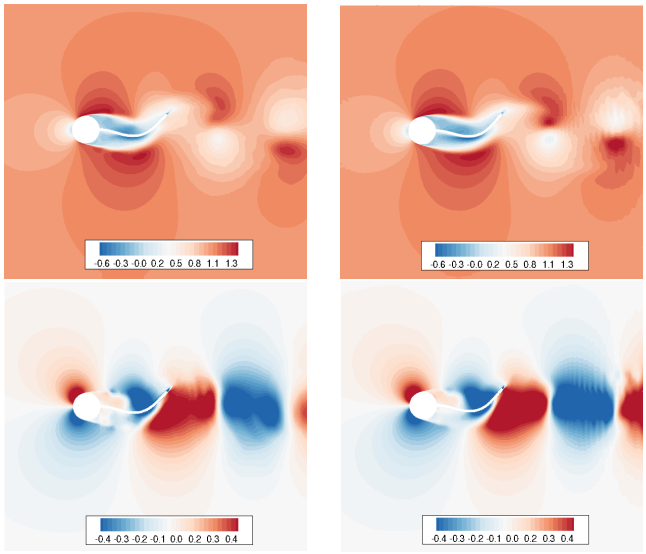

(a) (b)

Fig. 5.45: FSI-PfS-2a: Comparison between (a) DDES (b) LES [72], for normalized u (top row) and v (bottom row) velocity at time $t = 9T_{FSI}/24$.

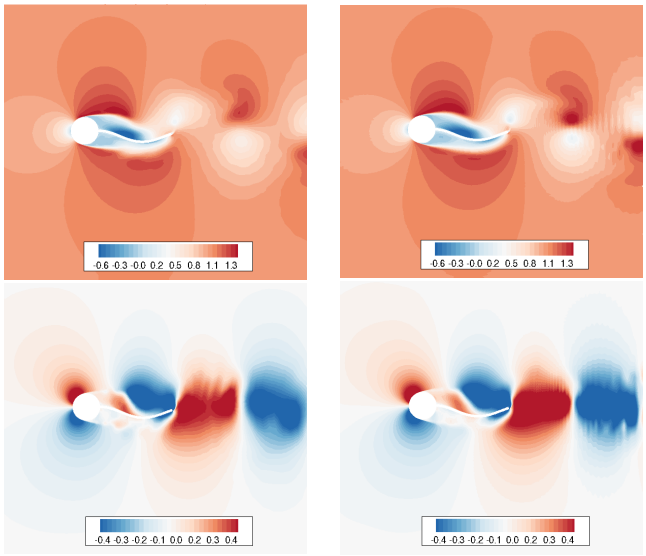

(a) (b)

Fig. 5.46: FSI-PfS-2a: Comparison between (a) DDES (b) LES [72], for normalized u (top row) and v (bottom row) velocity at time $t = 13T_{FSI}/24$.

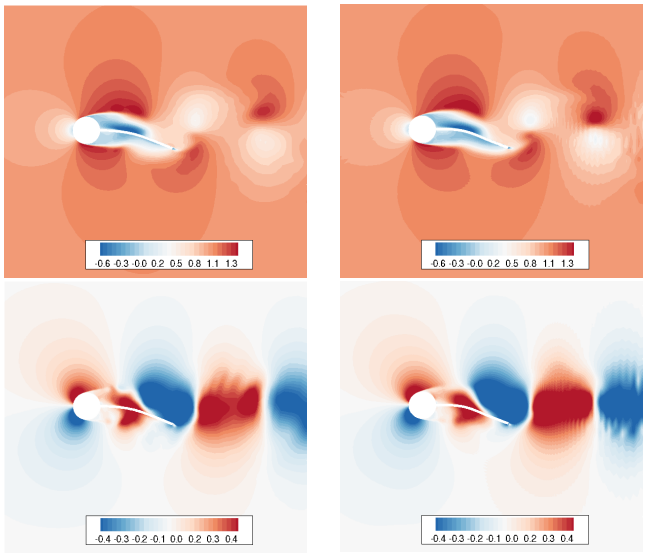

(a) (b)

Fig. 5.47: FSI-PfS-2a: Comparison between (a) DDES (b) LES [72], for normalized u (top row) and v (bottom row) velocity at time $t = 17T_{FSI}/24$.

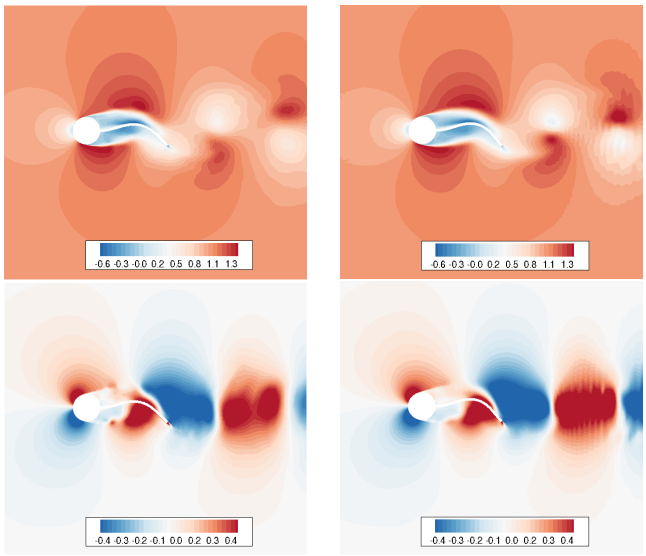

(a) (b)

Fig. 5.48: FSI-PfS-2a: Comparison between (a) DDES (b) LES [72], for normalized u (top row) and v (bottom row) velocity at time $t = 21T_{FSI}/24$.

Figures 5.43 to 5.48 shows a comparison of the streamwise and the transverse velocity contours at six locations in the oscillation cycle for $T_{FSI}/24$, $5T_{FSI}/24$, $9T_{FSI}/24$, $13T_{FSI}/24$, $17T_{FSI}/24$ and $21T_{FSI}/24$. The velocity fields are phase-averaged for 10 oscillation cycles of the structure, while the averaging is performed in the spanwise direction as well.

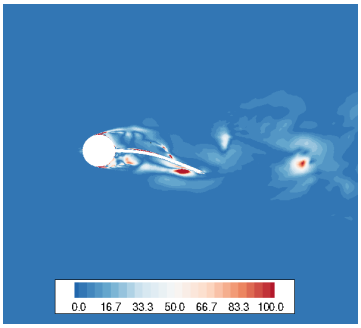

Fig. 5.49: FSI-PfS-2a: Percentage difference of velocity magnitude between DDES and LES[72] at $t = 17T_{FSI}/24$.

Figure 5.49 shows the absolute percentage difference between the velocity magnitude from the current simulation and the reference LES at $t = 17T_{FSI}/24$. The largest differences can be observed in the vicinity of the structure and close to the origin of the shear layers near the cylinder. While a visual comparison of errors in the velocity fields from the DDES simulations i.e. FSI-PfS-1a (figure 5.39) and FSI-PfS-2a (figure 5.49) reveal a better prediction of the flow field in this simulation.

The averaged y-displacement of the monitoring point on the structure is compared with the experimental results in figure 5.40. A very good agreement can be observed with the experimental data.

	$\overline{f_{FSI}}$[hz]	$Err.\%$	$\overline{U_y^*\|_{max}}$	$Err.\%$	$\overline{U_y^*\|_{min}}$	$Err.\%$
Exp. [47]	11.25	-	0.667	-	-0.629	-
DDES	10.85	-3.5	0.660	-1.1	-0.642	2.1

Table 5.18: FSI-PfS-2a: Comparison between DDES and experimental results for averaged y-displacement of structural deflections and oscillation frequency.

Table 5.18 shows the result for the averaged extrema of the structure and the oscillation frequency, with the corresponding errors. The averaged extrema and the oscillation frequency are very well predicted from the simulation in comparison to the the experiment.

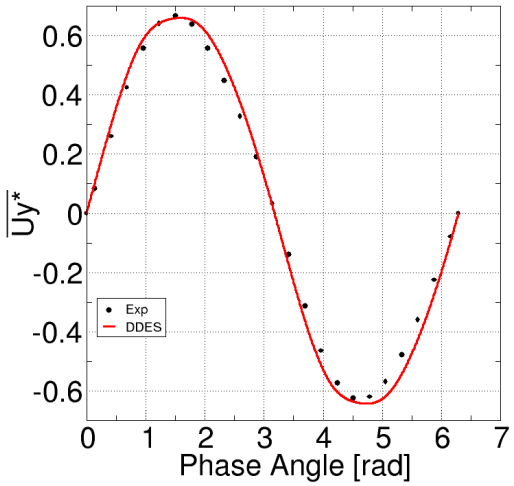

Fig. 5.50: FSI-PfS-2a: Averaged y-displacement comparison for DDES with experimental data from [47].

Chapter 6
Conclusion

6.1 Summary

The work presented in this thesis concerns the fluid-structure interaction in turbulent flows. In this regard an efficient Poisson equation based method for wall distance calculation is implemented for use in turbulence models, such as the Delayed Detached Eddy Simulation (DDES) model. The performance of the method is studied with a comparison of the calculated values of wall distance in a channel and a square against the measured values of wall distance. The comparison shows a better prediction of the wall distance in close proximity of walls, however away from walls the prediction deteriorates.

A wall y^+ insensitive wall treatment approach, which is called the Compound Wall Treatment (CWT) [81], has been implemented in the flow solver FASTEST. The CWT implementation has been validated on stationary grids with a channel flow test case at a $Re_\tau = 590$. The flow simulations of the channel on grids with varying wall y^+ values demonstrated satisfactory results. A test of CWT for FSI simulations has been performed with the FSI-PfS-1a test case. The grid employed for the study was designed with a wall $y^+ \approx 15$ and simulations with and without CWT were performed. A comparison between the oscillation characteristics from the two simulations revealed a better prediction of the structural deflections and the oscillation frequency with the application of CWT.

A comparison of coupling acceleration techniques has been performed in laminar and turbulent flow regimes in a lid driven cavity flow with flexible bottom wall. The IQN-ILS technique required the least number of iterations for convergence in both regimes. From previous studies with this test case, it is obvious that the convergence rate of an acceleration technique is problem dependent.

The FSI-PfS-1a test case has been simulated with two different element formulations in the structural solver. The 8-node linear element with enhanced strain formulation and the 20-node higher order element produced

similar structural deflections and oscillation frequencies. However, it was observed that the use of a higher order element for the structural subproblem slowed down the convergence of the coupling algorithm by requiring more iterations for convergence.

The turbulence modeling capabilities of the fluid solver FASTEST have been extended with an implementation of the Wall Adapting Local Eddy (WALE) viscosity model for LES. The calibration of the model constant for the WALE model has been performed with the help of the Decaying homogeneous Isotropic Turbulence (DIT) test case. Further a validation study of the model has been conducted with a 2-d periodic hill flow test case with satisfactory results in comparison to the reference LES. The simulation has been performed on a significantly coarser grid compared to the other LES studies. The CWT treatment has been employed on the upper wall of the 2-d hill case, where the wall $y^+ \approx 15$. The original formulation of the wall normal velocity scale ζ equation in the $k-\epsilon-\zeta-f$ model has been modified on the same lines as proposed for the v^2-f model in [12]. A test of the modified model revealed an improvement in the prediction of ζ in a channel flow test case.

2-d and 3-d URANS computations for FSI-PfS-1a and FSI-PfS-2a have been carried out with the $k-\epsilon-\zeta-f$ turbulence model. The characteristic oscillation frequency and structural deflections are adequately predicted for both 2-d and 3-d URANS simulations. However, in terms of the reproducible periodic behavior, FSI-PfS-2a showed better characteristics with a lower cycle to cycle variation than the FSI-PfS-1a. 2-d URANS FSI simulations for two test cases produced an over-prediction of the oscillation frequency. It has been noticed that in 2-d URANS simulation of a sub-critical flow over a cylinder, the vortex shedding frequency is reported to be over-estimated [125, 75]. The over-prediction of the oscillation frequency has been attributed to an increased vortex shedding frequency in 2-d URANS simulations. 3-d computations for both test cases also show a satisfactory agreement with the experimental data, with better predictions for FSI-PfS-2a. The flow field from 2-d and 3-d URANS has also been compared with the reference LES. The 3-d URANS computations revealed a better prediction of the flow instabilities in comparison to the 2-d URANS. Both test cases have been simulated with the DDES model as well. The DDES of two test cases revealed a better prediction of experimental results for FSI-PfS-2a. The issue of damping for FSI-PfS-1a has been studied by performing DDES computations with the Rayleigh damping model. The effect of damping further reduced the structural deflections in comparison to the DDES simulation of FSI-PfS-1a without damping. In this case, the damping deteriorated the predictions further in comparison to the experimental data. However, this pronounced effect of damping cannot be ignored, but it is noteworthy that the calibration of the material damping in [73] has been performed with a shell element formulation, while this study employs solid elements for the structural simulation.

Two simulations with the DDES and the dynamic Smagorinsky model have been performed for the TL1 test case with a very dense mesh. The characteristics of the structural oscillation reveal a satisfactory agreement with the experimental data. The maximum differences are observed for end mass extrema, with an over-prediction of maximum 13%. The two simulations agree very well with a difference for extrema of less than 2%. This close agreement between the LES and the DDES on a relatively coarser mesh is an indication of the desired model performance from the DDES.

6.2 Outlook

For the future work, it would be interesting to investigate the discrepancies in the prediction of FSI-PfS-1a. The structural oscillation of FSI-PfS-1a with the 3-d URANS and the DDES model are under-predicted, without consideration of the material damping. However, the DDES simulation is performed for a considerably coarser mesh, where only some part of the flow domain is in an LES region. A more complex or sophisticated turbulence modeling approach could help to improve the result or find a reason for this under-prediction. A DDES simulation of the test case on a further refined mesh resolving the turbulence in some part of the wake immediately after the cylinder, would also be interesting. Further, the WALE model implemented in this study has not been validated with an FSI simulation, such a validation study could be performed with one of the FSI test cases.

Further more complex turbulent modeling approaches can be validated in an FSI scenario, with the help of the test cases studied in this work or even more challenging test cases can be employed in the current FSI frame work, like the flow over a flexible hemisphere recently proposed in [123].

List of Tables

List of Figures

References

1. MpCCI - Mesh-Based Parallel Code Coupling Interface. User Guide V3.0. *Fraunhofer, SCAI*, 2004.
2. FASTEST - User Manual, Institute of Numerical Methods in Mechanical Engineering. *Technische Universität Darmstadt*, 2005.
3. F. P. T. Baaijens. A fictitious domain/mortar element method for fluid-structure interaction. *International Journal for Numerical Methods in Fluids*, 35(7):743–761, 2001.
4. J. Boussinesq. *Théorie de l'écoulmnent tourbillonnant et tumultuex des liquides dans les lits rectilignes à grande section*, volume 1. Gauthier-Villars, 1897.
5. M. Breuer, D. Lakehal, and W. Rodi. Flow around a surface mounted cubical obstacle: comparison of les and rans-results. In *Computation of Three-Dimensional Complex Flows*, pages 22–30. Springer, 1996.
6. M. Breuer and M. Münsch. FSI of the turbulent flow around a swiveling flat plate using large-eddy simulation. In *International Workshop on Fluid-Structure Interaction–Theory, Numerics and Applications*, pages 31–43, 2008.
7. M. Breuer, G. D. Nayer, M. Münsch, T. Gallinger, and R. Wüchner. Fluid-structure interaction using a partitioned semi-implicit predictor-corrector coupling scheme for the application of large-eddy simulation. *Journal of Fluids and Structures*, 29:107 – 130, 2012.
8. M. Breuer, N. Peller, C. Rapp, and M. Manhart. Flow over periodic hills – numerical and experimental study in a wide range of reynolds numbers. *Computers & Fluids*, 38(2):433 – 457, 2009.
9. H.-J. Bungartz, F. Lindner, B. Gatzhammer, M. Mehl, K. Scheufele, A. Shukaev, and B. Uekermann. preCICE - A Fully Parallel Library for Multi-Physics Surface Coupling. *Computers and Fluids*, pages 1–9, 2016.
10. P. Causin, J. Gerbeau, and F. Nobile. Added-mass effect in the design of partitioned algorithms for fluid-structure problems. *Computer Methods in Applied Mechanics and Engineering*, 194(42?44):4506 – 4527, 2005.
11. K.-Y. Chien. Predictions of channel and boundary-layer flows with a low-reynolds-number turbulence model. *AIAA journal*, 20(1):33–38, 1982.
12. L. Davidson, P. Nielsen, and A. Sveningsson. Modifications of the v2-f model for computing the flow in a 3d wall jet. *Turbulence Heat and Mass Transfer 4, Hanjalić, K., Nagano, Y., Tummers, M.*, 2003.
13. J. W. Deardorff. A numerical study of three-dimensional turbulent channel flow at large reynolds numbers. *Journal of Fluid Mechanics*, 41(02):453–480, 1970.
14. J. Degroote. Partitioned simulation of fluid-structure interaction. *Archives of Computational Methods in Engineering*, 20(3):185–238, 2013.

15. J. Degroote, R. Haelterman, S. Annerel, A. Swillens, P. Segers, and J. Vierendeels. An interface quasi-newton algorithm for partitioned simulation of fluid-structure interaction. In *International Workshop on Fluid-Structure Interaction. Theory, Numerics and Applications*, page 55. Kassel University Press GmbH, 2009.
16. I. Demirdžić and M. Perić. Space conservation law in finite volume calculations of fluid flow. *International Journal for Numerical Methods in Fluids*, 8(9):1037–1050, 1988.
17. J. Donea, S. Giuliani, and J. Halleux. An arbitrary lagrangian-eulerian finite element method for transient dynamic fluid-structure interactions. *Computer Methods in Applied Mechanics and Engineering*, 33(1):689 – 723, 1982.
18. F. Ducros, F. Nicoud, and T. Poinsot. Wall-adapting local eddy-viscosity models for simulations in complex geometries. *Numerical Methods for Fluid Dynamics VI*, pages 293–299, 1998.
19. P. Durbin. Separated flow computations with the k-epsilon-v-squared model. *AIAA journal*, 33(4):659–664, 1995.
20. P. Durbin. On the k-3 stagnation point anomaly. *International Journal of Heat and Fluid Flow*, 17(1):89 – 90, 1996.
21. P. A. Durbin. Near-wall turbulence closure modeling without "damping functions". *Theoretical and Computational Fluid Dynamics*, 3(1):1–13, 1991.
22. C. Farhat, K. G. van der Zee, and P. Geuzaine. Provably second-order time-accurate loosely-coupled solution algorithms for transient nonlinear computational aeroelasticity. *Computer Methods in Applied Mechanics and Engineering*, 195(17-18):1973 – 2001, 2006. Fluid-Structure Interaction.
23. J. H. Ferziger and M. Peric. *Computational methods for fluid dynamics*. Springer Science & Business Media, 2012.
24. J. Fröhlich, C. P. Mellen, W. Rodi, L. Temmerman, and M. A. Leschziner. Highly resolved large-eddy simulation of separated flow in a channel with streamwise periodic constrictions. *Journal of Fluid Mechanics*, 526:19–66, 3 2005.
25. J. Fröhlich and D. von Terzi. Hybrid LES/RANS methods for the simulation of turbulent flows. *Progress in Aerospace Sciences*, 44(5):349 – 377, 2008.
26. M. Germano, U. Piomelli, P. Moin, and W. H. Cabot. A dynamic subgrid-scale eddy viscosity model. *Physics of Fluids A: Fluid Dynamics*, 3:1760, 1991.
27. R. Glowinski, T.-W. Pan, T. Hesla, and D. Joseph. A distributed lagrange multiplier/fictitious domain method for particulate flows. *International Journal of Multiphase Flow*, 25(5):755 – 794, 1999.
28. R. Glowinski, T.-W. Pan, and J. Periaux. A fictitious domain method for dirichlet problem and applications. *Computer Methods in Applied Mechanics and Engineering*, 111(3):283 – 303, 1994.
29. J. Gomes, M. Münsch, M. Breuer, and H. Lienhart. *Flow–Induced Oscillation of a Flat Plate – A Fluid–Structure–Interaction Study Using Experiment and LES*, pages 347–354. Springer Berlin Heidelberg, Berlin, Heidelberg, 2010.
30. J. P. Gomes and H. Lienhart. Fluid–structure interaction-induced oscillation of flexible structures in laminar and turbulent flows. *Journal of Fluid Mechanics*, 715:537–572, 2013.
31. W. J. Gordon and C. A. Hall. Construction of curvilinear co-ordinate systems and applications to mesh generation. *International Journal for Numerical Methods in Engineering*, 7(4):461–477, 1973.
32. K. Hanjalić, M. Popovac, and M. Hadžiabdić. A robust near-wall elliptic-relaxation eddy-viscosity turbulence model for CFD. *International Journal of Heat and Fluid Flow*, 25(6):1047 – 1051, 2004.
33. M. Heck, D. C. Sternel, M. Schäfer, and S. Yigit. Influence of numerical and physical parameters on an implicit partitioned fluid-structure solver. In *ECCOMAS CFD 2006: Proceedings of the European Conference on Computational*

Fluid Dynamics, Egmond aan Zee, The Netherlands, September 5-8, 2006. Delft University of Technology; European Community on Computational Methods in Applied Sciences (ECCOMAS), 2006.

34. M. Heil. An efficient solver for the fully coupled solution of large-displacement fluid-structure interaction problems. *Computer Methods in Applied Mechanics and Engineering*, 193(1-2):1 – 23, 2004.
35. H. M. Hilber, T. J. Hughes, and R. L. Taylor. Improved numerical dissipation for time integration algorithms in structural dynamics. *Earthquake Engineering & Structural Dynamics*, 5(3):283–292, 1977.
36. C. Hirt, A. Amsden, and J. Cook. An arbitrary lagrangian-eulerian computing method for all flow speeds. *Journal of Computational Physics*, 14(3):227 – 253, 1974.
37. G. Hou, J. Wang, and A. Layton. Numerical methods for fluid-structure interaction - a review. *Communications in Computational Physics*, 12:337–377, 8 2012.
38. J. Hron and S. Turek. *A Monolithic FEM/Multigrid Solver for an ALE Formulation of Fluid-Structure Interaction with Applications in Biomechanics*, pages 146–170. Springer Berlin Heidelberg, Berlin, Heidelberg, 2006.
39. M.-C. Hsu, I. Akkerman, and Y. Bazilevs. Finite element simulation of wind turbine aerodynamics: validation study using nrel phase vi experiment. *Wind Energy*, 17(3):461–481, 2014.
40. B. Hübner, E. Walhorn, and D. Dinkler. A monolithic approach to fluid-structure interaction using space-time finite elements. *Computer Methods in Applied Mechanics and Engineering*, 193(23-26):2087 – 2104, 2004.
41. T. J. Hughes. *The finite element method: linear static and dynamic finite element analysis*. Courier Corporation, 2012.
42. B. M. Irons and R. C. Tuck. A version of the aitken accelerator for computer iteration. *International Journal for Numerical Methods in Engineering*, 1(3):275–277, 1969.
43. H. Jasak, H. Weller, and A. Gosman. High resolution nvd differencing scheme for arbitrarily unstructured meshes. *International Journal for Numerical Methods in Fluids*, 31(2):431–449, 1999.
44. J. Jimnez, A. A. Wray, P. G. Saffman, and R. S. Rogallo. The structure of intense vorticity in isotropic turbulence. *Journal of Fluid Mechanics*, 255:65–90, 10 1993.
45. G. John-Puthenveettil. *Computational modelling of complex flows using eddy-resolving models accounting for near-wall turbulence*. Shaker, 2012.
46. B. Kader. Temperature and concentration profiles in fully turbulent boundary layers. *International Journal of Heat and Mass Transfer*, 24(9):1541 – 1544, 1981.
47. A. Kalmbach and M. Breuer. Experimental PIV/V3V measurements of vortex-induced fluid-structure interaction in turbulent flow–a new benchmark FSI-PfS-2a. *Journal of Fluids and Structures*, 42:369 – 387, 2013.
48. C. Kassiotis, A. Ibrahimbegovic, R. Niekamp, and H. G. Matthies. Nonlinear fluid–structure interaction problem. part i: implicit partitioned algorithm, nonlinear stability proof and validation examples. *Computational Mechanics*, 47(3):305–323, 2011.
49. A. N. Kolmogorov. The local structure of turbulence in incompressible viscous fluid for very large reynolds numbers. In *Dokl. Akad. Nauk SSSR*, volume 30, pages 301–305. JSTOR, 1941.
50. A. N. Kolmogorov. On degeneration of isotropic turbulence in an incompressible viscous liquid. In *Dokl. Akad. Nauk SSSR*, volume 31, pages 538–540. JSTOR, 1941.

51. A. N. Kolmogorov. On degeneration of isotropic turbulence in an incompressible viscous liquid. In *Dokl. Akad. Nauk SSSR*, volume 32, pages 16–18. JSTOR, 1941.
52. U. Küttler and W. A. Wall. Fixed-point fluid–structure interaction solvers with dynamic relaxation. *Computational Mechanics*, 43(1):61–72, 2008.
53. B. Launder, G. J. Reece, and W. Rodi. Progress in the development of a reynolds-stress turbulence closure. *Journal of fluid mechanics*, 68(03):537–566, 1975.
54. B. Launder and B. Sharma. Application of the energy-dissipation model of turbulence to the calculation of flow near a spinning disc. *Letters in Heat and Mass Transfer*, 1(2):131 – 137, 1974.
55. B. Launder and D. Spalding. The numerical computation of turbulent flows. *Computer Methods in Applied Mechanics and Engineering*, 3(2):269 – 289, 1974.
56. T. Lehnhuser and M. Schfer. Improved linear interpolation practice for finite-volume schemes on complex grids. *International Journal for Numerical Methods in Fluids*, 38(7):625–645, 2002.
57. A. Leonard. Energy cascade in large-eddy simulations of turbulent fluid flows. In F. Frenkiel and R. Munn, editors, *Turbulent Diffusion in Environmental PollutionProceedings of a Symposium held at Charlottesville*, volume 18, Part A of *Advances in Geophysics*, pages 237 – 248. Elsevier, 1975.
58. M. Lesoinne and C. Farhat. Higher-order subiteration-free staggered algorithm for nonlinear transient aeroelastic problems. *AIAA journal*, 36(9):1754–1757, 1998.
59. Y. Li, K.-J. Paik, T. Xing, and P. M. Carrica. Dynamic overset CFD simulations of wind turbine aerodynamics. *Renewable Energy*, 37(1):285 – 298, 2012.
60. D. Lilly. A proposed modification of the germano subgrid-scale closure method. *Physics of Fluids A: Fluid Dynamics*, 4:633, 1992.
61. R. Löhner, C. Yang, J. Cebral, J. D. Baum, H. Luo, D. Pelessone, and C. Charman. Fluid-structure-thermal interaction using a loose coupling algorithm and adaptive unstructured grids. In *Proc., 29th AIAA Fluid Dynamics Conference*, 1998.
62. H. Lüdeke and J. B. Calvo. A fluid structure coupling of the ariane-5 nozzle section during start phase by detached eddy simulation. *CEAS Space Journal*, 1(1):33–44, 2011.
63. G. Martinat, M. Braza, Y. Hoarau, and G. Harran. Turbulence modelling of the flow past a pitching NACA0012 airfoil at and reynolds numbers. *Journal of Fluids and Structures*, 24(8):1294 – 1303, 2008. Unsteady Separated Flows and their Control.
64. H. G. Matthies and J. Steindorf. Partitioned strong coupling algorithms for fluid-structure interaction. *Computers & Structures*, 81(8-11):805 – 812, 2003. K.J Bathe 60th Anniversary Issue.
65. F. Menter and Y. Egorov. A scale-adaptive simulation model using two-equation models. *AIAA paper*, 1095:2005, 2005.
66. F. R. Menter. Two-equation eddy-viscosity turbulence models for engineering applications. *AIAA journal*, 32(8):1598–1605, 1994.
67. R. Mittal and G. Iaccarino. Immersed boundary methods. *Annual Review of Fluid Mechanics*, 37(1):239–261, 2005.
68. C. Mockett. *A Comprehensive Study of Detached Eddy Simulation*. Univerlagtuberlin, 2009.
69. R. D. Moser, J. Kim, and N. N. Mansour. Direct numerical simulation of turbulent channel flow up to $Re_\tau = 590$. *Physics of Fluids (1994-present)*, 11(4):943–945, 1999.
70. M. Münsch, A. Delgado, and M. Breuer. *Large-Eddy Simulation of a FSI-Induced Oscillation Test Case in Turbulent Flow*, pages 397–403. Springer International Publishing, Cham, 2015.

71. E. Naudascher and D. Rockwell. *Flow-induced vibrations: an engineering guide*. Courier Corporation, 2012.
72. G. D. Nayer and M. Breuer. Numerical investigation based on LES: Flow past a cylinder with a flexible splitter plate involving large deformations (-PfS-2a). *International Journal of Heat and Fluid Flow*, 50:300 – 315, 2014.
73. G. D. Nayer, A. Kalmbach, M. Breuer, S. Sicklinger, and R. Wüchner. Flow past a cylinder with a flexible splitter plate: A complementary experimental-numerical investigation and a new FSI test case (FSI-PfS-1a). *Computers & Fluids*, 99:18 – 43, 2014.
74. S. V. Patankar and D. B. Spalding. A calculation procedure for heat, mass and momentum transfer in three-dimensional parabolic flows. *International journal of heat and mass transfer*, 15(10):1787–1806, 1972.
75. F. S. Pereira, G. Vaz, and L. Eça. Flow past a circular cylinder: A comparison between rans and hybrid turbulence models for a low reynolds number. In *ASME 2015 34th International Conference on Ocean, Offshore and Arctic Engineering*, pages V002T08A006–V002T08A006. American Society of Mechanical Engineers, 2015.
76. C. S. Peskin. Flow patterns around heart valves: A numerical method. *Journal of Computational Physics*, 10(2):252 – 271, 1972.
77. U. Piomelli and J. R. Chasnov. Large-eddy simulations: theory and applications. In *Turbulence and transition modelling*, pages 269–336. Springer, 1996.
78. P. Pironkov. *Numerical Simulation of Thermal Fluid-Structure Interaction*. PhD thesis, Technische Universität, Darmstadt, January 2010.
79. S. Pope. A more general effective-viscosity hypothesis. *Journal of Fluid Mechanics*, 72(02):331–340, 1975.
80. S. B. Pope. *Turbulent Flows*. Cambridge University Press, 2000. Cambridge Books Online.
81. M. Popovac and K. Hanjalic. Compound wall treatment for RANS computation of complex turbulent flows and heat transfer. *Flow, Turbulence and Combustion*, 78(2):177–202, 2007.
82. J. Rakowski. The interpretation of the shear locking in beam elements. *Computers & Structures*, 37(5):769 – 776, 1990.
83. T. Reimann. *Numerische Simulation von Fluid-Struktur-Interaktion in turbulenten Strömungen*. Logos Verlag, 2013.
84. O. Reynolds. An experimental investigation of the circumstances which determine whether the motion of water shall be direct or sinuous, and of the law of resistance in parallel channels. *Philosophical Transactions of the Royal Society of London*, 174:935–982, 1883.
85. O. Reynolds. On the dynamical theory of incompressible viscous fluids and the determination of the criterion. *Philosophical Transactions of the Royal Society of London A: Mathematical, Physical and Engineering Sciences*, 186:123–164, 1895.
86. C. Rhie and W. Chow. Numerical study of the turbulent flow past an airfoil with trailing edge separation. *AIAA journal*, 21(11):1525–1532, 1983.
87. L. F. Richardson. *Weather prediction by numerical process*. Cambridge University Press, 1922.
88. S. Sachs, M. Streitenberger, D. Sternel, and M. Schäfer. Extrapolation methods for accelerating unsteady partitioned fluid-structure interaction simulations. *The International Journal of Multiphysics*, 5(4):287–298, 2011.
89. P. Sagaut. *Large eddy simulation for incompressible flows: an introduction*. Springer Science & Business Media, 2006.
90. M. Schäfer. *Computational Engineering - Introduction to Numerical Methods*, volume 0. Springer, Berlin, 2006. Numerische Berechnungsverfahren im Maschinenbau.

91. M. Schäfer, M. Heck, and S. Yigit. *An Implicit Partitioned Method for the Numerical Simulation of Fluid-Structure Interaction*, pages 171–194. Springer Berlin Heidelberg, Berlin, Heidelberg, 2006.
92. V. Shinde, T. Marcel, Y. Hoarau, T. Deloze, G. Harran, F. Baj, J. Cardolaccia, J. Magnaud, E. Longatte, and M. Braza. Numerical simulation of the fluid-structure interaction in a tube array under cross flow at moderate and high reynolds number. *Journal of Fluids and Structures*, 47:99 – 113, 2014. Special Issue on Unsteady Separation in Fluid-Structure Interaction-l.
93. J. Smagorinsky. General circulation experiments with the primitive equations. *Monthly Weather Review*, 91(3):99–164, 1963.
94. P. Spalart. Strategies for turbulence modelling and simulations. *International Journal of Heat and Fluid Flow*, 21(3):252 – 263, 2000.
95. P. Spalart, S. Deck, M. Shur, K. Squires, M. Strelets, and A. Travin. A new version of detached-eddy simulation, resistant to ambiguous grid densities. *Theoretical and Computational Fluid Dynamics*, 20(3):181–195, 2006.
96. P. Spalart, W. Jou, M. Strelets, and S. Allmaras. Comments of feasibility of les for wings, and on a hybrid RANS/LES approach. In *International Conference on DNS/LES, Aug. 4-8, 1997, Ruston, Louisiana.*, 1997.
97. P. R. Spalart and S. R. Allmaras. A one-equation turbulence model for aerodynamic flows. *AIAA-Paper 92-0439*, 94-439, 1992.
98. D. Spalding. Calculation of turbulent heat transfer in cluttered spaces. (unpublished work). In *10th International Heat Transfer Conference, Brighton, U.K.*, 1994.
99. S. P. Spekreijse. Elliptic grid generation based on laplace equations and algebraic transformations. *Journal of Computational Physics*, 118(1):38–61, 1995.
100. J. L. Steger and J. A. Benek. On the use of composite grid schemes in computational aerodynamics. *Computer Methods in Applied Mechanics and Engineering*, 64(1):301 – 320, 1987.
101. K. Stein, R. Benney, V. Kalro, T. E. Tezduyar, J. Leonard, and M. Accorsi. Parachute fluid-structure interactions: 3-d computation. *Computer Methods in Applied Mechanics and Engineering*, 190(3-4):373 – 386, 2000.
102. D. C. Sternel, M. Schäfer, M. Heck, and S. Yigit. Efficiency and accuracy of fluid-structure interaction simulations using an implicit partitioned approach. *Computational Mechanics*, 43(1):103–113, 2008.
103. H. L. Stone. Iterative solution of implicit approximations of multidimensional partial differential equations. *SIAM Journal on Numerical Analysis*, 5(3):530–558, 1968.
104. M. Strelets. Detached eddy simulation of massively separated flows. In *AIAA, Aerospace Sciences Meeting and Exhibit, 39 th, Reno, NV*, 2001.
105. B. M. Sumer and J. Fredsøe. *Hydrodynamics around cylindrical structures*, volume 12. World Scientific, 1997.
106. K. Takizawa, C. Moorman, S. Wright, T. Spielman, and T. E. Tezduyar. Fluid-structure interaction modeling and performance analysis of the orion spacecraft parachutes. *International Journal for Numerical Methods in Fluids*, 65(1-3):271–285, 2011.
107. K. Takizawa, T. Spielman, and T. E. Tezduyar. Space–time FSI modeling and dynamical analysis of spacecraft parachutes and parachute clusters. *Computational Mechanics*, 48(3):345–364, 2011.
108. R. Taylor. Feap - A Finite Element Analysis Program, Version 7.5 User Manual. *University of California at Berkeley, Berkeley, CA*, 2005.
109. L. Temmerman, M. A. Leschziner, C. P. Mellen, and J. Fröhlich. Investigation of wall-function approximations and subgrid-scale models in large eddy simulation of separated flow in a channel with streamwise periodic constrictions. *International Journal of Heat and Fluid Flow*, 24(2):157 – 180, 2003.

110. P. D. Thomas and C. K. Lombard. Geometric conservation law and its application to flow computations on moving grids. *AIAA J.*, 17:1030–1037, 1979.
111. W. Tollmien, H. Schlichting, H. Görtler, and F. W. Riegels. *Ludwig Prandtl Gesammelte Abhandlungen: zur angewandten Mechanik, Hydro- und Aerodynamik*, chapter On the Rôle of Turbulence in Technical Hydrodynamics, pages 798–811. Springer Berlin Heidelberg, Berlin, Heidelberg, 1961.
112. A. Travin, M. Shur, M. Strelets, and P. R. Spalart. *Physical and Numerical Upgrades in the Detached-Eddy Simulation of Complex Turbulent Flows*, pages 239–254. Springer Netherlands, Dordrecht, 2002.
113. A. K. Travin, M. L. Shur, P. R. Spalart, and M. K. Strelets. Improvement of delayed detached-eddy simulation for les with wall modelling. In *ECCOMAS CFD 2006: Proceedings of the European Conference on Computational Fluid Dynamics, Egmond aan Zee, The Netherlands, September 5-8, 2006*. Delft University of Technology; European Community on Computational Methods in Applied Sciences (ECCOMAS), 2006.
114. P. Tucker. Differential equation-based wall distance computation for DES and RANS. *Journal of Computational Physics*, 190(1):229 – 248, 2003.
115. S. Türk. *Investigation of hybrid turbulence modeling techniques in the context of fluid-structure interaction.* PhD thesis, TU Darmstadt, München, 2015. Zugl.: Technische Universität Darmstadt, Diss., 2014.
116. S. Türk, T. Reimann, D. Sternel, and M. Schäfer. On the performance of detached-eddy simulation in fluid-structure interaction problems. In *5th Conf. on Computational Methods for Coupled Problems in Science and Engineering (Coupled 2013), Ibiza, Spain*, 2013.
117. E. R. Van Driest. On turbulent flow near a wall. *J. Aerospace Sci.*, 23:1007–1011, 1956.
118. J. Vierendeels. *Implicit Coupling of Partitioned Fluid-Structure Interaction Solvers using Reduced-Order Models*, pages 1–18. Springer Berlin Heidelberg, Berlin, Heidelberg, 2006.
119. E. Walhorn, A. Kölke, B. Hübner, and D. Dinkler. Fluid-structure coupling within a monolithic model involving free surface flows. *Computers & Structures*, 83(25-26):2100 – 2111, 2005.
120. W. A. Wall, A. Gerstenberger, P. Gamnitzer, C. Förster, and E. Ramm. *Large Deformation Fluid-Structure Interaction – Advances in ALE Methods and New Fixed Grid Approaches*, pages 195–232. Springer Berlin Heidelberg, Berlin, Heidelberg, 2006.
121. S. Wallin and A. V. Johansson. An explicit algebraic reynolds stress model for incompressible and compressible turbulent flows. *Journal of Fluid Mechanics*, 403:89–132, 2000.
122. D. Wilcox. Reassessment of the scale-determining equation for advanced turbulence models. *AIAA JOURNAL*, 26(11):1299–1310, NOV 1988.
123. J. N. Wood and M. Breuer. Complementary experimental–numerical investigation of the flow past a rigid and a flexible hemisphere in turbulent flow: Part i: Experimental measurements. In *Fachtagung Experimentelle Strömungsmechanik*, 2016.
124. A. Wray. A selection of test cases for the validation of large-eddy simulations of turbulent flows. *AGARD Advisory Report*, 345, 1998.
125. M. Young and A. Ooi. Comparative assessment of les and urans for flow over a cylinder at a reynolds number of 3900. In *16th Australasian Fluid Mechanics Conference (AFMC)*, pages 1063–1070. School of Engineering, The University of Queensland, 2007.
126. Z. Yu. A dlm/fd method for fluid/flexible-body interactions. *Journal of Computational Physics*, 207(1):1 – 27, 2005.
127. O. C. Zienkiewicz, R. L. Taylor, O. C. Zienkiewicz, and R. L. Taylor. *The finite element method*, volume 1,2,3. McGraw-hill London, 1977.

Ich erkläre hiermit, dass ich die Dissertation selbstständig und nur unter Zuhilfenahme der angegebenen Hilfsmittel und Quellen angefertigt habe.

Darmstadt, 9. Februar 2017

Awais Ali